TRIBHUVAN UNIVERSITY

INSTITUTE OF ENGINEERING

PULCHOWK CAMPUS

B-06-BME-2018/2023

ASSESSING THE IMPACT OF CAVITATION MODELS ON THE PERFORMANCE OF MOTORBOAT PROPELLERS: A NUMERICAL ANALYSIS

BY

ADARSHA PAUDEL (075BME006)

AMIT HITANG (075BME008)

SAMEER ADHIKARI (075BME038)

A PROJECT REPORT

SUBMITTED TO THE DEPARTMENT OF MECHANICAL AND AEROSPACE ENGINEERING IN PARTIAL FULFILLMENT OF THE REQUIREMENTS FOR THE DEGREE OF BACHELOR IN MECHANICAL ENGINEERING

DEPARTMENT OF MECHANICAL AND AEROSPACE ENGINEERING

LALITPUR, NEPAL

MARCH, 2023

COPYRIGHT

TRIBHUWAN UNIVERSITY

INSTITUTE OF ENGINEERING

PULCHOWK CAMPUS

DEPARTMENT OF MECHANICAL AND AEROSPACE ENGINEERING

The undersigned certify that they have read, and recommended to the Institute of Engineering for acceptance, a project report entitled " ASSESSING THE IMPACT OF CAVITATION MODELS ON THE PERFORMANCE OF MOTORBOAT PROPELLERS: A NUMERICAL ANALYSIS " submitted by Adarsha Paudel, Amit Hitang and Sameer Adhikari in partial fulfillment of the requirements for the degree of Bachelor of Mechanical Engineering.

Supervisor, Mr. Neeraj Adhikari
Assistant Professor
Department of Mechanical and Aerospace Engineering

Supervisor, Mr. Laxman Motra
Assistant Professor and Deputy Head of Department
Department of Mechanical and Aerospace Engineering

External Examiner, Er. Smarika Tamrakar
Senior Mechanical Engineer
NEA Engineering Company

Committee Chairperson, Dr. Surya Prasad. Adhikari
Head, Department of Mechanical and Aerospace Engineering
Pulchowk Campus

13-03-2023

Date

II

ABSTRACT

This paper presents simulation of cavitating flows on a motorboat propeller and the performance changes brought by two cavitation models. K-ω SST was used as the turbulence model and effect of cavitation was introduced via cavitation models. The cavitation models are based on multiphase mixture model. Singhal cavitation model and Schnerr-Sauer cavitation models are some of the widely used cavitation models in literature. Both cavitation models were compared based on vapor fraction and performance parameters. The major difference in the two models is the inclusion of effects of non-condensable gases on Singhal cavitation model. The difficulty in setup and convergence of Singhal cavitation model has put forward other cavitation models as its alternatives. According to the results of this paper, both cavitation models show similar nature of cavitation in the propeller, with slight variation in performance parameters. If model parameters can accurately set according to properties of water, accuracy of these models can be further improved. Unless the effects of non-condensable gases are significant, the Schnerr-Sauer cavitation model is a good alternative to Singhal cavitation model to save computational costs.

ACKNOWLEDGEMENTS

TABLE OF CONTENTS

LIST OF FIGURES

VIII

LIST OF TABLES

LIST OF ABBREVIATIONS

CFD   Computational Fluid Dynamics

EFD   Experimental Fluid Dynamics

EWT   Enhanced Wall Treatment

LES   Large Eddy Simulation

PISO   Pressure Implicit with Splitting of Operators

QUICK   Quadratic Upwind Interpolation For Convective Kinematics

RANS   Reynolds-Averaged Navier-Stokes

RPS   Revolutions Per Second

SST   Shear-Stress Transport

LIST OF SYMBOLS

ρ Density of two-phase mixed flow

v Quality-averaged velocity vector of two-phase mixed flow

P   Pressure

μ Molecule viscosity

μ_t Turbulence viscosity

f Mass ratio of cavity phase

R_e Formation rate of steam

R_c Condensation rate of steam.

g Acceleration due to gravity

τ Time

t Turbulence

D   Diameter (m)

N   Rotational speed (rps)

V_A Advance velocity (m/s)

γ Volume fraction of water

p_v Vapor pressure (Pa)

p_∞ Free stream pressure (Pa)

c_p Pressure coefficient

J   Advance ratio

KQ   Torque coefficient

KT   Thrust Coefficient

η Efficiency

ST   Surface tension coefficient

Z   Number of blades

σ Cavitation number

Y+   Wall function

CHAPTER ONE: INTRODUCTION

1.1. Background

The conventional internal combustion outboard engine, as shown in the figure, remains the dominant modern form of marine propulsion, with a wide range of output capacities from 2 to 557 horsepower (hp) and weight varying from a few kilograms to half a metric ton. There are different types of outboard engines, each with varying designs, sizes, outputs, and weights. Outboard engines are highly preferred due to their excellent performance, affordable cost, ease of installation, lower fire risk, lightweight, high speed, better maneuverability, ability to navigate shallow waters with less draft, and easy launching and beaching. These features make them a popular power source for boats and ships. (H. S. Rainbow, 1963).

Figure 1.1 Outboard Motorboat Engine

Propellers are utilized to create the necessary thrust to move a ship through water. These fan-like structures are powered by the ship's engine and work by imparting momentum to the water, which generates a force that propels the vessel forward. The propulsion of a ship by a propeller is governed by Bernoulli's principle and Newton's third law of motion. As the propeller rotates, it creates a pressure difference between the forward and aft sides of the blade, causing water to accelerate behind it. This acceleration of

water generates a force that drives the ship forward. Different types of propellers are available, and their design can significantly impact a ship's performance.

i. Based on the type of pitch:
   a. Fixed pitch propeller
   b. Controllable pitch propeller
ii. Based on number of blades
   a. Three blade propeller
   b. Four blade propeller
   c. Five blade propeller

A propeller is a crucial component of a ship's propulsion system, and its efficient operation is essential for safe and smooth navigation through water.

The occurrence of cavitation in a ship's propeller can have a detrimental impact on the vessel's propulsive performance and can also cause rapid wear and tear of the propeller. Cavitation typically initiates at the tips of the blades and gradually spreads across them as the propeller loading increases. Once the cavitation has extended to about 0.75 of the radius, there is a notable decrease in thrust, followed by a decline in torque. This decrease in torque implies that there will be a significant increase in revolutions required for a given power. Vibration is produced due to the unstable nature of cavitation and is characterized by the periodic bending or twisting of the structure in vertical, horizontal, or torsional directions. The implosion of the cavities creates noise effects that, when combined with high-frequency vibrations, can be highly unpleasant for passengers and crew situated in the aft end of the ship's accommodation.

1.2. Problem Statement

Cavitation is a major concern for any rotating mechanism in a fluid as it is inevitable. It is important to determine the cavitation prone areas extent of cavitation to minimize its effects in the propeller. Experimentally testing cavitation is very expensive and not very versatile. Because of the cavitation caused on the propeller blades, using an outboard motor as a substitute for a high-speed boat still presents a hurdle. Study of various factors affecting the cavitation is necessary to design a high performance propeller.

1.3. Objective

1.3.1. Main Objective

The main objective of this project is to study propeller cavitation on available propeller blade of the ship with the help of Computational Fluid Dynamics (CFD)

1.3.2. Specific Objectives

- To perform numerical simulation using CFD to study cavitation on the selected blade.
- Comparison of two mixture cavitation models: Schnerr-Sauer cavitation model and Singhal cavitation model.
- To analyze the effect of cavitation on the performance of propeller

1.3.3. Rationale of the Project

Conducting experiments to study cavitation phenomenon is very expensive and time consuming as it involves large experimental facility including infrastructure, large machinery and sophisticated devices. The rationale of this project is to use CFD methodology and some validated numerical models to study the cavitation phenomena and its impact on performance of propeller.

CFD methodology needs to be compared against experimental results for validation. In the absence of such experimental facility, validated cavitation model such as Singhal cavitation model can be used as a substitute to simulate the cavitation in a propeller. Even though Singhal cavitation model has good agreement to the experimental results as found in literature, convergence is still a difficult task in this model. Hence Schnerr-Sauer cavitation model is compared against Singhal cavitation model in an attempt to lower the computational cost and easier convergence.

1.3.4. Assumptions and Limitations

In this project CFD simulation was performed on the motorboat propeller.

- Effect of sediments is neglected.
- Scaled down prototype doesn't show the same cavitation characteristics of the model.
- The CAD model used in this project is not available in literature to validate the computational results.
- Experimental setup involves large infrastructures and expensive devices.

CHAPTER TWO: LITERATURE REVIEW

2.1. Outboard Propulsion System

The propulsion system of a boat comprises several components that generate rotary motion to move the vessel. In the case of an outboard propulsion system, the engine is an independent power unit mounted externally on the hull of the boat.
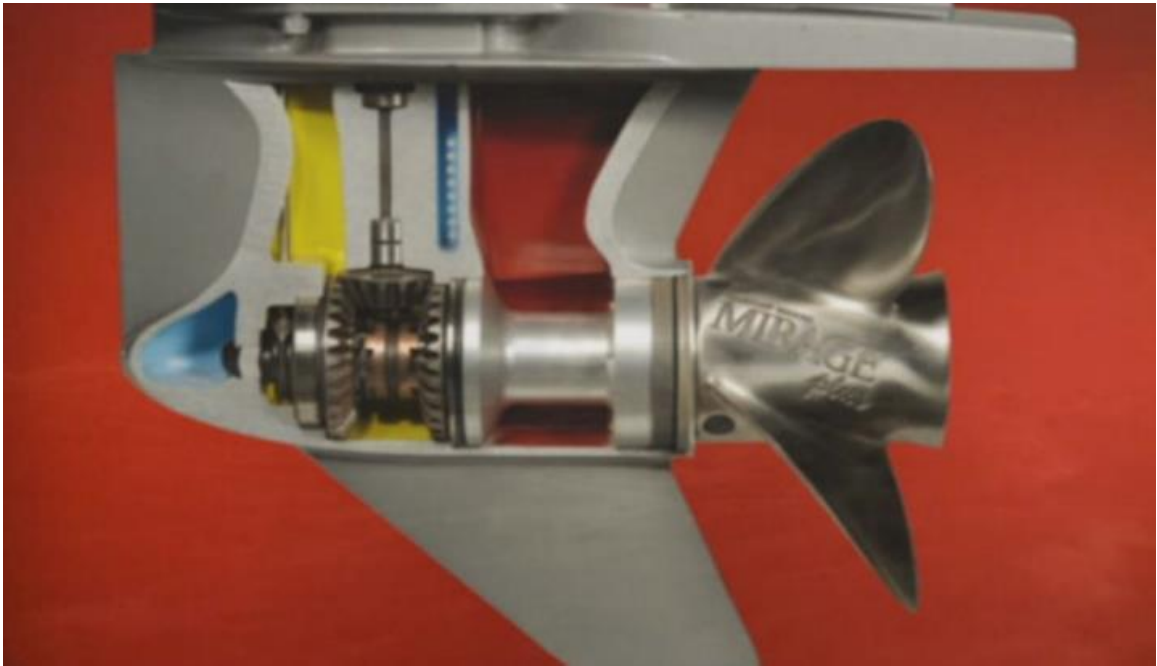
Figure 2.1 Propulsion System of an Outboard Engine (Gatete et al., 2018)

Propellers play a vital role in boat propulsion by creating the necessary force to move through water. Its design incorporates a mechanism to push water, and the resulting reaction propels the boat forward. The propeller design can greatly impact fuel efficiency, thrust, torque, and overall efficiency, making it an essential component. It is crucial to anticipate the performance of the propeller under consideration due to its significant influence on the boat's performance.

Based on their functions, the outboard engine can be categorized into six subsystems, which are the mechanical drive system, swivel bracket system, water intakes, propulsion system, and exteriors. The engine and transmission shafts generate kinetic energy, and this is the primary function of the mechanical drive system. The swivel bracket system supports the engine and allows for turning, while also distributing the propeller's thrust through its clamp located at the stern of the boat. Seawater enters through the water intakes to cool the engine. The gear box and propeller are the primary

components of the propulsion system. The covers, connections, and decorative pieces make up the exteriors.
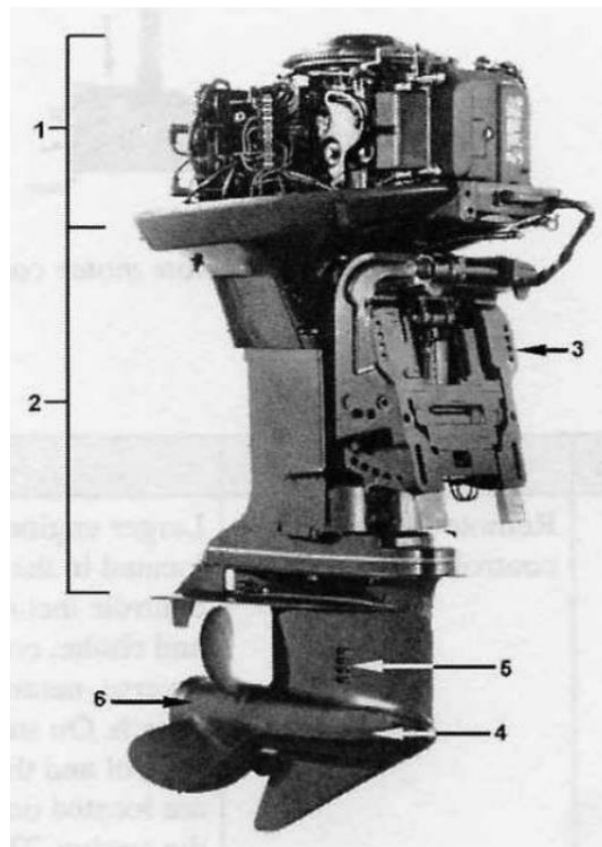
Figure 2.2 Parts of an Outboard Engine

(Gatete et al., 2018)

Where in Figure 2-2

1 and 2: Mechanical drive system,

3: Swivel bracket system,

4: Gearbox,

5: Water intakes,

6: Propeller.

2.2. Outboard Propeller

A propeller is a device utilized for propulsion in motorboats that creates movement by propelling the surrounding fluid in an axial backward direction. It comprises a motorboat propeller consisting of a pair of identical twisted blades positioned equally around a hub.

2.2.1. Basic Nomenclature

Hub: The propeller's hub is a solid disk positioned at the center of the propeller that is connected to the propeller shaft and to which the blades are attached. To achieve maximum thrust, the ideal diameter of the hub should be as small as possible. However, there is a compromise between hub size and strength. If the hub's diameter is too small, it may not be robust enough to withstand the forces acting on it.

Blades: The propeller blades are angled fins or wings that extend outwards from the hub of the propeller. The torque capacity of a propeller is determined by the blade's shape and the speed at which they rotate.

Blade Root and Blade Tip: The base where the propeller blade attaches to the hub is known as the root, while the farthest end of the blade away from the propeller shaft is referred to as the tip.

Blade Face and Back: The pressure face, which is the high-pressure side of a blade, is the surface that is facing backward and pushing the water when the ship moves forward. On the other hand, the suction face or the low-pressure side is the back of the blade that is facing the front or upstream direction.

Leading and Trailing Edges: The forward edge of a propeller blade, which slices through the fluid, is known as the leading edge. The downstream edge is referred to as the trailing edge.

Right-Handed vs. Left-Handed: The shape of a propeller is affected by its "handedness". In forward motion, a right-handed propeller turns in a clockwise direction when viewed from the stern of the vessel. When in forward motion, a left-handed propeller rotates counterclockwise when viewed from the stern. A propeller's handedness is unchangeable, meaning that a right-handed propeller cannot be substituted with a left-handed one and vice versa.

Diameter: The size of a propeller, specifically its diameter or radius, is a significant factor in determining its ability to absorb and deliver power, which in turn affects the amount of thrust available for propulsion. Increasing the diameter of a propeller even slightly can lead to a significant increase in both thrust and torque load on the engine shaft. However, larger diameters also result in slower propeller revolutions due to structural limitations and engine capacity.
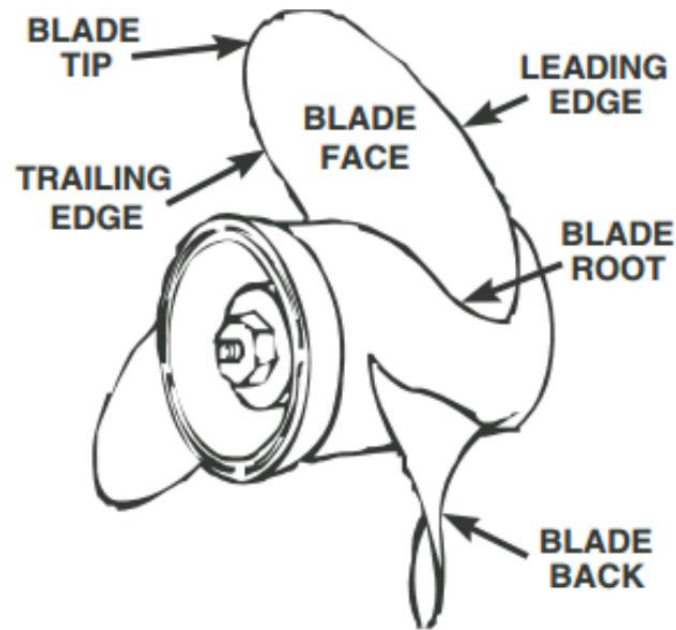
Figure 2.3 Parts of an Outboard Propeller (Gatete et al., 2018)

Pitch: The pitch of a propeller describes the distance it moves forward with each full rotation. For example, a propeller with a pitch of 10 inches moves 10 inches forward during one full rotation. However, due to the propeller being attached to a shaft, it drives the vessel forward instead of moving forward itself. The distance that the ship travels during one rotation of the propeller is actually less than the pitch. The difference between the nominal pitch and the actual distance traveled is called slip. Blade twisting is often employed to maintain constant pitch from the root to the tip. A pitch ratio, expressed as the pitch-to-diameter ratio, is typically given and ranges from 0.5 to 2.5. The ideal value for most vessels is usually closer to 0.8 to 1.8. Pitch plays a significant role in transferring propeller shaft torque to thrust by redirecting or accelerating water astern, which is an application of Newton's Second Law.

Meanline: The meanline of a propeller refers to the theoretical line running along the blade's centerline from its leading edge to its trailing edge.

Nose-Tail line: The straight line that goes from the front edge (nose) to the back edge (tail) of a propeller blade is called the nose-tail line.

Chord length: Chord length refers to the length of the nose-tail line.

Camber height: Camber height refers to the distance between the meanline and the highest point of the blade's camber curve at a particular point along the blade span.

Max. Camber: Maximum camber height along the section

Thickness: Section thickness of the propeller along a line normal to the meanline.

Max. Thickness: Maximum section thickness

Rake: The angle between the propeller blade and the hub or the angle between the blade's tip and a plane that is perpendicular to the propeller shaft is known as "rake" in propeller design. If the blade's tip is angled aft (toward the rear) relative to the perpendicular plane, it is considered to have a positive rake. Conversely, if the tip is angled forward, it has a negative rake.
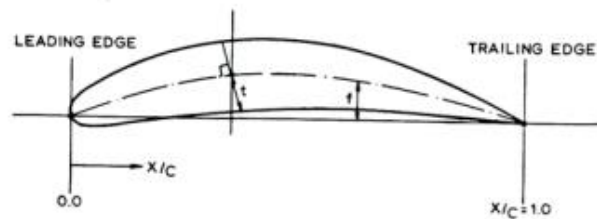
Figure 2.4 Cross Section of a Hydrfoil
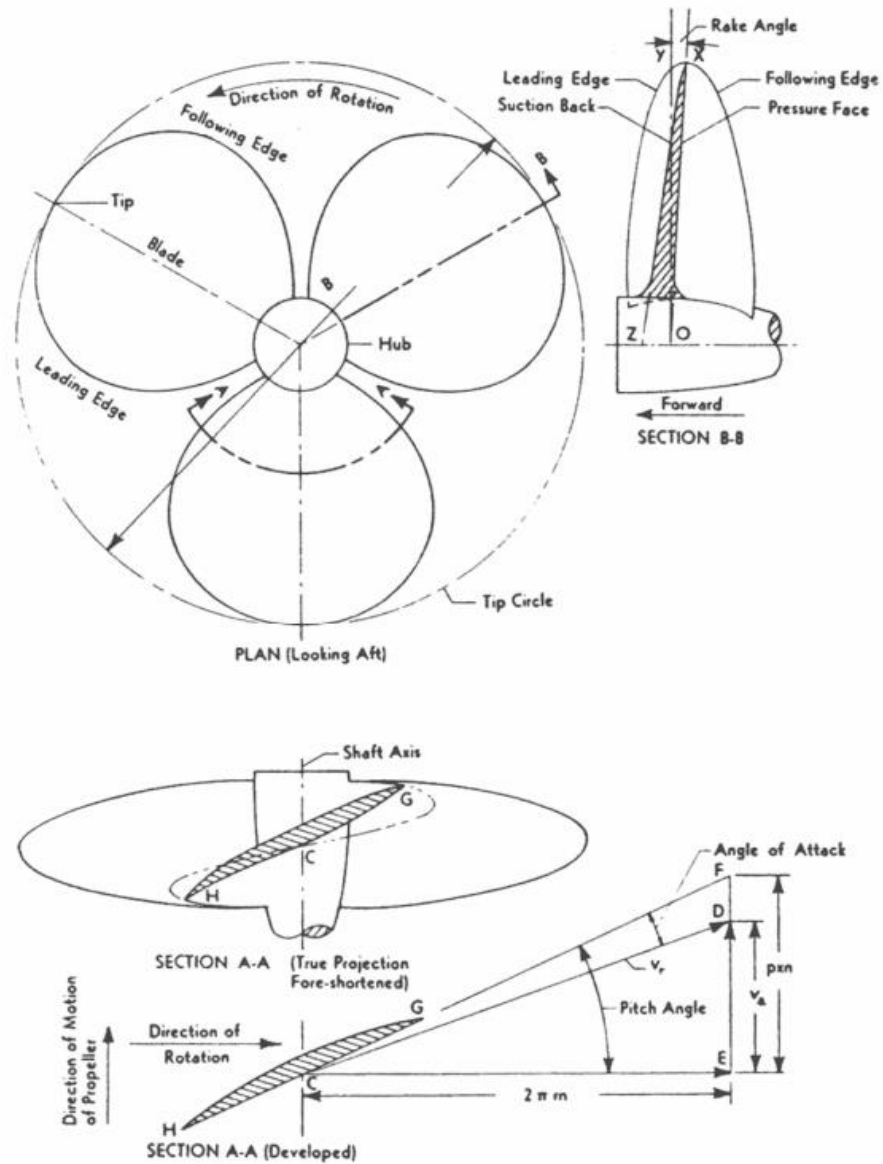
Figure 2.5: Propeller Design Parameters (Techet A., 2005)

2.2.2. Material and Construction of Propellers

Ship propellers are susceptible to corrosion due to their direct contact with water, which accelerates the process. As a result, they are made from materials that are resistant to corrosion. The most commonly used materials for marine propellers are a combination of aluminum and stainless steel. Since propellers undergo cyclic loading during operation, they are susceptible to fatigue, and materials such as alloys of nickel,

aluminum, and bronze are used because they are lighter and have greater strength and fatigue resistance, making them a popular choice for propeller construction. Propellers are typically constructed by welding or forging several blades to the hub, but forged blades are considered more reliable and have better resistance to fatigue and erosion, although they are more expensive than welded ones.

Although the design and shape of propellers have evolved with advancements in boat designs, the construction process remains the same as it was in the 1950s. The propeller is made using the sand-casting process, which involves four primary steps: creating the pattern, creating the mold cavity, pouring the metal, and finishing.

2.2.3. Performance Characteristics

Typically, an outboard engine's lower unit has a propeller that operates in water that has been disturbed by the boat's forward movement. Consequently, the propeller's performance is affected by the boat to which it is attached. Therefore, it is essential to test the propeller's performance in open water conditions, independent of the boat to evaluate its performance characteristics. (Rawson K. J.et al.2010)

Open Water Characteristics

The propeller's forces and moments can be described using non-dimensional properties, which are created through dimensional analysis. These properties provide a way to express the propeller's performance characteristics in a general way. Depending on the physical quantities being measured, there are various functions like density of water (ρ), diameter of propeller (D), acceleration due to gravity (g), rotational speed (N), pressure (P), viscosity (μ) etc. SW that can be used to represent the propeller's thrust (T) and torque (Q);

$$T = f_1(\rho, D, v, g, N, P, \mu)$$

Equation 2.1

And,

$$Q = f_2(\rho, D, v, g, N, P, \mu)$$

Equation 2.2

The propeller's performance is a critical factor in creating an efficient propulsion system, which depends on the thrust force, torque, and efficiency. To evaluate these performance characteristics, non-dimensional values such as the thrust coefficient (K_T),

torque coefficient (K_Q), coefficient of cavitation, and open propeller efficiency (η_o) are calculated with respect to the advance coefficient using propeller performance (J). Techet et al. provide equations for calculating K_T, K_Q, η_0, and J.

$$K_T = \frac{T}{\rho N^2 D^4}$$

Equation 2.3

$$K_Q = \frac{Q}{\rho N^2 D^5}$$

Equation 2.4

$$\eta_0 = \frac{TVa}{2\pi NQ}$$

$$\eta_0 = \frac{K_T \, \rho N^2 \, D^4 \, V_a}{2\pi N K_Q \rho N^2 \, D^5} = \frac{K_T}{K_Q} \cdot \frac{V_a}{2\pi ND} = \frac{K_T}{K_Q} \cdot \frac{J}{2\pi}$$

Equation 2.5

Advanced ratio

The advanced ratio of a marine propeller is a performance indicator that quantifies the relationship between a ship's forward speed and its propeller's rotating speed. It can be calculated as the ratio between the propeller's rotational speed n and the product of the propeller's diameter D.

Mathematically, the advanced ratio (J) is given by:

$$J = \frac{V_a}{ND}$$

Equation 2.6

The advanced ratio is significant because it serves as a quantitative tool in choosing the best propeller design and configuration for a particular ship. The advanced ratio has an impact on the propeller's effectiveness, power, and thrust. The advanced ratio is a measure of how efficiently the propeller is able to convert its rotational energy into forward motion for the boat.

11

In general, lower advanced ratio values (J<0.4) indicate greater efficiency, while higher values (J>0.4) indicate greater thrust and propulsive force. Consequently, lower advanced ratios are favored for ships that prioritize fuel efficiency, whereas higher advanced ratios may be more appropriate for ships that prioritize speed and maneuverability.

A propeller's cavitation performance can also be predicted using the advanced ratio. Cavitation, which can result in damage and lower propeller performance, is the creation and bursting of bubbles surrounding the propeller blades. In order to prevent cavitation issues, it's crucial to build propellers that are suited for a specific advanced ratio range. Greater advanced ratios can make cavitation more likely.

In order to compare various propeller properties, including diameter, pitch, and blade area, among others, advanced ratios can be utilized as a non-dimensional measure. This is due to the fact that the advanced ratio is a comparison of speeds or velocities, which are by nature non-dimensional quantities.

One can know more about the relative efficiencies, propulsive powers, and cavitation susceptibilities of various propellers by comparing their advanced ratios. When choosing and developing propellers for various uses, such as marine or boat propulsion, and when maximizing propeller performance under particular operating conditions, this knowledge might be helpful.

2.2.4. Parameters Affecting Performance

The performance and efficiency of a propeller are heavily influenced by three key variables: diameter, rotational speed, and pitch. Pitch refers to the forward motion generated by a single rotation of the propeller. However, when selecting the appropriate propeller, other factors also need to be considered, including the pitch to diameter ratio, rotation speed, blade number to area ratio, skew angle, blade shape, and blade thickness.

Propeller Diameter

The diameter of a propeller is an important factor in determining the amount of power it can absorb and output, and this, in turn, affects the amount of thrust available for propulsion. Generally, propeller efficiency and diameter have an inverse relationship, except in high-speed vehicles (over 35 knots) where a larger diameter corresponds to higher efficiency. However, in fast-moving vessels, a bigger diameter can result in more

drag. A wider diameter propeller turns more slowly, up to the limits of structural loads and engine rating, because even a small increase in diameter increases the thrust and torque load on the engine shaft significantly. To determine the propeller diameter for maximum efficiency, a sophisticated process involving several empirical calculations is used. In high-speed vessels, a larger propeller diameter can slow down the rotational speed while still achieving the necessary forward motion. This can reduce inflow forces, resulting in a decrease in pressure imbalance on the blades and a corresponding reduction in cavitation. Therefore, a large diameter propeller can allow for slower rotation and less cavitation at a given engine output or intended forward speed. (Johnson et al. 2011)

Rotational Speed

For vessels moving at speeds below 35 knots, a larger diameter and lower speed result in higher torque. The RPM for high-speed boats can range from 2000 to 6000, and by using these values, the inflow velocity for a particular advance coefficient can be calculated.

Pitch to Diameter Ratio

The measurement of how far a propeller can travel with each full rotation is determined by its pitch. However, it is important to note that the propeller itself does not move forward due to its connection to a shaft, but rather it propels the ship ahead. Interestingly, the forward motion of the boat with each spin of the propeller is actually less than the pitch distance. Typically, for high-speed watercraft, the pitch can range between 9 to 24 inches. To ensure uniform pitch from the root to the tip of the blades, they are twisted.

In an effort to create an efficient maritime propeller that has the lowest torque and minimal cavitation, Mojtaba et al.(2014) used Blade Element Theory (BET), a numerical method to evaluate thrust and how it varies based on the propeller's geometry. Pitch ratio, blade area ratio, and skew angle were the input variables used to design the optimal propeller that would deliver the highest possible performance. By experimenting with several pitch ratios such as 0.4, 0.6, 0.8, 1.0, 1.2, and 1.4, the researchers were able to identify those that met the propeller's performance

requirements. The study also revealed that the skew angle effect can determine propeller efficiency within the limitations of the cavitation issue. It is noteworthy that this study did not consider optimization factors such as blade count, material selection, and diameter.

In another study, Kiam et al. (2014) predicted the performance characteristics of a three-bladed marine propeller through an investigation that aimed to characterize marine propeller performance using Computational Fluid Dynamics (CFD). The study used the RANS solver for computational flow analysis and evaluated the propeller's performance characteristics with respect to the advance coefficient. The researchers used five propellers with varying pitch-to-diameter ratio values of 0.6, 0.8, 1.0, 1.2, and 1.4. The study revealed that as the pitch diameter ratio increased, efficiency, torque, and thrust also increased.

Number of Blades

When discussing marine propellers, the blades are the twisted fins or foils extending from the hub that play a crucial role in determining the torque produced and speed achieved. The shape of the blades and the speed at which they are propelled can impact the torque of a particular propeller. However, when selecting the number of blades, it is important to avoid resonance as it can affect both the frequency and intensity of vibrations during operation. The diameter, area, and number of blades are strongly correlated, with larger diameters requiring fewer blades and larger areas requiring more blades. To minimize suction side sheet cavitation, it is recommended to increase the number of propeller blades as this will decrease the strain on each blade, while root cavitation can be increased due to decreased clearance between each blade.

It is recommended that the number of blades for a marine propeller should fall within the range of 2 to 6, with each blade having an area ratio of 16-18%. For each additional blade, it is suggested to reduce the diameter by 4%. This recommendation is based on considerations of performance and cavitation efficiency, as proposed by Johnson E. in 1998.

Additionally, Kiam et al.(2014) examined the impact of the number of blades on the efficiency of marine propellers. Using a computational flow analysis, the study

analyzed five propellers with varying blade counts, ranging from 2 to 5. The results showed that increasing the number of blades led to an increase in torque and thrust, but a decrease in efficiency. Although additional blades may lower efficiency and increase fuel consumption, they can improve velocity.

Boucetta et al.(2016) also explored the effect of skew magnitude, thickness, and blade count on the hydrodynamic performance of marine propellers. The study employed a numerical simulation of the flow around a marine propeller using the RANS method of the commercial CFD code fluent. Varying the blade count from three to four and five, the researchers found that increasing blade thickness improved propeller efficiency, while adopting a skew angle on the blade enhanced the hydrodynamic performance of marine propellers. The four-bladed propeller was found to have the best efficiency. However, the effect of blade materials, pitch diameter ratio, and rotational speed on propeller performance was not taken into account in this study.

2.3. Cavitation

The development of vapor bubbles in a liquid at low pressure levels is known as cavitation. Cavitation can occur in moving fluid, which is the subject of this work, or it can be produced by an ultrasonic acoustic field. The process of cavities (bubbles) forming, expanding, and then collapsing in a flowing liquid is known as hydrodynamic cavitation. When the flow rate increases and the system pressure approaches the saturation vapor pressure at a specific liquid temperature, the process of bubble formation takes place. Surfaces that come into contact with cavitation, noise, and vibration are eroded as a result of the local microjets and shock waves that form when these vapor bubbles collapse.

Multi-phase flow zones are, by definition, cavitating flows. Water and its own vapor are the two phases that are most crucial, but in virtually all instances, there is also an amount of gas, such as air, which has considerable impacts on both bubble collapse and inception, typically having the most impact on the inception process. Cavitation is therefore typically seen as a two-phase, three-component flow regime (Water, its own vapor, and gas such as air).

Cavitation can arise in a variety of situations, ranging from marine propellers to medical equipment utilizing ultrasound technology. Below are few different types of cavitation:

Surface cavitation: When the surface pressure of an object drops below the liquid's vapor pressure, small bubbles can form on the surface, such as on marine propellers.

Cloud cavitation: Large quantities of bubbles can form due to a decrease in liquid pressure, causing them to coalesce into a "cloud" that can inflict damage on machinery.

Gas cavitation: The injection of a gas into a liquid can lead to the formation of bubbles when pressure drops, a technique used in industrial processes to mix gases and liquids.

Acoustic cavitation: High-frequency sound waves can be utilized to create bubbles in a liquid, as in the case of medical ultrasound machines.

Bubble collapse cavitation: The collapse of bubbles within a liquid can generate shock waves that cause harm to nearby objects. This can occur in marine propellers, for instance.

Vortex cavitation: Bubbles can develop in a liquid when a vortex forms, leading to a drop in pressure. This can happen in fluid mixers, for example.

Transient cavitation: The sudden decrease in pressure can cause bubbles to arise. This can happen when high-pressure liquid is suddenly released into a low-pressure environment.

Cavitation erosion: Repeated formation and collapse of bubbles can inflict damage on nearby surfaces, such as the blades of marine propellers.

Fixed and traveling bubble cavitation are the two categories into which propeller cavitation can be subdivided. Sheet cavitation is a thin, glassy sheet of gas and vapor that extends from the leading edge to a specific chordwise point and is essentially immobile with regard to the propeller blade. Cavitation of this kind frequently occurs on lifting surfaces and hydrofoils. The instance of a hydrofoil illustrates the mechanics of sheet cavitation commencement.
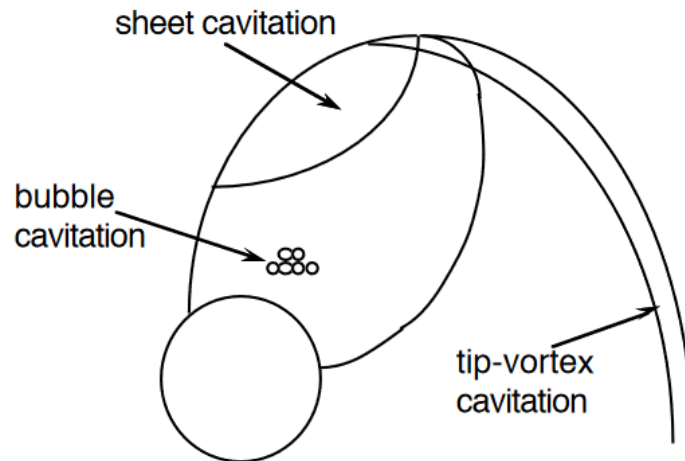
Figure 2.6 Types of Cavitation (Matusiak J., 1992)

Low pressure forms on the top (suction) side of a hydrofoil in a flow with a velocity of U and an ambient pressure of P_0 at an angle of attack, which is a fairly typical cavitation type. Cavitation happens if this pressure falls below the vapor pressure value, or P_v.

Cavitation Number

The cavitation behavior of maritime propellers is described by cavitation numbers, a performance metric. Cavitation is a phenomenon that happens when the pressure around a propeller blade falls below the vapor pressure of the fluid in the vicinity, resulting in the formation of bubbles and their subsequent collapse as the pressure rises. It's crucial to design propellers that function within acceptable cavitation limits since cavitation can harm propellers and decrease their effectiveness. The cavitation number (σ) is a non-dimensional parameter that compares the local pressure around a propeller blade to the vapor pressure of the fluid. It is defined as:

$$\sigma = \frac{P_0 - P_v}{0.5\rho V^2}$$

Where, P_0 is the local pressure, P_v is the vapor pressure of the fluid, ρ is the fluid density, and V is the velocity of the fluid.

The cavitation number is significant because it may be used to predict when and how severely cavitation will develop around a propeller blade. A higher cavitation number denotes a reduced probability of cavitation, whereas a lower cavitation number denotes a higher probability of cavitation. Hence, it is possible to reduce the danger of cavitation damage and increase propeller efficiency by designing propellers that operate within a safe range of cavitation numbers.

The ideal cavitation number range for a propeller will depend on a number of variables, including the propeller's design, operating circumstances, and fluid parameters. To tailor their propellers' cavitation behavior for particular applications, propeller designers may run computational fluid dynamics (CFD) simulations and perform experimental testing.
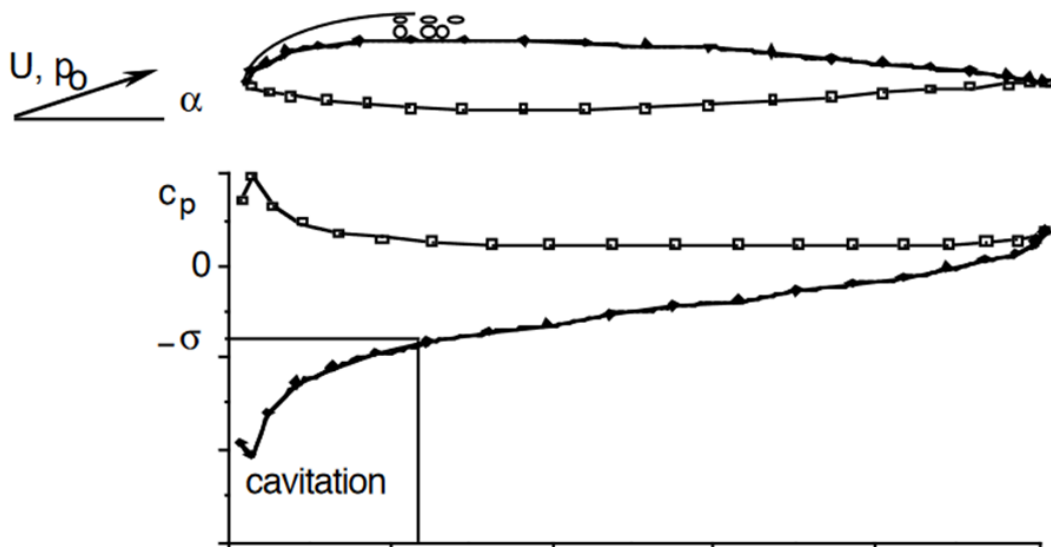
Figure 2.7 Illustration of Cavitating Hydrofoil (Matusiak J., 1992)

The coefficient of pressure c_p is a non-dimensional measurement of the pressure change p_d resulting from dynamic fluid motion brought on by the hydrofoil's presence in the

flow. The term "dynamic pressure" refers to p_d. The cavitation number measures how closely the ambient pressure is to the vapor pressure, which is necessary for cavitation to happen. The hydrofoil is under a total pressure of pressure p, g is the acceleration brought on by gravity, h is the submergence depth, and p_a is air pressure.
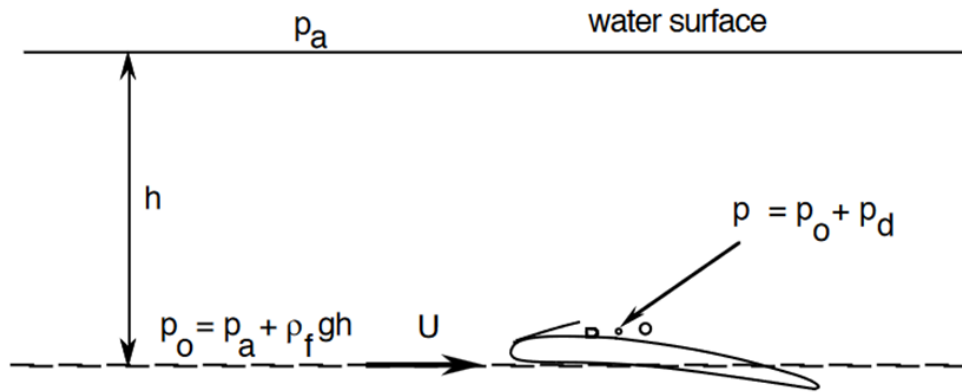
Figure 2.8 Definitions of Pressure (Matusiak J., 1992)

The cavitation at the blade tip area is frequently substantially thicker than that estimated using a two-dimensional flow model, according to cavitation measurements. The tip-vortex cavitation of propellers or the vortex wakes of large transport aircraft are manifestations of the three-dimensional nature of the flow near the blade tip, which can be dangerous for tiny aircraft. The examination of the vorticity roll-up process from lifting surfaces of finite span has been driven by the latter feature. The following assumes that sheet and tip-vortex cavitation, which are merging at the blade tip area, make up fixed cavitation in propellers. Global models of attached or fixed cavitation include both sheet cavitation and tip-vortex cavitation.

There are two flow processes that may result in distinct cavitation bubbles on propellers. The first is connected to the previously mentioned instability of sheet cavitation. The second is related to turbulence in the inflow. A static component is overlaid with a randomly varying pressure at high Reynolds numbers, which causes the flow to be turbulent. Peak total pressure values randomly decrease below the essential vapor pressure threshold in both time and space. The expansion and deflation of the microbubbles (air nuclei) confined by the inflow are driven by these rapid pressure oscillations. As a result, the blades begin to erode significantly and become noisy.
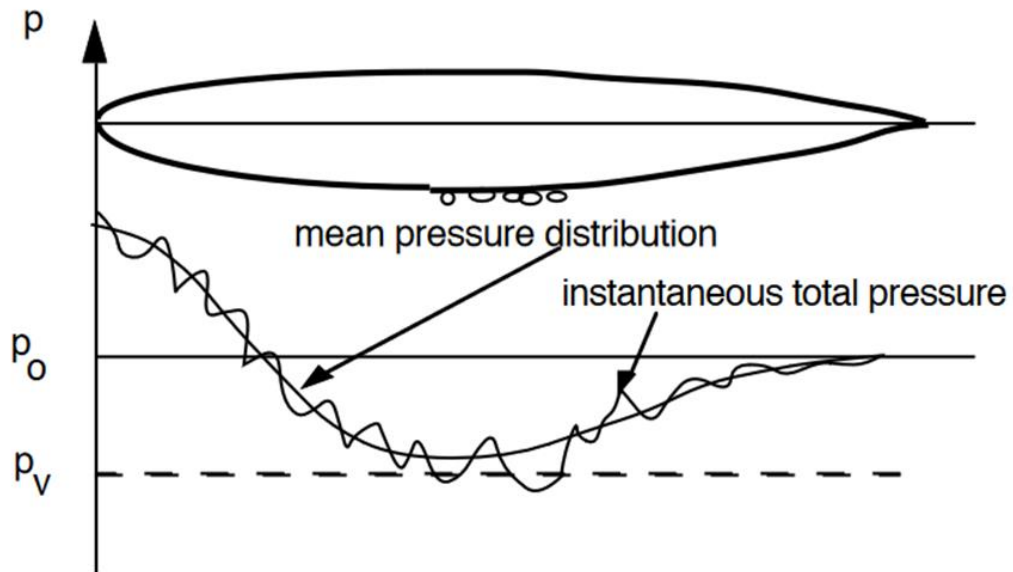
Figure 2.9 Pressure Distribution on Hydrofoil (Matusiak J., 1992)

2.3.1. Effect of Cavitation on Propeller Performance

Despite the simplicity of the sheet cavity model proposed by Yin Lu Young (2009), it remains a commonly used model for analyzing the behavior of propeller blades. The constant vapor pressure assumption within the sheet cavity is seen as a reasonable approximation in many cases, which makes it easier to apply potential flow theory to predict the behavior of the propeller. However, Tulin et al. (2010) argue that more complex models are needed to account for the various types of cavitation that can occur, such as tip or hub vortex cavitation. Additionally, phenomena like wake roll-up have been overlooked in the past and need to be considered for a more accurate analysis of propeller blade behavior.

2.3.2. Scale Effect of Cavitation

Szantyr J.A. (2006) carried out a study to examine particular scale-related phenomena that occur during cavitation experiments involving a model of a marine propeller. These scale effects arise due to the inevitable differences between the flow phenomena of the model and those of the full-scale version. He found out that the majority of the scale effects observed are significant mainly in initiating cavitation on marine propellers and have less significance in the fully developed cavitation phenomena. He also observed that the impact of boundary layer scale effect, object size, velocity and time scale effect leads to under-prediction of the full-scale cavitation.

2.4. Computational Fluid Dynamics

CFD has been used extensively for research and problem solving in various fields of engineering. CFD is a branch of fluid mechanics that is used to solve problems related to fluid flow by making use of different algorithms and numerical methods to solve the governing equations. CFD uses computers in order to simulate and analyze the fluid flow. CFD is based on the approximate solution of fundamental governing equations of fluid dynamics: continuity, momentum and energy equations. Fluid dynamics is based on three fundamental physical principles: conservation of mass, momentum, and energy. A mathematical model is developed using these fundamental physical principles where there are expressed as partial differential equations (PDE) which are solved using numerical methods. The PDEs are replaced by discretized algebraic equations which are then solved with the help of computers with large memories and high processing power. CFD delivers an approximate estimation of fluid flow by the means of:

- Mathematical modelling
- Numerical method
- Software tool

To simulate fluid flow using computational fluid dynamics (CFD), mathematical modeling is first used to create a mathematical representation of the physical system. This involves developing complex equations to describe the behavior of fluid flow, which typically include equations for mass, momentum, and energy conservation. Numerical methods are then used to solve these equations by dividing the fluid domain into a grid of cells and iteratively solving the equations at each cell. Various numerical methods can be used for CFD, such as finite difference, finite volume, and finite element methods. Finally, software tools are employed to implement the numerical methods and solve the mathematical equations. These tools can range from simple programming languages to dedicated CFD software packages that provide a user-friendly interface for setting up and running simulations, as well as tools for analyzing and visualizing the results. Overall, CFD delivery means involve creating mathematical models, using numerical methods to solve equations, and employing software tools to implement the numerical methods and analyze results.

In order to analyze the fluid flow, different commercial CFD packages software are available. They provide a user interface to enter the input parameters and provide facilities to obtain and study the results. All the process is done with the help of CFD codes which is composed of the following elements:

- Pre-processor
- Solver
- Post-processor

With the given input parameters, it solves the problem and shows the results. Each of these three elements have their own functions which will be described in detail henceforth.

Different commercial CFD codes are available, some are paid and some are available for free as student version license. ANSYS CFX and ANSYS Fluent are the widely accepted commercial CFD codes available as free student version license. ANSYS CFX is a Finite Volume Method (FVM) solver that uses a vertex-centered approach while ANSYS Fluent is a Finite Volume Method solver that uses cell-centered approach. FVM discretizes the conservation form of the PDE. Both of these solvers are control volume-based solvers, which ensures conservation of flow quantities.

2.4.1. Governing Equations

Normally, all of CFD is based on mass, momentum and energy equations. CFD solver such as ANSYS Fluent solves Navier Stokes equation in order to obtain the solution. The Navier-Stokes equations were developed by Claude-Louis Navier and George Gabriel Stokes in the 19th century to explain the behavior of fluids (liquids and gases) in motion. These equations explain how the velocity, pressure, temperature, and density of a fluid change over time and space. They embody the principles of mass conservation, momentum conservation, and energy conservation. Specifically, they describe how fluids behave in terms of their movement and physical properties. Navier Stokes equation include:

Mass conservation equation

The continuity equation, which is derived from the principle of mass conservation, describes the net rate of mass flow in and out of a fluid element.

$$\frac{\partial(\rho)}{\partial t} + \frac{\partial(\rho x)}{\partial x} + \frac{\partial(\rho v)}{\partial v} + \frac{\partial(\rho \omega)}{\partial \omega} = 0$$

Equation 2.8

Momentum conservation equation

The momentum equation accounts for both internal and external forces affecting a fluid, such as pressure and viscosity.

$$\frac{\partial(\rho u)}{\partial t} + \frac{\partial(\rho u^2)}{\partial x} + \frac{\partial(\rho uv)}{\partial y} + \frac{\partial(\rho uw)}{\partial z} = -\frac{\partial p}{\partial x} + \frac{1}{Re_r}\left[\frac{\partial \tau_{xx}}{\partial x} + \frac{\partial \tau_{xy}}{\partial y} + \frac{\partial \tau_{xz}}{\partial z}\right]$$

Equation 2.9

$$\frac{\partial(\rho v)}{\partial t} + \frac{\partial(\rho uv)}{\partial x} + \frac{\partial(\rho v^2)}{\partial y} + \frac{\partial(\rho vw)}{\partial z} = -\frac{\partial p}{\partial y} + \frac{1}{Re_r}\left[\frac{\partial \tau_{xy}}{\partial x} + \frac{\partial \tau_{yy}}{\partial y} + \frac{\partial \tau_{yz}}{\partial z}\right]$$

Equation 2.10

$$\frac{\partial(\rho v)}{\partial t} + \frac{\partial(\rho uw)}{\partial x} + \frac{\partial(\rho vw)}{\partial y} + \frac{\partial(\rho w^2)}{\partial z} = -\frac{\partial p}{\partial z} + \frac{1}{Re_r}\left[\frac{\partial \tau_{xz}}{\partial x} + \frac{\partial \tau_{yz}}{\partial y} + \frac{\partial \tau_{zz}}{\partial z}\right]$$

Equation 2.11

Energy conservation equation

The energy equation explains how thermal energy is transferred within the fluid and converted from mechanical energy.

$$\frac{\partial(E_T)}{\partial t} + \frac{\partial(uE_T)}{\partial x} + \frac{\partial(vE_T)}{\partial y} + \frac{\partial(wE_T)}{\partial z}$$
$$= -\frac{\partial(up)}{\partial x} - \frac{\partial(vp)}{\partial y} - \frac{\partial(wp)}{\partial z} - \frac{1}{Re_r Pr_r}\left[\frac{\partial q_x}{\partial x} + \frac{\partial q_y}{\partial y} + \frac{\partial q_z}{\partial z}\right]$$
$$+ \frac{1}{Re_r}\left[\frac{\partial}{\partial x}\left(u\tau_{xx} + v\tau_{xy} + w\tau_{xz}\right) + \frac{\partial}{\partial y}\left(u\tau_{xy} + v\tau_{yy} + w\tau_{yz}\right)\right.$$
$$\left. + \frac{\partial}{\partial z}\left(u\tau_{xz} + v\tau_{yz} + w\tau_{zz}\right)\right]$$

Equation 2.12

These equations provide valuable information on fluid behavior and physical properties and are used in various fields, including aerospace and oceanography.

2.4.2. Steps of CFD

Pre-Processor

Pre-processing is the preliminary step of a CFD simulation in which the parameters of the simulation are defined. Pre-processing stage involves activities such as preparation of the geometric model of the fluid problem using a CAD software, dividing it into finite elements, i.e., mesh generation, material property definition, and input of the boundary conditions. In order to get accurate results, the geometric model must be an accurate representation of the actual system. The geometry can be modelled using CAD software such as SolidWorks, CATIA, and Autodesk Inventor etc. Meshing can be done using software such as ANSYS ICEM CFD, GAMBIT, TurboGrid etc. For the analysis of the fluid flow, the flow domain is split into discrete elements, which is known as grid generation. Such discrete representation of a domain is called mesh or grid. For more accurate results, the cells must be as small as possible, i.e., the mesh must be as fine as possible.

Solver

Solvers such as ANSYS Fluent are software which provide the user an interface for selecting and setting the material properties, initial conditions, boundary conditions and other parameters as required to solve the governing equations of the flow subject in order to obtain the output solution. For solving the governing equations of fluid motion, a numerical analogue is generated by numerical discretization. Flow solvers use these four different methods for numerical discretization:

- Finite Difference Method
- Finite Element Method
- Finite Volume Method
- Spectral Method

All these methods differ from each other by the discretization processes involved. ANSYS Fluent solver, which is used for this study, uses the finite volume method for numerical discretization.

Post-Processor

Post-processing is the analysis stage of CFD in which the results are analyzed. In order to analyze the results, various tools and visualization techniques are available, some of which are listed as follows:

- Contour plots
- Velocity vectors
- Graphs and charts
- Particle tracking

2.4.3. Types of CFD meshes

There are several types of meshes that can be used for computational fluid dynamics (CFD):

Structured mesh: A structured mesh is a type of mesh that has a clearly defined structure and is made up of rectangular or curvilinear cells arranged in a grid pattern. These meshes are often used in straightforward shapes with regular geometries, like channels or ducts.

Unstructured mesh: An unstructured mesh is a type of mesh that is more adaptable and suitable for simulating intricate geometries, such as those encountered in aerodynamics or automotive engineering. These meshes are composed of cells with different shapes and sizes that are not arranged in a regular pattern.

Hybrid mesh: In a hybrid mesh, the structured and unstructured meshes are combined to leverage the benefits of both. The structured portion of the mesh can be utilized in areas where the geometry is regular, while the unstructured part can be employed in more intricate regions.

Polyhedral mesh: A polyhedral mesh is an unstructured mesh made up of polyhedra, which are 3D shapes with flat polygonal faces. These meshes are proven to be more effective and precise compared to conventional tetrahedral or hexahedral meshes in certain types of simulations.

2.4.4. Mesh Quality Metrics

To evaluate whether a Mesh is appropriate for simulations, we use a set of quality metrics to measure the mesh quality. The main goal of these metrics is to determine if a mesh enhances at least one of the crucial simulation properties, such as convergence time, stability, or accuracy, without causing negative impacts on the others. Consequently, a mesh that achieves this objective is typically considered to be of better quality than another mesh. Some of the mesh quality metrics used are:

Aspect Ratio

The aspect ratio refers to the comparison between the longest and shortest lengths of a cell. An ideal aspect ratio is 1, and the smaller it is, the better the quality of the element.
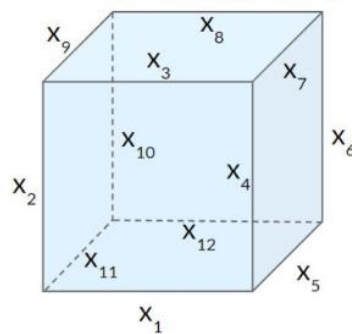
Figure 2.10 Cell with low Aspect Ratio (simscale)
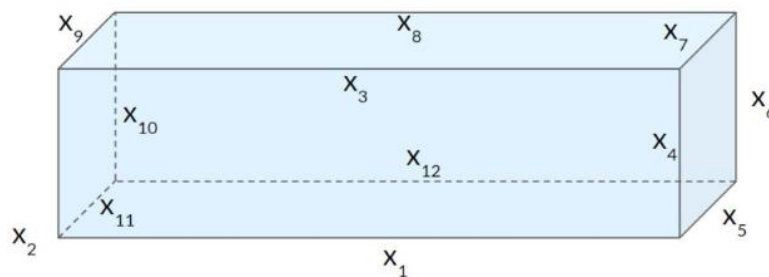
Figure 2.11 Cell with high Aspect Ratio (simscale)

Non-Orthogonality

Non-orthogonality refers to the degree of angle between the normal of the face shared by two adjacent cells and the vector connecting their centers. The non-orthogonality ranges from 0 (ideal) to 90 (worst), with 0 indicating that the mesh is orthogonal. High levels of non-orthogonality should be avoided since they can lead to numerical

26

instability, causing simulations with higher non-orthogonality to take longer to converge or even diverge.
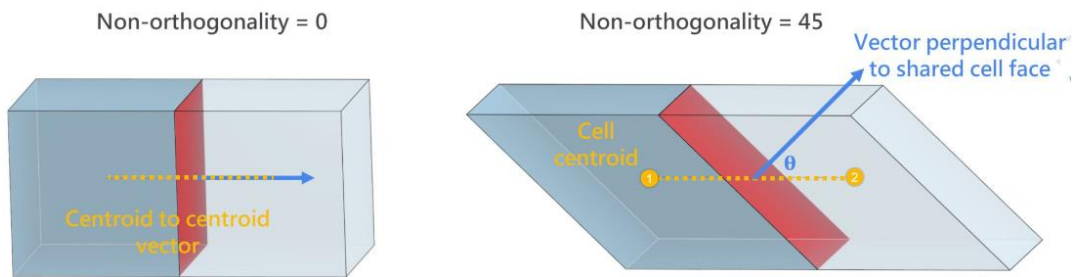
Figure 2.12 Representation of Non-orthogonality Mesh Quality Metric (simscale)

Skewness

Skewness refers to the difference between the ideal cell size and the actual cell size. The skewness value ranges from 0 (ideal) to 1 (worst). Cells that are highly skewed are not desirable because they can cause inaccuracies in the interpolated regions, leading to poor accuracy.
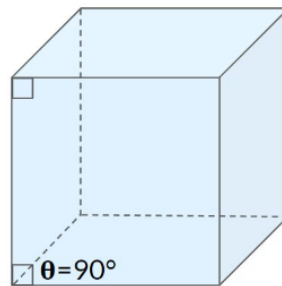
Figure 2.13 Hexahedral Cell with 0 Skewness (simscale)
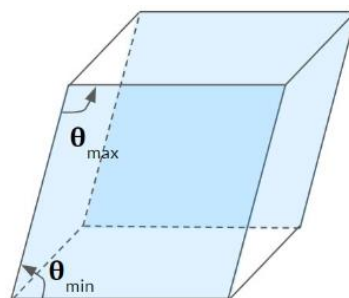
Figure 2.14 Hexahedral Cell with High Skewness (simscale)

2.4.5. Sliding Mesh

Sliding mesh method is used to compute time-accurate solution for flows involving rotational or linear relative velocities between two domains. Two or more cell zones are used, which are bounded by interface zones at regions of contact. A mesh interface is formed between separate cell zones. All the walls and boundaries of a cell zone move without deformation in rigid-body motion. The mesh interface must be such that it maintains perfect contact throughout its motion. Dynamic mesh method is required only for cases that must consider deformation of meshes. Sliding mesh approach is simple and more efficient for this case as deformation is not taken into account. (Ansys Users Guide, 2022)

2.4.6. Commercial CFD Codes

ANSYS CFX and ANSYS Fluent are commonly used solvers which can be used to solve fluid flow problems and for erosion analysis. ANSYS Fluent 2022 R1 was chosen for this study as the CFD solver.

2.4.7. Turbulence Modelling in CFD

Reynolds (Ensemble) Averaging:

Although the potential of Navier-Stokes equations to explain the nature of fluid motion, they are very complex to solve analytically. The Navier-Stokes equations are a group of mathematical equations (PDEs) that are used to explain how fluids like water and air move. Because of the complex nature of the equations and wide range of time scales involved, solving NS equations for practical engineering applications is challenging. One way to simplify the problem is to use the Reynolds-averaged Navier-Stokes (RANS). Reynolds averaging is a method commonly employed in the study of fluid mechanics to split the instantaneous component of fluid flow into two quantities: a mean or average component and a fluctuating component, an idea proposed by Osborne. The main purpose of Reynolds averaging is to separate a fluid flow into a time-averaged mean component and a fluctuating component that describes the unpredictable variations in the flow around the mean. This technique is widely used in fluid mechanics to analyze and understand turbulent flows, which are inherently complex and unpredictable.

For example:

For velocity components,

$$u_i = \bar{u}_\iota + u_i'$$

Where $\bar{u}_\iota$ and u_i' are the mean and fluctuating velocity components respectively and i= 1, 2, 3…

Similarly, for other related scalar quantities:

$$\phi = \bar{\phi} + \phi'$$

Here ϕ denotes a scalar quantity such as density, pressure, energy.

The process of replacing certain expressions for the flow variables in the continuity and momentum equations with the aim of obtaining averaged equations is called substitution. The ensemble-averaged momentum equations are obtained by averaging the equations over time, while ignoring the mean velocity ($\bar{u}_\iota$). These equations are expressed in Cartesian tensor notation as:

$$\frac{\partial p}{\partial t} + \frac{\partial}{\partial x_i}(\rho u_i) = 0$$

$$\frac{\partial}{\partial t}(\rho u_i) + \frac{\partial}{\partial x_i}(\rho u_i u_j) = -\frac{\partial p}{\partial x_i} + \frac{\partial}{\partial xj}\left[\mu\left(\frac{\partial u_i}{\partial x_j} + \frac{\partial u_j}{\partial x_i} - \frac{2}{3}\delta_{ij}\frac{\partial u_l}{\partial x_l}\right)\right] + \frac{\partial}{\partial xj}\left(-\rho\overline{u_\iota' u_j'}\right)$$

The equations derived from the process of taking an average of the Navier-Stokes equations are known as the Reynolds-averaged Navier-Stokes (RANS) equations. Although they look similar in structure to the original Navier-Stokes equations, the velocities and other variables now represent a time-averaged values. The introduction of additional terms in the RANS equations accounts for the impact of turbulence on the fluid flow. The additional term is called Reynolds stress, $(-\rho\overline{u_\iota' u_j'})$ which must be modeled to close the above equation.
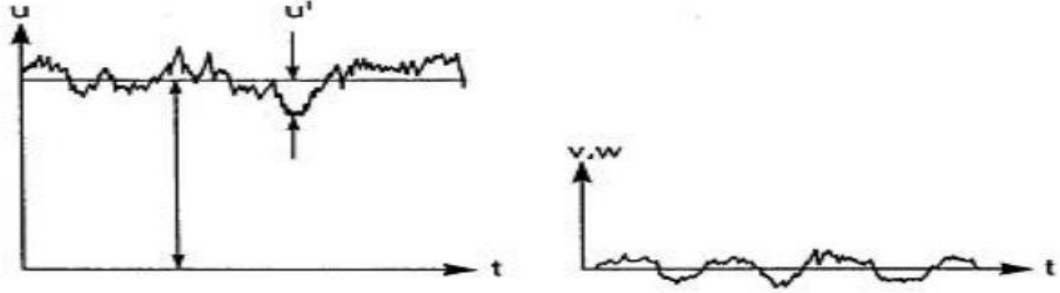
Figure 2.15 Averaging Fluctuations

Reynolds Stress Tensor which gives turbulent stress and adds another six unknowns in the originally existing four unknowns. This requires finding new relations and approximation to resolve these newly added unknowns. The closure problem is used to find additional equations for unknown co-relations. The order of closure is the order of additional differential equations required to solve RANS.

K-ε Standard Model

The k-epsilon (k-ε) turbulence model is the most widely used model in computational fluid dynamics (CFD) for predicting the averaged flow characteristics/properties of turbulent flow. This model utilizes two transport equations to provide a general understanding of turbulence. Following two transport equations provide information regarding turbulence kinetic energy (k) and its dissipation rate (ε):

$$\frac{\partial}{\partial t}(\rho k) + \frac{\partial}{\partial x_i}(\rho k u_i) = \frac{\partial}{\partial x_j}\left[\left(\mu + \frac{\mu_t}{\sigma_k}\right)\frac{\partial k}{\partial x_j}\right] + G_k + G_b - \rho\varepsilon - Y_m + S_k$$

Equation 2.17

And,

$$\frac{\partial}{\partial t}(\rho\varepsilon) + \frac{\partial}{\partial x_i}(\rho\varepsilon u_i) = \frac{\partial}{\partial x_j}\left[\left(\mu + \frac{\mu_t}{\sigma_\varepsilon}\right)\frac{\partial\varepsilon}{\partial xj}\right] + \frac{\varepsilon}{k}CG_k + (3\varepsilon^{G_b}) - c_{2\varepsilon}\rho\frac{\varepsilon^2}{k} + s_\varepsilon$$

Equation 2.18

The equations contain three terms, where signifies G_k how much of the turbulence kinetic energy is produced by the mean velocity gradients. G_b refers to how much of turbulence kinetic energy is produced due to buoyancy, while Y_m is the contribution of fluctuating dilatation to the total dissipation rate in compressible turbulence.

30

The k-epsilon model was originally developed to improve upon the mixing-length model and as a substitute for mathematically determining turbulent length scales in flows that have moderate to high levels of complexity.

Two-equation models are considered the most basic "full models" of turbulence. These models use two separate transport equations to determine the turbulent length and velocity scales independently. The standard k ε model, which is part of this class of turbulence models and was initially proposed by Launder and Spalding, has become the most commonly used model for engineering flow calculations. It is widely used in FLUENT software. The reason for the widespread use of the k-epsilon model in industrial flow and heat transfer simulations is due to its strong and dependable nature, efficiency, and ability to accurately simulate a broad range of turbulent flows. The model is a semi-empirical one, and it uses a combination of phenomenological and empirical methods to develop its equations.

During the development of the K-epsilon model, it was assumed that the flow is completely turbulent and that the impact of molecular viscosity is insignificant. As a result, the standard K-epsilon model is only appropriate for fully turbulent flows.

Improvements have been made to the model to enhance its performance as the model's advantages and disadvantages have come to light. The RNG k-epsilon model and the realizable k-epsilon model are two of these variations that are offered in FLUENT.

This model uses two transport equations, one for turbulent kinetic energy and another for turbulent dissipation rate and applies various closure assumptions to relate these variables and their gradients to the eddy viscosity. The transport equation for one of the variables in the k-epsilon model is derived from the exact equation using mathematical methods. In contrast, the transport equation for the other variable is obtained using physical reasoning and differs significantly from its mathematically exact equivalent. The k-epsilon model is highly versatile and is capable of modeling a wide range of turbulent flows while being computationally less expensive than more advanced turbulence models.

The k-epsilon turbulence model is based on several assumptions, such as a high Reynolds number and turbulence equilibrium in boundary layers where production is equal to dissipation. However, these assumptions can restrict the accuracy of the model as they are not always applicable. For example, the model may not provide precise

results for flows with adverse pressure gradients, and it may underestimate the extent of recirculation zones. Moreover, the k-epsilon model has demonstrated poor agreement with experimental data in simulations of rotating flows. Despite these limitations, the k-epsilon model remains widely used since it requires less computational power compared to more complex turbulence models.

To accurately use the k-epsilon model, a finer mesh is generally required compared to laminar flow simulations. This is because the model must capture the smaller scale of turbulent eddies, which require a finer mesh to be resolved. The mesh must also be fine enough to accurately capture regions of high shear stress and boundary layers. A mesh with sufficient resolution must be used to capture the complex geometry of the propeller accurately. This mesh must be refined enough to capture the boundary layer and other regions of high shear stress, while still being coarse enough to allow for a feasible computational cost.

K-ω standard model:

The K-ω turbulence model is commonly used in computational fluid dynamics (CFD) simulations to model turbulent flows. It is an improvement over earlier turbulence models, such as the standard k-epsilon model, because it is more accurate for boundary layer flows and has fewer assumptions.

The K-ω model is a two-equation model, meaning it solves for two additional transport equations, one for turbulent kinetic energy (K) and another for a specific dissipation rate (ω). These equations describe the evolution of turbulence quantities in the flow field and provide a closure for the Reynolds-averaged Navier-Stokes (RANS) equations.

Following two transport equations provide the turbulent kinetic energy (k) and specific dissipation rate (ω):

$$\frac{\partial}{\partial t}(\rho k) + \frac{\partial}{\partial x_i}(\rho k u_i) = \frac{\partial}{\partial x_j}\left(\Gamma_k \frac{\partial k}{\partial x_J}\right) + G_k - Y_k + + G_b$$

$$\frac{\partial}{\partial t}(\rho\omega) + \frac{\partial}{\partial x_i}(\rho\omega u_i) = \frac{\partial}{\partial x_j}\left(\Gamma_\omega \frac{\partial\omega}{\partial x_j}\right) + G_\omega - Y_\omega + s_{\omega + G_{\omega b}}$$

The production of turbulent kinetic energy due to averaged velocity gradients is represented by G_k while G_ω tells us about the generation of turbulent frequency (ω). Effective diffusivity of k and ω is represented by Γ_ω and Γ_k respectively. While Y_k and Y_ω tell us about the dissipation of k and ω due to turbulence. s_k and s_ω are user-defined source terms.

The K-ω model assumes that the turbulent kinetic energy and the turbulent frequency are related and that their ratio can be used to define a length scale for the turbulent eddies. This length scale is then used to calculate the turbulent viscosity, which is required to close the RANS equations.

The K-ω model has several advantages over other turbulence models. It is better suited for boundary layer flows, which are common in engineering applications, and it has fewer assumptions than earlier models, making it more accurate. Additionally, the K-ω model is more robust than other models, meaning it is less likely to produce unphysical results, such as negative values for turbulent quantities.

Despite its advantages, the K-ω model does have some limitations. It is still a model and not a perfect representation of reality, and its accuracy depends on the specific flow conditions and geometry. The K-omega turbulence model is a widely used in literature and popular among researchers. It assumes that the ratio of these quantities defines the length scale for turbulent eddies, which is then used to calculate turbulent viscosity. The K-omega model is suitable for boundary layer flows, provides accurate predictions of near-wall turbulence, has fewer assumptions than earlier models, and is more robust, which means it is less likely to produce unphysical results. However, as with any turbulence model, it needs to be validated against experimental data to ensure accuracy for specific applications.

Despite being used in CFD simulations widely, it has several limitations and assumptions that should be taken into account. For example, it is developed primarily for wall-bounded flows, and its accuracy may be reduced in other types of flows.

Additionally, the model assumes that turbulence is isotropic and neglects the effects of pressure gradient. The accuracy of the model also depends on its constants, which may need to be calibrated for each specific application. Overall, while the k-ω turbulence model is a useful tool for moderate to high Reynolds numbers, it should be applied with caution and awareness of its limitations.

K- ω SST:

The k-ω SST (Shear Stress Transport) turbulence model is a successor of the k-ω turbulence model. It is also widely used turbulence model in CFD simulations. The k-ω SST model blends the benefits of both the k-ω and k-ε turbulence models, making it more accurate and reliable for simulating various turbulent flows.

The k-ω SST model solves two separate transport equations for the turbulent kinetic energy (k) and specific dissipation rate (ω). The model uses a blending function to determine which equation should be used in different regions of the flow. For regions where the flow is attached to a solid surface, the k-ω model is used to capture the boundary layer dynamics or wall bounded types of flows. In regions where the flow is separated, the k-ε model is used to account for the high levels of turbulence. The blending function smoothly transitions between these two models to provide accurate results throughout the flow. The blending function is a mathematical function that ranges from 0 to 1 and is dependent on the distance from a solid surface and turbulence intensity. When the blending function equals 1, the k-ω model is used to solve the turbulent kinetic energy equation, which is ideal for attached flow to a solid surface with a relatively thin boundary layer. This accurately captures the dynamics of the boundary layer. But when the blending function is 0, the k-ε model is used to solve the turbulent kinetic energy equation. This is better suited for regions with high turbulence levels and flow separation.

One of the key features of the k-ω SST model is the use of the shear stress transport equation. This equation accounts for the effects of the Reynolds stresses, which are important in regions with high level of turbulence. The shear stress transport equation is used to model the transport of these Reynolds stresses, improving the accuracy of the model in such regions.

The k-ω SST (Shear Stress Transport) turbulence model is a commonly used tool in computational fluid dynamics simulations for marine propellers. Its accuracy in

predicting the performance and hydrodynamic loads of marine propellers is due to several features and capabilities. These include its ability to accurately predict boundary layer dynamics, separated flows, and turbulent wakes, as well as its robustness and stability in simulating complex flows. Additionally, the k-ω SST model is suitable for unsteady simulations, which are important for predicting the behavior of marine propellers under realistic operating conditions.

2.4.8. Cavitation Modelling

With the growth in ship load capacity, the degradation of hydrodynamic performance caused by propeller cavitation is becoming a highly serious concern. Different models were created to forecast cavitation erosion utilizing numerical methods for real-world and macro-scale hydrodynamic flow problems. The operating environment for ship propellers varies greatly from one another. Cavitation happens on practically every maritime propeller, notwithstanding the unique propellers of research on military vessels. As a result, numerous kinds of cavitation may happen on various ship appendages, particularly the propeller. The leading edge, blade tip, and hub of the propeller are where cavitation in propellers most frequently occurs. The pressure or suction side of a blade may produce cavitation depending on the operating circumstances. The blades are exposed to various angles of attack for each position during one rotation due to the propeller rotation and the uneven flow in front of the propeller. This cyclical variation in the flow conditions at the blades could lead to generation and collapse of cavitation structures.

Many fluid dynamics models that are used for cavitation studies assume fluid as a single-phase compressible fluid. This approach uses barotropic equation of state $\rho = \rho(p)$, with continuous variation of density between liquid and vapor, centered on the vapor pressure. Such approaches are attractive due to their simplicity.

The formation of cavitation is due to the growth of small nuclei, containing mixture of vapor and gases. The collapse of these rapidly growing bubbles depends on various number of variables, including surface tension, viscosity, and non-condensable content. No models exist that account for all the factors affecting the collapse phase of cavitation. Using Rayleigh-Plesset equation, some models attempt to account for the non-equilibrium effects.

Multiphase Models

Many types of flows consist of non-uniform composition and distribution of materials. These types of flows are modelled by multiphase models. According to Ansys Theory Guide 2022, multiphase flows can be broadly classified as:

1. Gas-Liquid or Liquid-Liquid Flows
2. Gas-Solid Flows
3. Liquid-Solid Flows
4. Three-Phase Flows

Cavitation involves only liquid phase and vapor phase, so it belongs to the first category.

In Ansys Fluent, there are two approaches to modelling Multiphase Flows:

1. Euler-Lagrange Approach

   This is the discrete phase model in Ansys Fluent. In this model, first the fluid phase is solved to obtain the flow field. Using the flow field, number of particles are tracked to obtain the dispersed phase solution.

2. Euler-Euler Approach

   a. VOF Model

      This model tracks the volume fraction and interface between two immiscible fluids. All phases in the multiphase system share the same momentum equations.

   b. Mixture Model

      In mixture model, momentum, continuity and energy equations are solved for the mixture. Relative velocities are solved using algebraic equations. Due to smaller number of variables than full Eulerian multiphase model, it is a good alternative for most cases. Singhal et al. cavitation model is only available in mixture model.

   c. Eulerian Model

      This is the most complex multiphase model in Ansys Fluent. Momentum and continuity equations are solved separately for each phase. Coupling between phases is done on the basis of the types of materials involved.

Bulten et al. (2006) used CFD to predict cavitation formation at propeller tip. With detailed analysis of tip vortex, cavitation formation was predicted reasonably at model-scale level. This method shows good agreement with results from multiphase capabilities of advanced commercial packages.

A three-dimensional sheet cavitation model has been developed by Vaz and Bosschers (2006). On Matin S propeller, this model predicted cavity extent accurately at moderate loadings but not at low loadings. In Rome 2008, models based on RANS and LES solvers were shown to have good qualitative similarity with measured values, but quantitative differences were found. Different cavitation models have been used in commercial software with good prediction. Liu et al. (2008) used FLUENT 6.2 with a full cavitation model with Singhal et al (2002) characterization. The SST k-ω turbulence model has been used by Sato et al. (2009), to reasonably predict fundamentals of sheet cavitation. Using modified SST k-ω model, NACA0015 hydrofoil could be accurately represented (Li et al, 2009). The modified SST k-ω model provided enhanced correlation with standard fluid dynamics.

Various models were created to forecast cavitation erosion using numerical methods for real-world and macroscopic hydrodynamic flow problems. Li's model assesses the pressure on the surface under consideration's temporal derivatives. Where these pressure derivatives surpass a predetermined threshold value, erosion is projected. She demonstrated a qualitative agreement between her numerical erosion forecast and experimental predictions. To create so-called aggression indices, Nohmi et al. (2008) provided a formula. These indicators are dependent on the pressure, the volume fraction, and their temporal derivatives. A low or high value indicates a strong potential for erosion, depending on the index under consideration. The pressure waves emitted by microscopic cloud collapses were taken into account by Fortes-Patella et al. (2004) The cavitation clouds' potential energy is supposedly transformed into pressure waves' acoustic energy, which can harm the surface being struck. They computed the acoustic pressure that the spherical cloud emits in order to determine the erosion potential.

Kimura et al. (2009) and Lu et al. (2012) investigated cavitation on marine propellers using Reynolds-averaged Navier-Stokes (RANS) methods. Their findings were in strong agreement with experimental observations, demonstrating that the behavior and degree of cavitation in a uniformly cavitating flow can be anticipated computationally.

Schmidt et al. (2011) demonstrated that if a high resolution is offered, a Euler-Euler technique may model the collapse dynamics of a single bubble. Schenke and van Terwisga (2017) demonstrated that even a Euler-Euler solver utilizing a mass transfer cavitation model is capable of accurately capturing the bubble collapse time with fine spatial discretization and small time increments.

To study the tip vortex flow, Asnaght et al. (2017) used Implicit Large Eddy Simulation. The results of vortex core pressures and velocity distributions. Kim et al. (2017) deployed an analysis based on viscous/interaction method to study performance of ducted propellers. Both results and computational efficiency of this method compared well with RANS formulation.

The risk of cavitation-induced propeller blade degradation was mathematically examined by Hasuike et al. (2009). In a predetermined wake field, they assessed the occurrence of cavitation erosion on a propeller with four differently loaded blades. Because cavitation volumes collapsed close to the blade surface, simulations and measurements of a test case revealed a larger erosion risk on the less loaded blades. Their numerical forecast was based on the aggressiveness indices suggested by Nohmi et al. whereas their experimental erosion prediction used a painted surface. They were able to forecast qualitative deterioration using these aggression indices. Ponkratov and Caldas (2015) also used the Nohmi et al. indices to forecast cavitation erosion brought on by a ship propeller close to a rudder's leading edge. By modelling the entire ship geometry, these scientists employed detached eddy simulations (DES) to forecast cavitation erosion on a rudder. Full-scale measurements on the rudder revealed that degradation was brought on by the propeller's hub vortex collapsing close to the leading edge. Similar zones of erosion risk were found using the aggressiveness indices. Ponkratov calculated the erosion potential on a full-scale propeller behind the whole ship geometry using the same DES and erosion indices. Full-scale studies of the propeller in operation revealed cavitation-induced degradation on the leading-edge tip. In the numerical simulations, the aggressiveness indices qualitatively addressed the erosion damage. Three approaches to numerically forecast cavitation erosion using various formulas were investigated by Usta et al. (2017). On a four-bladed model propeller, they ran simulations and compared erosion predictions to an experimental prediction approach, which revealed a fair qualitative agreement.

Cavitation occurs when a liquid is exposed to a decreasing pressure, causing it to rupture, even below its saturated vapor pressure. This process can also cause micro-bubbles of non-condensable gases or nuclei within the liquid to grow and form cavities. As a result, significant and sudden changes in density occur in the low-pressure and cavitating regions.

Singhal et al. (2002) developed a cavitation model called the Singhal cavitation model that has been widely used in computational fluid dynamics (CFD) to simulate cavitating flows. Several research have been done to evaluate the accuracy and effectiveness of this model. For example, Kim and Choi (2007) compared the Singhal model with the Zwart-Gerber-Belamri (ZGB) model and found that the Singhal model performed better in predicting cavitation inception and growth. Chen et al. (2015) compared the Singhal model with other models in simulating the cavitating flow around a hydrofoil and concluded that the Singhal model was more accurate in predicting the location and size of the cavitation cloud. The implementation of the Singhal model in different CFD solvers has also been investigated, with Kulkarni et al. (2018) finding that the model exhibited good accuracy and stability in simulating cavitating flows in the OpenFOAM solver. Researchers have also proposed modifications to the Singhal model to account for its limitations, such as compressibility effects, and to improve its accuracy. In summary, the Singhal cavitation model has been extensively validated and has become a reliable tool for simulating cavitating flows in various applications. Ongoing research continues to explore its potential improvements and limitations.

The Singhal cavitation model is a commonly used two-phase flow model that is utilized to simulate the interaction between liquid and vapor phases in cavitating flows. This model is based on the Rayleigh-Plesset equation, which is a mathematical model that describes the behavior of a spherical cavity in a liquid. The Singhal model assumes that the shape of the cavity is spherical and that the only changing variable over time is the cavity radius.

The model employs a transport equation to track the formation, growth, and collapse of vapor bubbles in the liquid. This equation includes a source term that considers the nucleation of vapor bubbles due to pressure fluctuations or other mechanisms. Additionally, the model incorporates a cavitation number, a dimensionless parameter that determines when cavitation begins, which is a function of the local pressure, liquid

density, and speed of sound. If the local pressure drops below a particular threshold, the model predicts the onset of cavitation.

Several closure relationships are included in the Singhal model to account for the effects of turbulence, compressibility, and vapor diffusion. These relationships, which are derived from empirical data and experimental observations, modify the transport equation for the vapor volume fraction and account for the transport of vapor bubbles in the liquid phase.

The Schnerr-Sauer Cavitation model is also a popular method for simulating cavitating flows. It views the fluid as a mixture of a liquid phase and a compressible vapor phase, with the liquid phase being always present and the vapor phase appearing or disappearing depending on local pressure and temperature. The model predicts the onset of cavitation and amount of vapor by simulating pressure drop and nucleation rate. It also includes a transport equation for tracking vapor fraction. This model has been successfully used for simulating various cavitating flows and has provided accurate predictions of vapor distribution and pressure fluctuations. Overall, it's a valuable tool for understanding cavitating flows.

The Schnerr-Sauer Cavitation model utilizes the bubble number density parameter "n_b" to model the growth and nucleation of vapor bubbles in cavitating flows. This parameter represents the number of vapor bubbles per unit volume of the liquid phase and plays a crucial role in determining the rate of bubble growth and coalescence, which affects the overall behavior of the flow. The model includes a transport equation for the bubble number density that considers the effects of bubble growth, coalescence, and nucleation rate. Accurately modeling this parameter is essential for predicting cavitation onset and development in engineering applications, such as pumps, propellers, and fuel injectors. The Schnerr-Sauer Cavitation Model is a reliable tool for predicting bubble number density and other important parameters in cavitating flows, making it a valuable resource for engineers and researchers.

The Schnerr-Sauer and Singhal cavitation models are used to simulate cavitation in fluids but differ in their approach. The former assumes two phases (liquid and vapor) and includes a vapor fraction transport equation and mass transfer, while the latter assumes a single fluid phase with variable thermodynamic properties and uses a liquid pressure transport equation to determine if cavitation occurs based on the comparison

of local vapor and liquid pressures. While the Singhal model offers more detail and accuracy, it is more computationally expensive, whereas the Schnerr-Sauer model is simpler and faster but may not capture all the complexities of cavitation. The choice between these models depends on the desired level of simulation detail and the specific application.

2.4.9. Types of Different Closure Orders

Zero Order (Algebraic Model)

Bossenesque's used an algebraic model to solve RANS. He introduced a new parameter called Eddy viscosity which was used to determine turbulent stresses. Though it works only in limited cases (axis-symmetric jets, 2D jets), dividing flow regimes into different zones with different eddy viscosity provides good approximations. According to his theory, Turbulent Stress is

$$\tau = \mu_{turb} \left(\frac{\partial U}{\partial x} \right)$$

Equation 2.21

It was highlighted that μ_{turb} is larger than fluid dynamic viscosity μ and is property of flow density and condition. This limits the application as it needs more and more experiments to find turbulent viscosity. Prandtl added a new concept in the algebraic model by defining mixing length where he defines the turbulent viscosity in terms of it.

One Equation Model

It uses a first-order differential equation to compute turbulent stresses. Kolmogorov and Prandtl used turbulent kinetic energy per unit mass (k) to evaluate the turbulent shear stress. This model requires a length scale to be specified which is its major drawback due to which two-equation models are required.

Two Equation Model

They are extrapolations of one equation model with the addition of an equation expressing characteristic turbulent length scale for another quantity. They don't require prior knowledge of the length scale. Hence, they are far more appropriate than its predecessor. k-ω and k-ϵ are widely used turbulence model.

CHAPTER THREE: METHODOLOGY
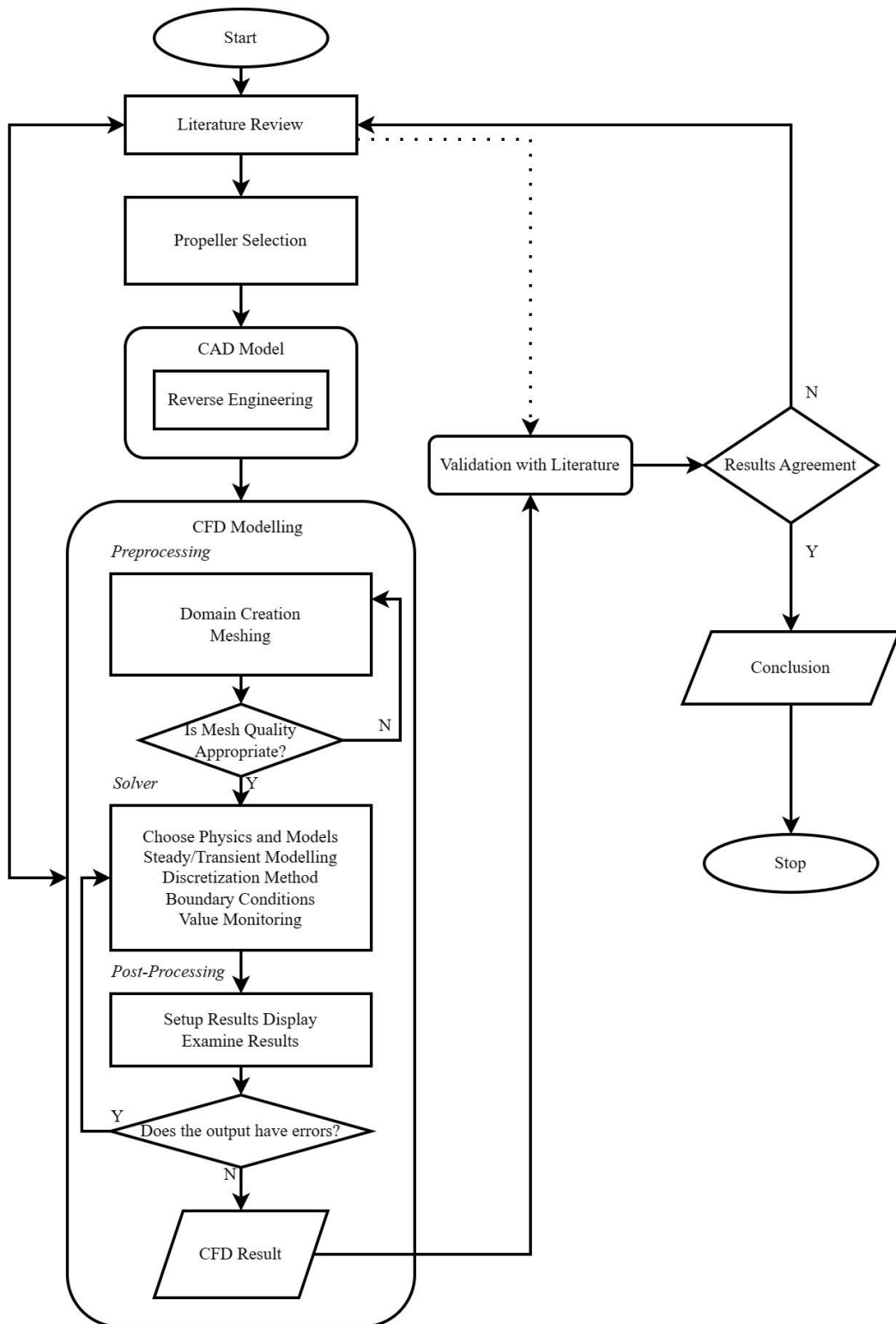
Figure 3.1 Methodology Flowchart

3.1. CAD Modelling

The propeller for the simulation was provided by Nepal Ship and Boat Building Company Pvt. Ltd. located in Gaidakot, Nepal. The propeller was based on a 40 HP, Parsun outboard motor.

The specifications of the propeller are:

Table 1 Specifications of Propeller

Identification marking	3-11 1/8 "X13"
Diameter D	282.575mm
Number of blades (Z)	3
Pitch	330.2mm
Hub Diameter	80mm
Engine speed	800±50 to 5000~6000 rpm
Maximum output	29.4 KW at 5500 rpm
Gear ratio	2.0
Propeller total operating range n	6.6667 to 50 rps

Figure 3.2 Provided Propeller

The propeller was then scanned at Zener Technologies. Using Geomagic Design X, alignment and centering of the facet body was done ensuring symmetry. The initial scanned model had lots of uneven surfaces, discontinuous bodies, and some holes.

Using repair tools in Geomagic Design X, the major defects were fixed first. After the major defects were removed, only blades of the propellers were extracted for further operation. Using other two blades as reference, one of the blades were smoothened and other minor defects were removed. To extract this blade surface into CAD format, 'Create Patch Network' and 'Auto Surface' Tools were used to generate surface for the propeller blade. After adjusting the parameters, a surface that fits the blade well was obtained. The blade surface was imported to Siemens NX, from where rest of the propeller geometry was remade. From this solid model, computational domain was created for simulation in ANSYS.

Figure 3.4 Scanned File   Figure 3.3 Final CAD Geometry
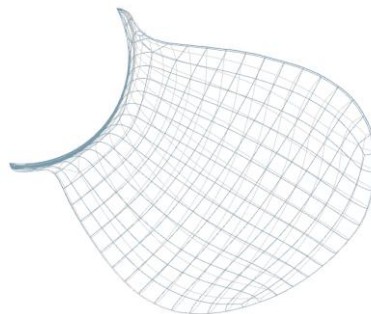
Figure 3.5 Extracted Blade Surface

3.2.   Computational Domain

The computational domain for the simulation is chosen being based on the dimension of the propeller. The reference for the computational domain is taken as suggested by

S. Subhas et al. (2012). A cylindrical enclosure domain with diameter of 4D is taken, while the inlet is at 3D and outlet expanding up to 4D length.
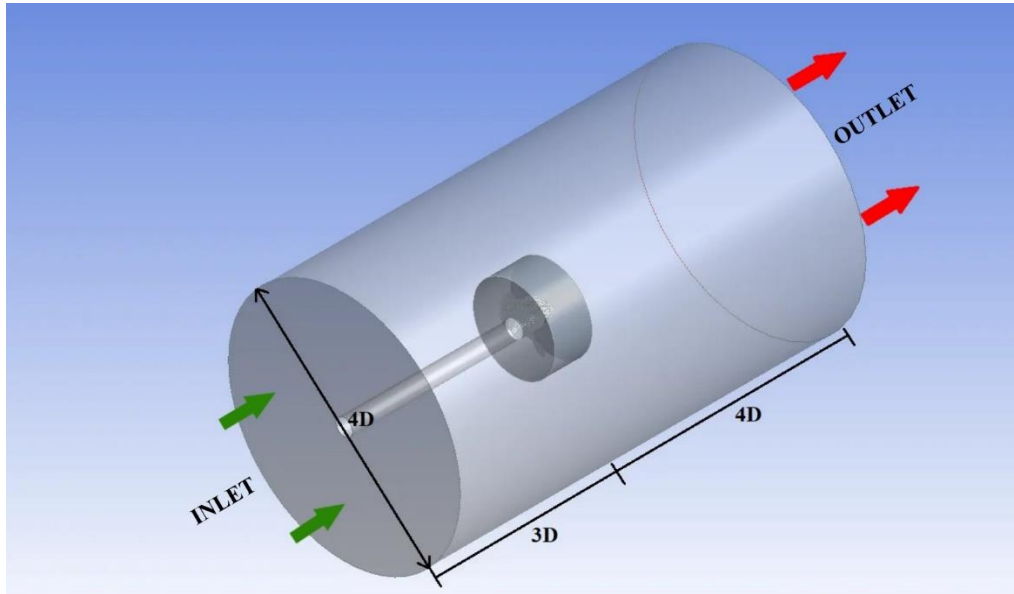
Figure 3.6 Computational Domain

3.3. Grid Generation

3.3.1. Mesh Sizing

For meshing, unstructured tetrahedral cells were generated with ANSYS Fluent Meshing (watertight geometry). For sliding mesh approach, non-conformal mesh of constant sizing was generated at the interface. Mesh sizing was adjusted to be finer on propeller blade edges to better capture flow on critical locations. Inflation layer with 5 layers were grown on propeller surface.

Another polyhedral volume mesh was created for mesh independence test with tetrahedral volume mesh. Three minimum mesh sizes of 1.5mm, 1mm, and 0.8mm mesh elements were chosen for polyhedral mesh. Schnerr-Sauer cavitation model was run on these meshes and the results were compared. The result of the mesh independence test showed that the thrust coefficient (K_T) and Torque coefficient (K_Q) were showing low variation in 1mm size of the polyhedral mesh. The same mesh sizing parameters based on the 1mm grid were used for both meshes used in this study..

Table 2 Mesh Refinement

Number of	Tetrahedra cells	Polyhedral cells		
Cells	2428209	494819	709103	789194
Faces	5243748	2997642	4132078	4553494
Nodes	546871	2202763	2983632	3272769
Thrust	1246.66	1128.79	974.364	963.256
Kt	0.21765	0.19707	0.17011	0.16817
Torque	68.9618	73.8059	65.5842	65.5595
Kq	0.04261	0.0456	0.04052	0.0405
10Kq	0.42607	0.456	0.4052	0.40505
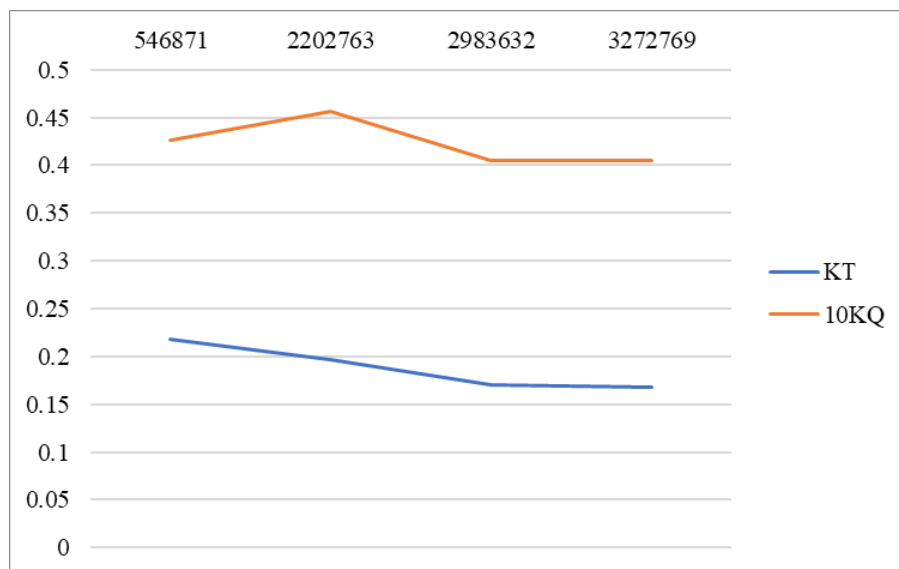
Figure 3.7 Variation of K_T and K_Q with number of nodes.
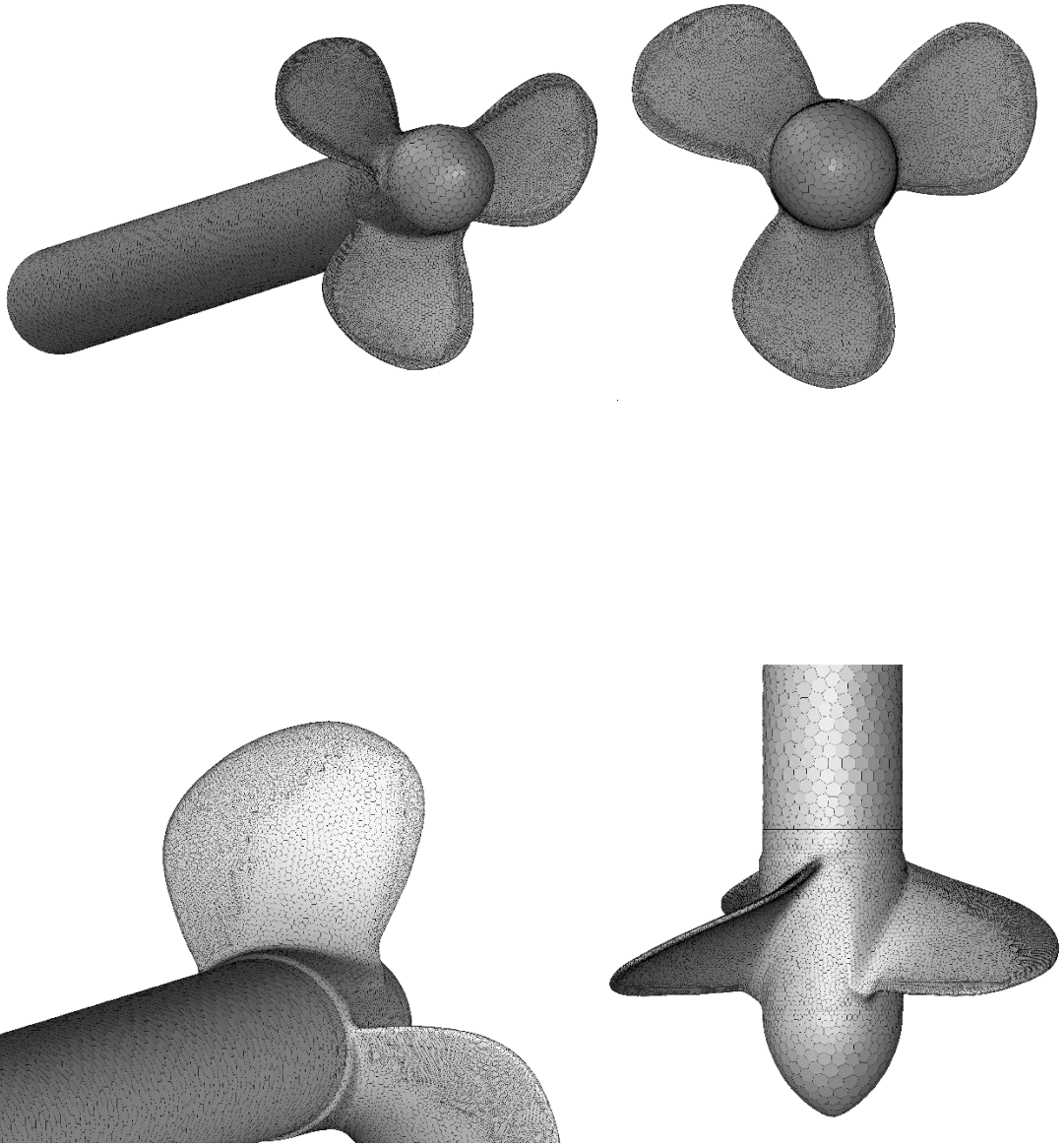
Figure 3.8 Polyhedral Mesh
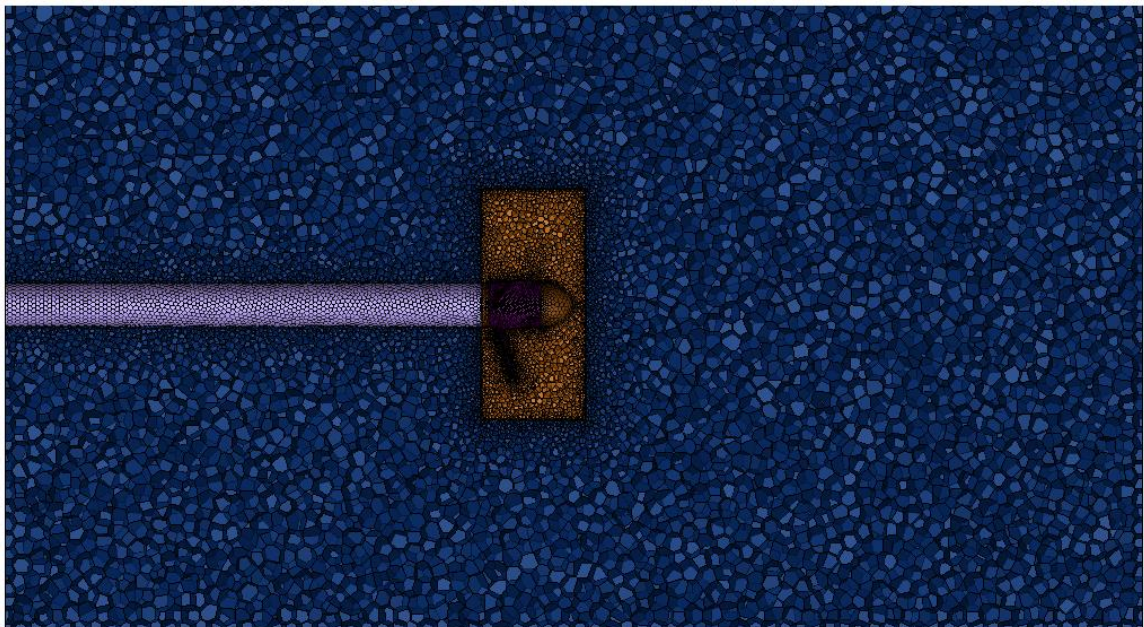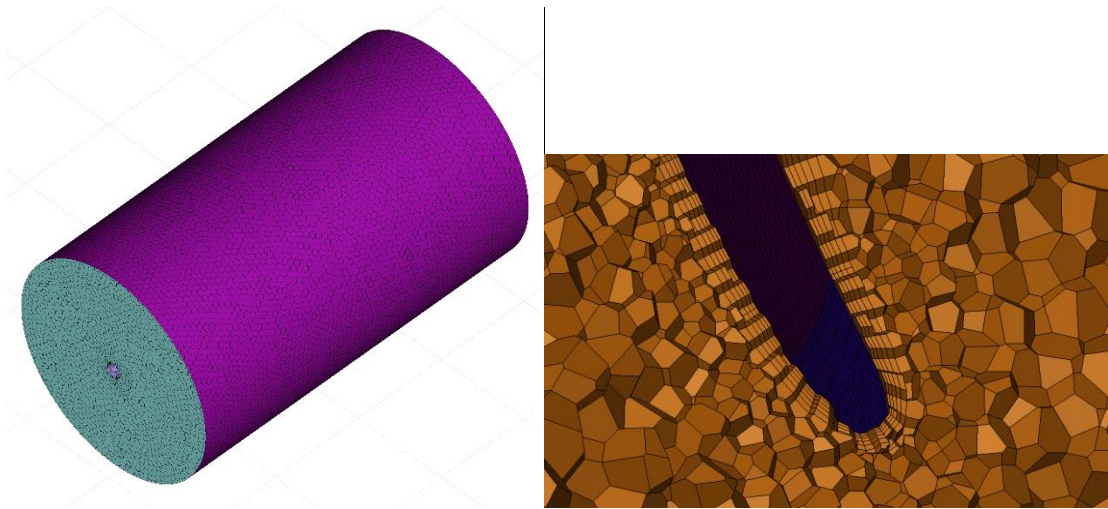
Figure 3.9 Polyhedral Cells in Computational Domain

A polyhedral mesh is a kind of unstructured mesh that discretizes the domain using polyhedrons (3D forms with flat faces). Hexahedrons, tetrahedrons, prisms, and pyramids are just a few examples of the many shapes that these polyhedrons can take. Polyhedral meshes may represent curved surfaces and can be created automatically, making them suitable for complex geometry. Contrarily, structured meshes, which are frequently employed in smaller geometries, are composed of homogeneous, regular

shapes like rectangular or hexagonal cells. Although they are more difficult to create and have better numerical accuracy, structured meshes might not be as effective for complex geometries.

It offers several benefits over other types of mesh such as structured and unstructured meshes. Polyhedral volume mesh is flexible and can represent complex geometries with arbitrary shapes. It is also accurate and can provide better predictions of flow fields and physical properties. Furthermore, it is efficient and can reduce computational costs by reducing the number of cells required to represent a given geometry. Additionally, polyhedral volume mesh has better mesh quality metrics, leading to better numerical stability and convergence properties. Overall, it is a powerful option for CFD simulations and is preferred by many researchers and engineers.

Amjd Ibraheem (2021) studied the effectiveness of polyhedral grids to simulate the flow around ship rudder using a RANS turbulence model (K-ω SST) and compared it to a tetrahedral mesh using ANSYS fluent. Although the limitations of the academic version of the software, it produced satisfying results in estimating the lift and the drag coefficient, the velocity, and the turbulent kinetic energy. The result of his study showed the supremacy of the polyhedral elements in saving time and computational resources and improving mesh quality without much sacrifice of the accuracy in the results.

Polyhedral mesh is derived by the direct formation of polygons around each node of tetrahedral mesh resulting least number of element count compared to tetrahedral and hexahedral mesh elements.

ANSYS FLUENT was used for simulating the open water flow due to its widespread usage by most researchers for marine propeller models and ease in usage. The transient computational fluid analysis of the model was performed by solving 3D RANS equations with a control volume-based technique and K-ω SST turbulence model for turbulence kinetic energy (K) and specific dissipation rate (ω).

3.4. Mesh Statistics

Four mesh quality parameters are presented below: Aspect ratio, Skewness, and Orthogonal quality. These four mesh quality parameters are enough to explain whether high quality meshes are formed or not. Majority of them are within the range of recommended value.

Table 3 Mesh Statistics for Forward Operation

	Orthogonal Quality	Skewness	Aspect Ratio
Minimum	0.2002204	1.6187e-06	1.380058
Average	0.9488667	0.05113333	3.597327
Maximum	0.9999984	0.7997796	17.81117
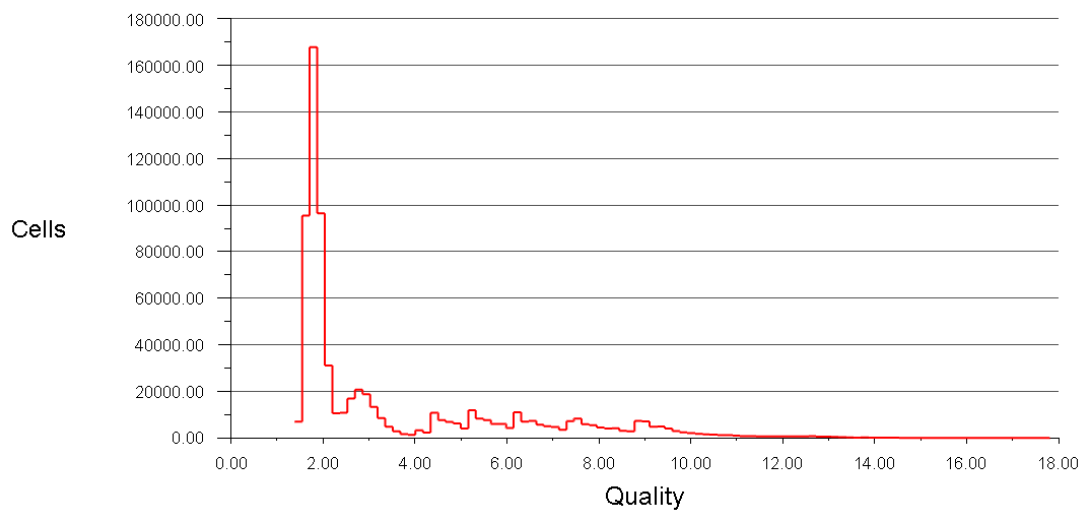
Figure 3.10 Aspect Ratio (Forward Operation)
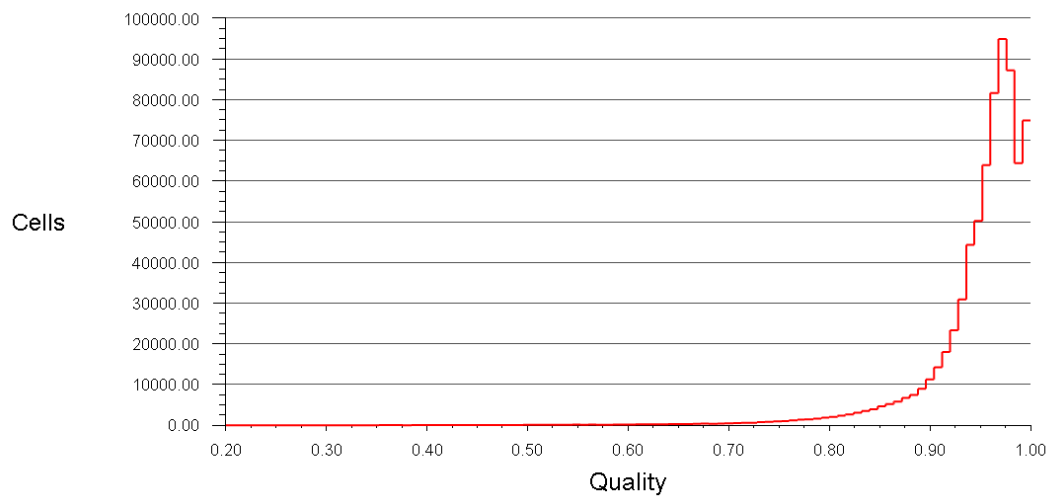
Figure 3.11 Orthogonal Quality (Forward Operation)
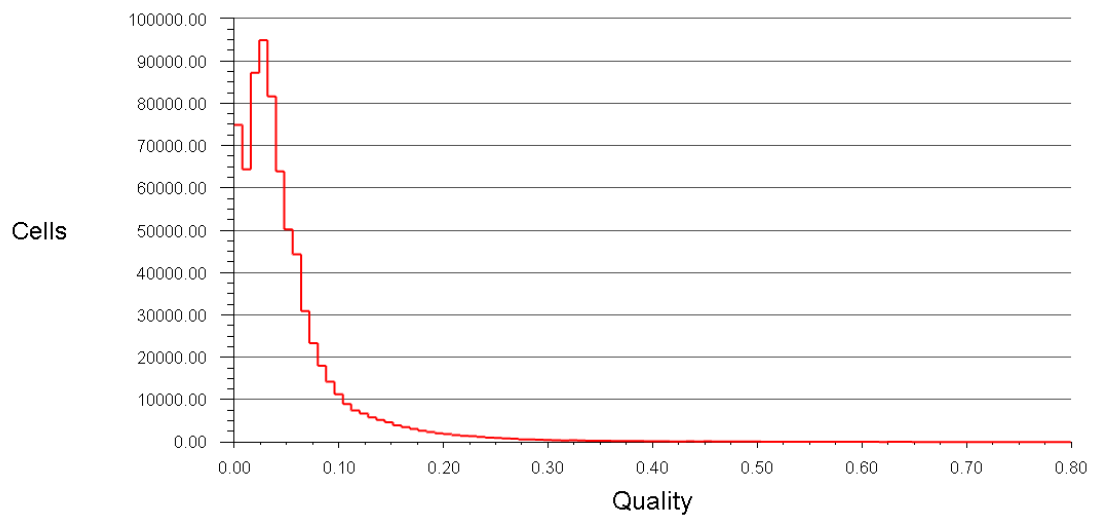
Figure 3.12 Skewness (Forward Operation)

Table 4 Mesh Statistics (Reverse Operation)

	Orthogonal Quality	Skewness	Aspect Ratio
Minimum	0.2001217	1.1009e-6	1.330634
Average	0.9505067	0.04949326	3.815063
Maximum	0.9999989	0.7998783	53.1139
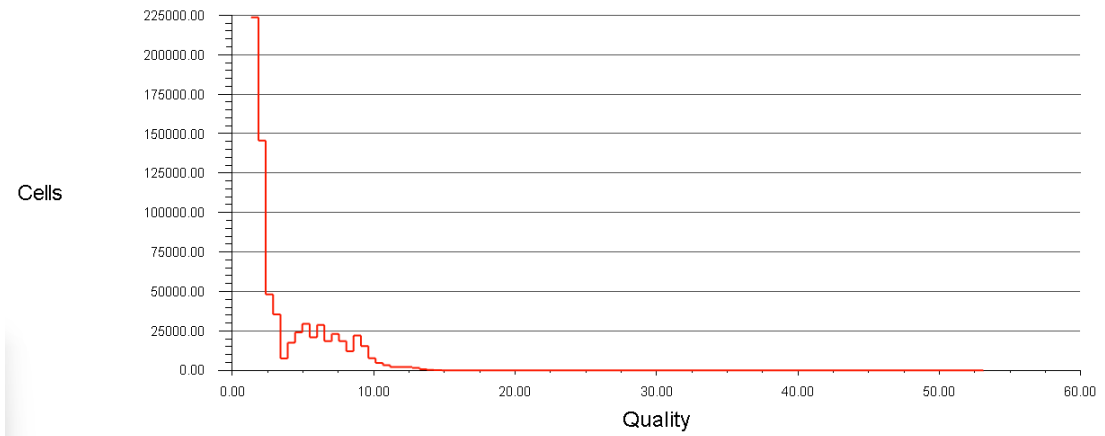
Figure 3.13 Aspect Ratio (Reverse Operation)
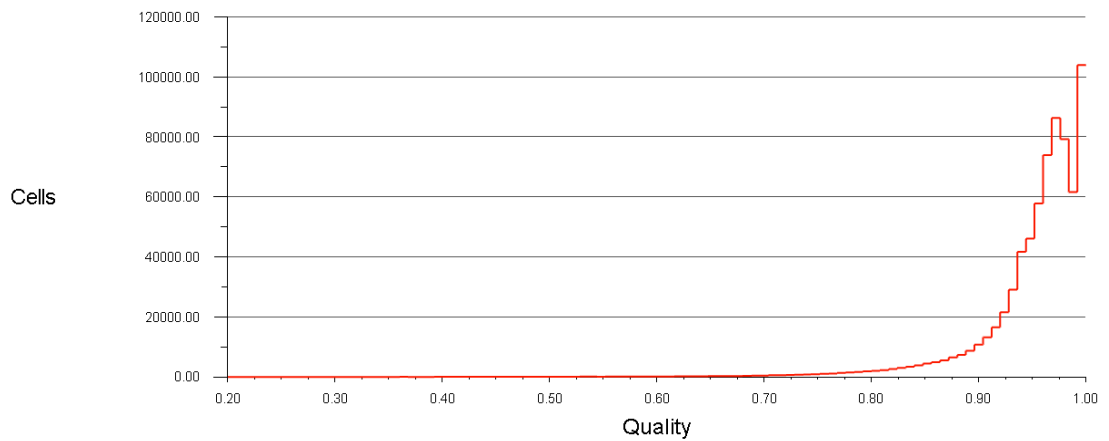
Figure 3.14 Orthogonal Quality (Reverse Operation)
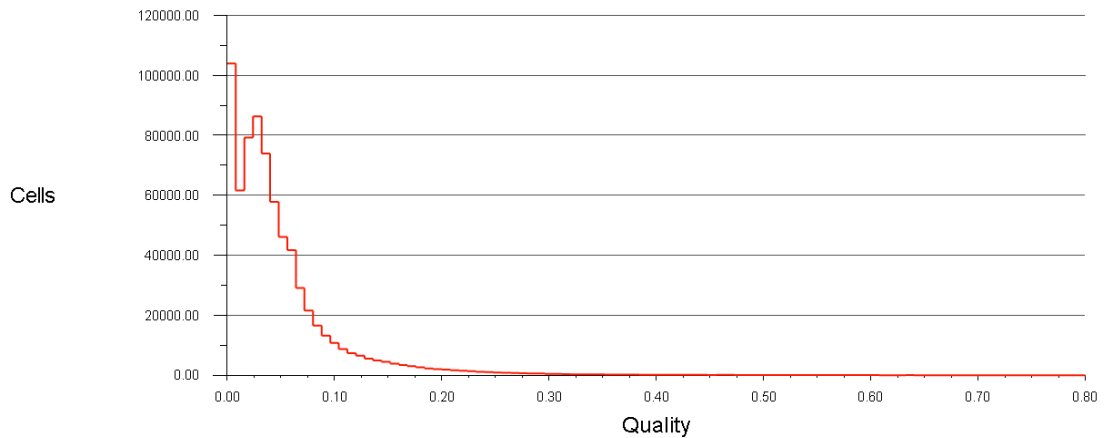
Figure 3.15 Skewness (Reverse Operation)

3.5. Cavitation Models

The cavitation model used were Schnerr-Sauer and Singhal model. Both of the cavitation models are mixture model of Euler-Euler multiphase model. However, the Schnerr-Sauer and Singhal cavitation models are two different approaches for modeling the formation and collapse of cavitation bubbles in fluid dynamics, and they differ in several ways. The Schnerr-Sauer model uses a Rayleigh-Plesset-type equation, assumes a single collapse phase, has a fixed boundary condition, and requires a complex numerical algorithm. In contrast, the Singhal model uses a homogeneous equilibrium model, takes into account multiple collapse phases, allows for mass transfer, can be implemented using a simpler numerical scheme, and is applicable for a wider range of flow speeds.

Table 5 Solver Settings (Non-Cavitating)

Pressure-Velocity Coupling	PISO
Pressure Discretization	PRESTO!
Turbulence Model	SST k- ω
Solver Type	Transient (Sliding Mesh)
Time Step Size	Equivalent to one degree rotation
Material	Water Liquid
Turbulence Parameters Discretization	Second Order Upwind
Momentum Equations Discretization	Second Order Upwind

ANSYS user manual suggested the use of PRESTO! pressure discretization scheme for multiphase flows and flows involving curved surfaces and rotating machines. It also highly recommends the use of PISO algorithm for pressure-velocity compounding The K- ω SST turbulence model was used for the simulation which is a popular choice among researchers along with k- ε with wide uses for simulating flows involving marine propellers (Guilherme Vaz et al., 2015). Guilherme Vaz et al. (2015) suggested the use of sliding grid/interface approach for unsteady simulations of marine propellers in an earth fixed reference frame. This is also supported by Takayuki WATANABE et al. (2003). A timestep equivalent to a single degree of rotation was used for the transient simulation as suggested by Chaosheng Zheng et al. (2019).

Table 6 Solver Settings (Cavitating)

Pressure-Velocity Coupling	PISO
Pressure Discretization	PRESTO!
Turbulence Model	SST k- ω
Solver Type	Transient (Sliding Mesh)
Time Step Size	Equivalent to one degree rotation
Phases	1. Water Liquid 2. Water Vapor
Vaporization Pressure	2337 Pa
Multiphase model	Implicit mixture
Cavitation Models	1. Schnerr-Sauer model 2. Singhal model
Volume Fraction Discretization	First Order Upwind
Turbulence Parameters Discretization	First Order Upwind
Momentum Equations Discretization	First Order Upwind

The Schnerr-Sauer Cavitation Model is a tool used in CFD to predict the occurrence of cavitation in fluid systems, which is the formation of vapor bubbles in a liquid that can cause damage and decrease efficiency. This model assumes the fluid as a mixture of liquid and vapor phases and uses an equation to track the growth of cavitation bubbles in the flow. It also accounts for turbulence effects and predicts the behavior of the cavitation bubbles using a bubble dynamics equation. The model has been applied in various engineering fields and is useful in predicting cavitation.

The Schnerr-Sauer model makes use of an equation that describes the dynamics of bubbles in order to anticipate how they will behave and how big they will become. This equation takes into account various factors such as pressure changes, energy and mass transfer between liquid and vapor phases, and bubble growth and collapse. In addition, the model provides an equation for vapor phase pressure, which is utilized to determine whether the fluid is experiencing cavitation or not.

This model for cavitation is called the "full cavitation model" and was developed by Singhal et al. (2002). It considers all major effects, such as change in phase, bubble behavior, fluctuations in pressure, and non-condensable gases. It is capable of dealing with multiphase flows and the transport of various species within them. The model also accounts for slip velocities between liquid and gaseous phases, as well as the thermal and compressibility effects of both phases. The model can be applied with the mixture multiphase model, with or without slip velocities, although using the model without slip velocity is preferred unless the situation warrants their inclusion.

Mohamed M. Helal et al. (2011) used the Singhal cavitation model in INSEAN E977A propeller using a transition sensitive turbulence model and verified it against an experimental results Watanabe et al. (2003) also used the Singhal cavitation model to simulate the cavitating flow around two different propellers and validate against EFD. (Experimental Fluid Dynamics) results. In literature, the use of Singhal cavitation model is significant to validate the CFD result with EFD result.

Before including effects of cavitation, numerical simulation was conducted using sliding mesh method only using the turbulence model. When semi-stable flow field was obtained, the cavitation model was activated as suggested by Chaosheng Zheng et al. (2019).

For Schnerr-Sauer cavitation model, bubble number density was chosen to be 10e+13 according to study by Zhu Jiakai at al. (2015). For Singhal Cavitation model, the recommended value of 1.5e-05 according to Ansys Fluent Users Guide (2022) was chosen. Surface Tension Coefficient of 72.75e-3 was taken for water at 20 degree Celsius according to Vargafik et al., (1983).

3.6. Boundary Conditions

Boundary conditions are calculated for certain values of advance ratio (J) and cavitation number (σ). Other performance parameters include the thrust coefficient KT, the torque coefficient KQ and the efficiency η.

The advanced ratio (J) and cavitation number (σ) were non-dimensionalized with the data available for INSEAN E799A propeller from Mohamed M. Helal et al. (2011).

Table 7 Boundary Conditions

Propeller Speed (rps)	Propeller Speed (rpm)	Advanced Ratio (J)	Inlet velocity(m/s)	Cavitation Number	Abs. Pressure (Pa)
25	1500	0.9	6.3579	4.455	113301.17
30	1800	0.83	7.0361	2.063	76331.05
40	2400	0.77	8.7033	1.783	116028.03
50	3000	0.71	10.0314	1.763	177986.68

CHAPTER FOUR: RESULT AND DISCUSSIONS

The propeller's performance is usually measured using non-dimensional coefficients, such as thrust coefficient (K_T), torque coefficient (K_Q), and efficiency, as well as their variations with advance coefficients (J). Using Fluent 2022 R1 software, a comprehensive computational analysis of the flow was performed, and using the software the propeller's thrust and torque was calculated for various rotational speeds (rps) and expressed them in terms of K_T and K_Q. The thrust and torque estimates obtained for non-cavitating flow are presented in the following table below.

Table 8 Computational estimation of thrust and torque

N (rps)	50	40	30	25
Advanced ratio (J)	0.71	0.77	0.83	0.9
Kt	0.122381	0.095355	0.068111	0.036228
10Kq	0.259246	0.215079	0.172174	0.121319
efficiency	0.533432	0.54332	0.522572	0.427737

Comparing the two performance parameters from literature and computed results, it is found that both computed torque and thrust coefficients variation with advance ratio follows the same nature of variation as followed in the literature.

The result indicates that as the advance ratio increases, both the thrust coefficient (K_T) and torque coefficient (K_Q) of the propeller decrease. Additionally, the propeller efficiency exhibits a consistent pattern of initially increasing non-linearly to a peak optimal value, followed by a sharp decline as the advance ratio (J) value increases. This result is supported by the study done by Yeo et al. (2014).
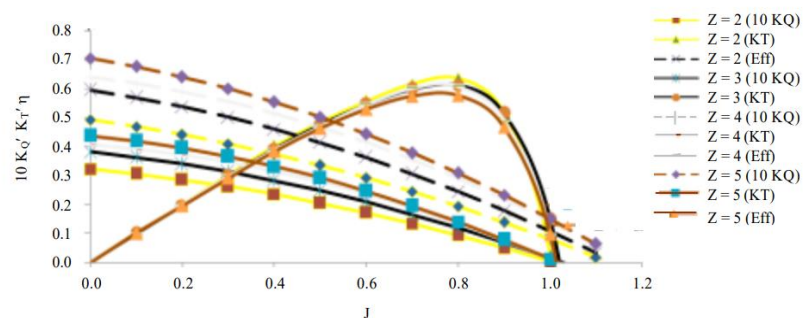
Figure 4.1 Variation of performance parameters with advance ratio from literature
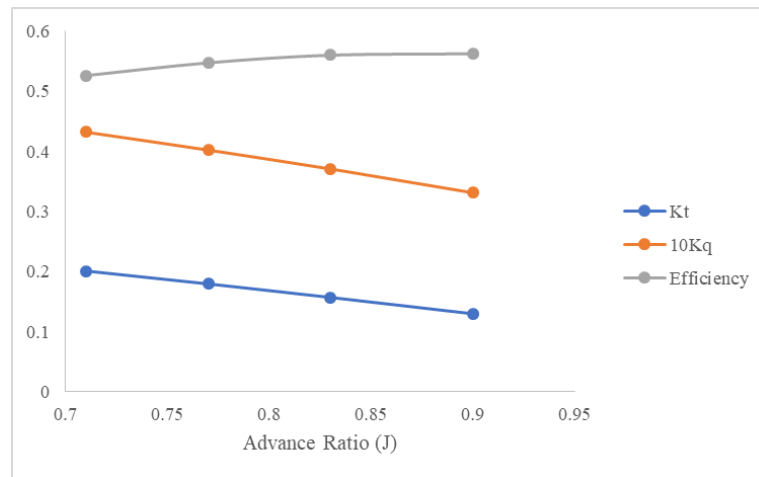
Figure 4.2 Computational Variation of Performance Parameters with Advance Ratio for Non-Cavitating flow in Forward Operation
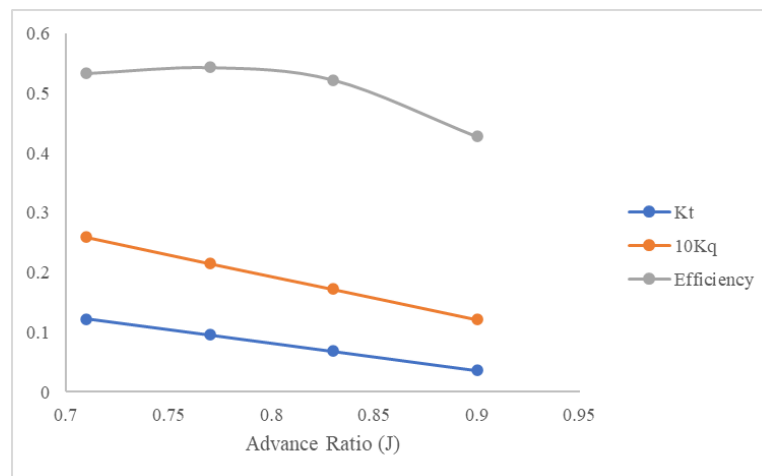
Figure 4.3 Computational Variation of Performance Parameters with Advance Ratio for Non-Cavitating flow in Reverse Operation

4.1. Propeller under Cavitation

Table below presents the comparison of volume fraction of vapor in motorboat propeller for four different values of advance ratio (J). It is evident from the results that as the advance ratio decreases the cavitation area increases starting from the leading edge and advancing towards the suction side of the propeller blade. For J = 0.9, the cavitation number is fairly high (4.455). The cavitation in this condition is marginal. On the other hand, for J = 0.71, the cavitation number is relatively low (1.763). As the local pressure drop is more in this case, the cavitation area is covering almost half the suction side of the propeller blade. Both the cavitation model showed similar pattern of cavitation

For Forward Operation,
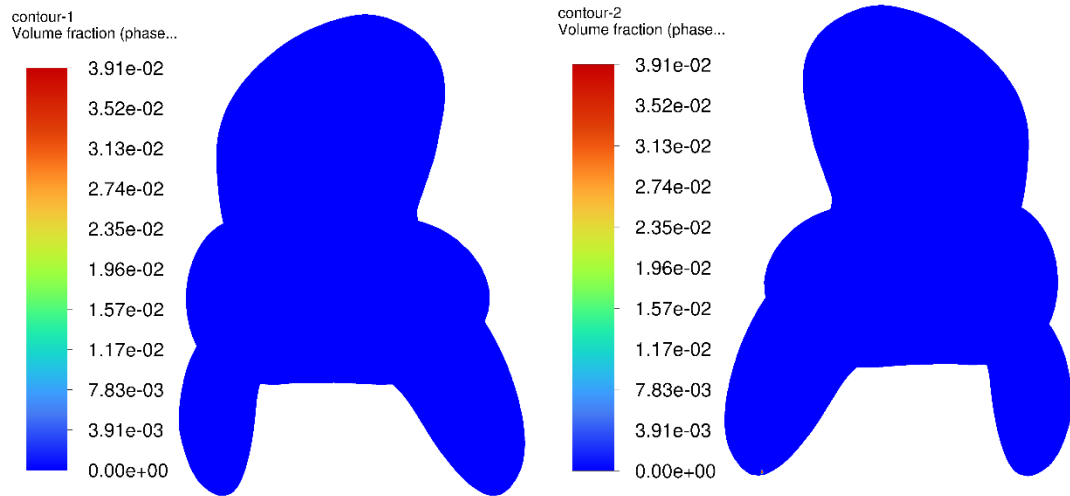
Figure 4.4 Contours of Volume Fraction of Vapor for Schnerr-Sauer Model at J=0.9 on Suction Side (left) and Pressure Side (right)
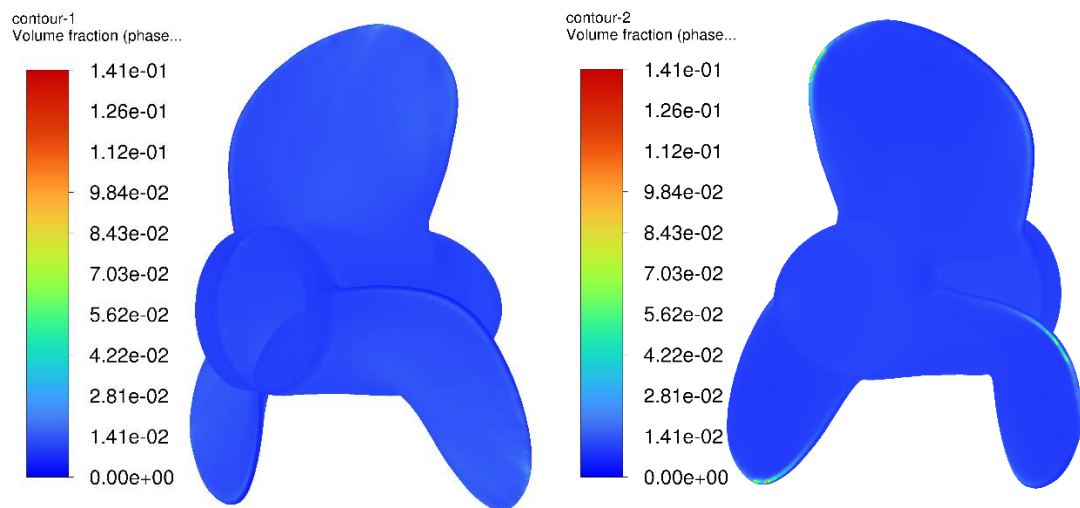
Figure 4.5 Contours of Volume Fraction of Vapor for Singhal Model at J=0.9 on Suction Side (left) and Pressure Side (right)
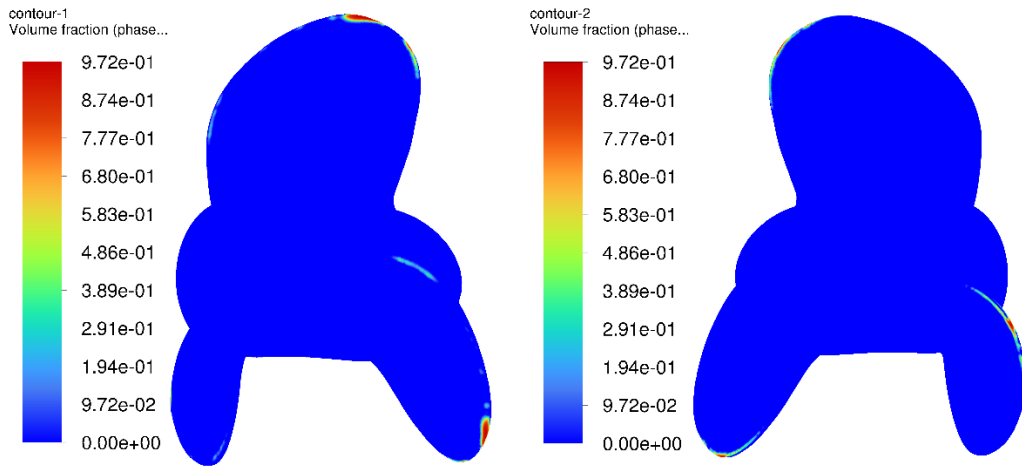
Figure 4.6 Contours of Volume Fraction of Vapor for Schnerr-Sauer Model at J=0.83 on Suction Side (left) and Pressure Side (right)
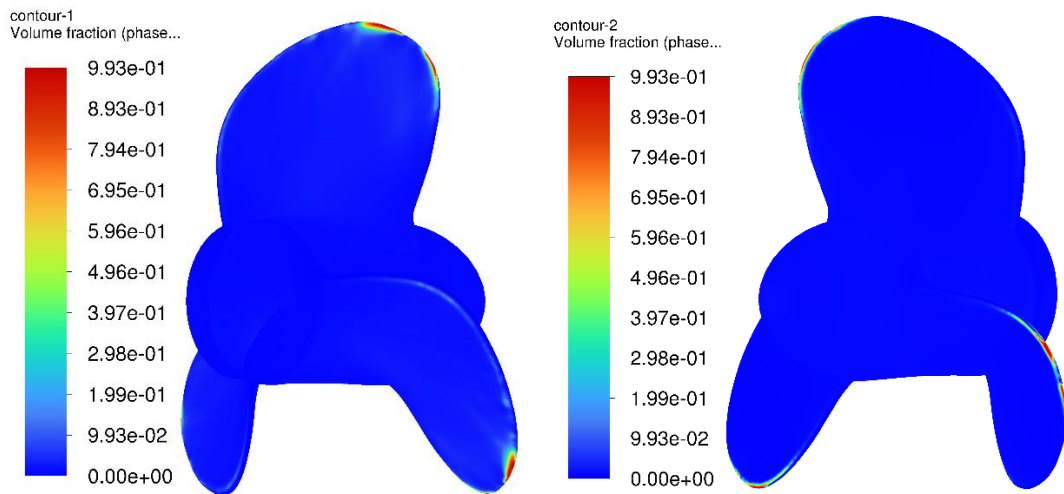
Figure 4.7 Contours of Volume Fraction of Vapor for Singhal Model at J=0.83 on Suction Side (left) and Pressure Side (right)
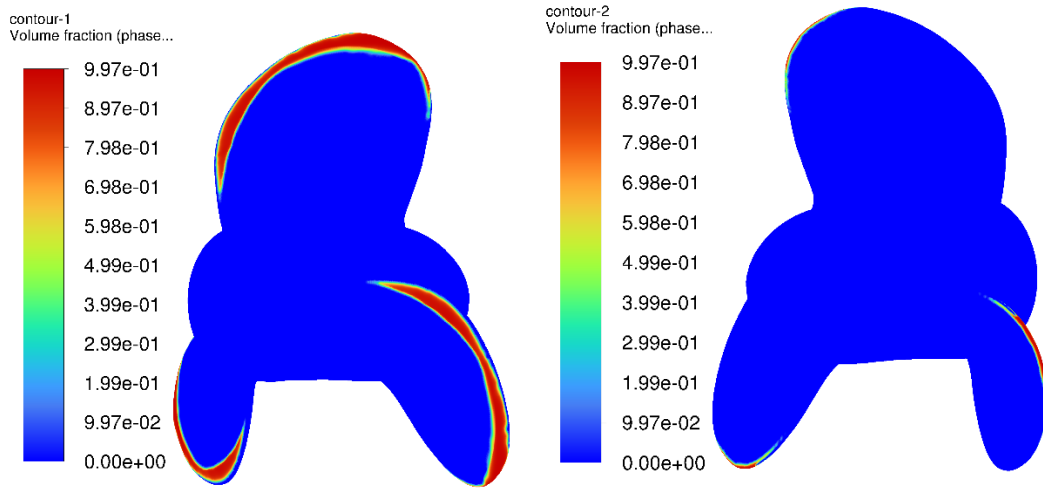
Figure 4.8 Contours of Volume Fraction of Vapor for Schnerr-Sauer Model at J=0.77 on Suction Side (left) and Pressure Side (right)
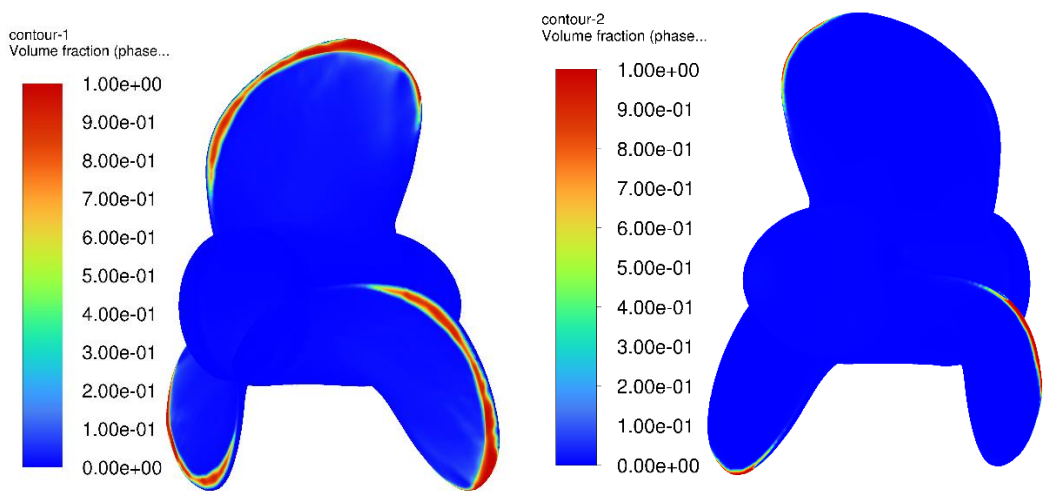
Figure 4.9 Contours of Volume Fraction of Vapor for Singhal Model at J=0.77 on Suction Side (left) and Pressure Side (right)
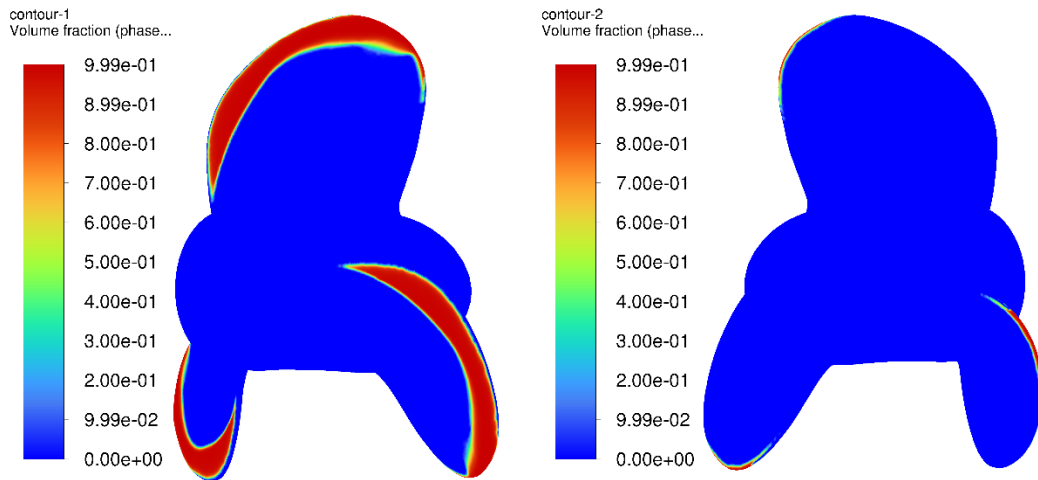
Figure 4.10 Contours of Volume Fraction of Vapor for Schnerr-Sauer Model at J=0.71 on Suction Side (left) and Pressure Side (right)
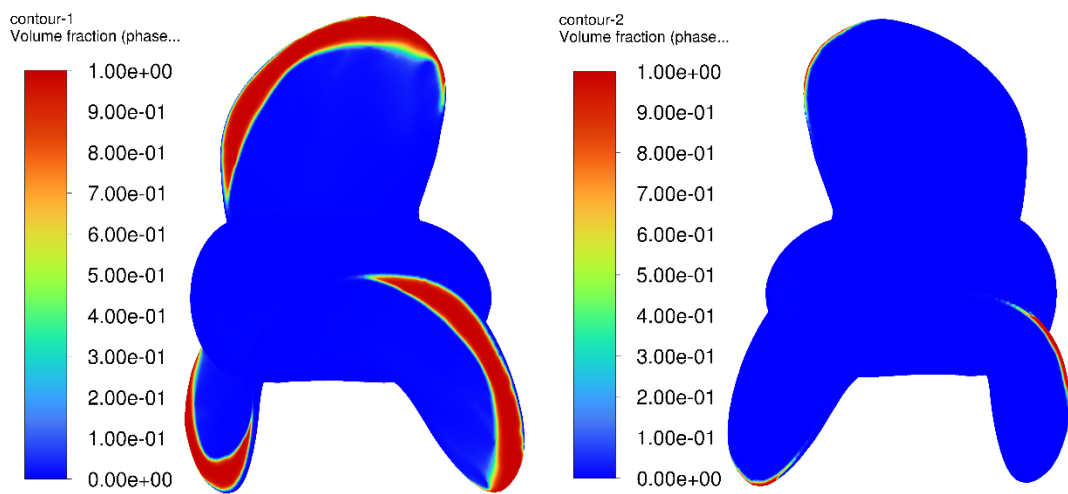
Figure 4.11 Contours of Volume Fraction of Vapor for Singhal Model at J=0.71 on Suction Side (left) and Pressure Side (right)
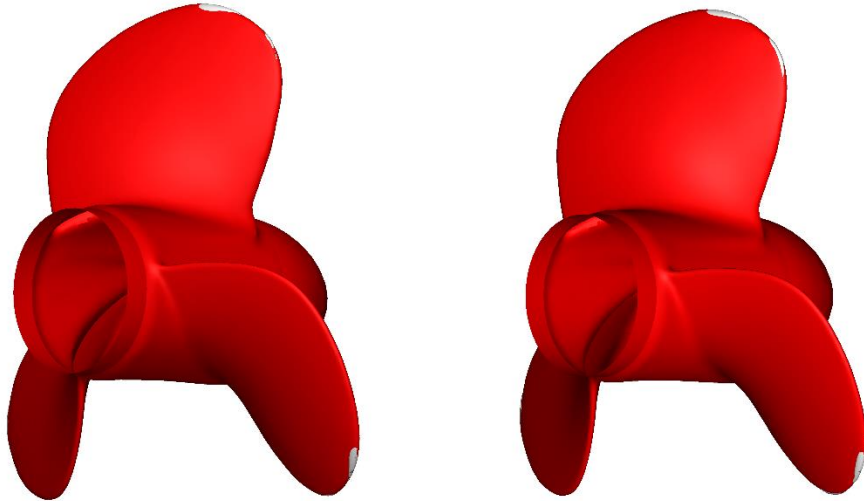
Figure 4.12 Iso-surface of Volume fraction α=0.5 for Schnerr-Sauer (left) and Singhal (right) cavitation models (J=0.83) in Forward Operation
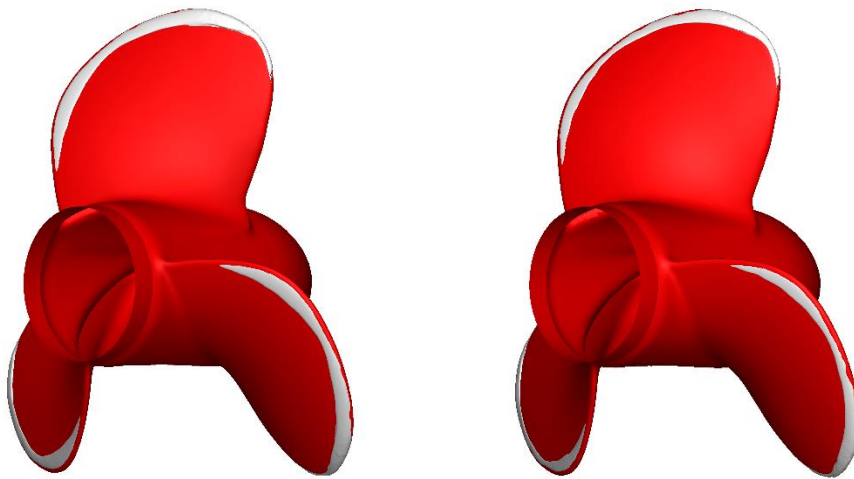
Figure 4.13 Iso-surface of Volume fraction α=0.5 for Schnerr-Sauer (left) and Singhal (right) cavitation models (J=0.77) FOR Forward Operation
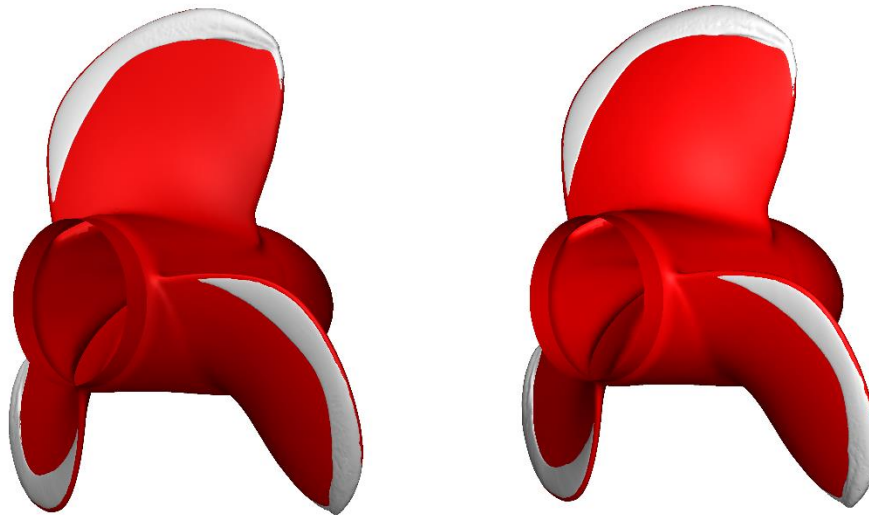
Figure 4.14 Iso-surface of Volume fraction α=0.5 for Schnerr-Sauer (left) and Singhal (right) cavitation models (J=0.71) for Forward Operation

In the case of J=0.9 (σ=4.455) no cavitation is observed. The maximum vapor volume fraction was observed to be 0.0391 and 0.141 for Schnerr-Sauer and Singhal cavitation models respectively. As cavitation number decreases, increase in area of vaporized region can be observed. At J=0.83, bubbles start forming near the tip of the propeller. Small traces of vapor formation can also be seen at leading and trailing edges from the contours of volume fraction of vapor. As the cavitation number keeps decreasing, the cavitation starts extending along the top edges of suction side of the propeller, which then keeps increasing in area at the suction side of the propeller.

The variation of thrust and torque obtained by simulation at various rotational speeds during forward operation are shown below:

Table 9 Performance Parameters for J=0.9 (Forward Operation)

N (rps)	25		
Model	Non Cavitating	Schnerr-Sauer model	Singhal model
Thrust (N)	517.5134	517.4779	498.8357
Kt	0.130104	0.130095	0.125408
Torque (Nm)	37.23482	37.23466	36.40232
$10K_Q$	0.331271	0.331269	0.323864
Efficiency	0.56256	0.56252	0.55466

Table 10 Performance Parameters for J=0.83 (Forward Operation)

N (rps)	30		
Model	Non Cavitating	Schnerr-Sauer model	Singhal model
Thrust (N)	900.5346	950.8412	917.881
Kt	0.157219	0.166002	0.160248
Torque (Nm)	60.01629	63.00259	61.96901
$10K_Q$	0.370801	0.389251	0.382865
Efficiency	0.560097	0.563354	0.552896

Table 11 Performance Parameters for J=0.77 (Forward Operation)

N (rps)	40		
Model	Non Cavitating	Schnerr-Sauer model	Singhal model
Thrust (N)	1830.205	1944.801	1910.145
Kt	0.179733	0.190987	0.187583
Torque (Nm)	115.7697	122.2333	121.4408
$10K_Q$	0.402336	0.424799	0.422045
Efficiency	0.547456	0.518507	0.521891

Table 12 Performance Parameters for J=0.71 (Forward Operation)

N (rps)	50		
Model	Non Cavitating	Schnerr-Sauer model	Singhal model
Thrust (N)	3201.431	3392.734	3364.294
Kt	0.201211	0.213234	0.211447
Torque (Nm)	194.2704	205.3742	204.7993
$10K_Q$	0.432096	0.456793	0.455515
Efficiency	0.526199	0.527492	0.524539
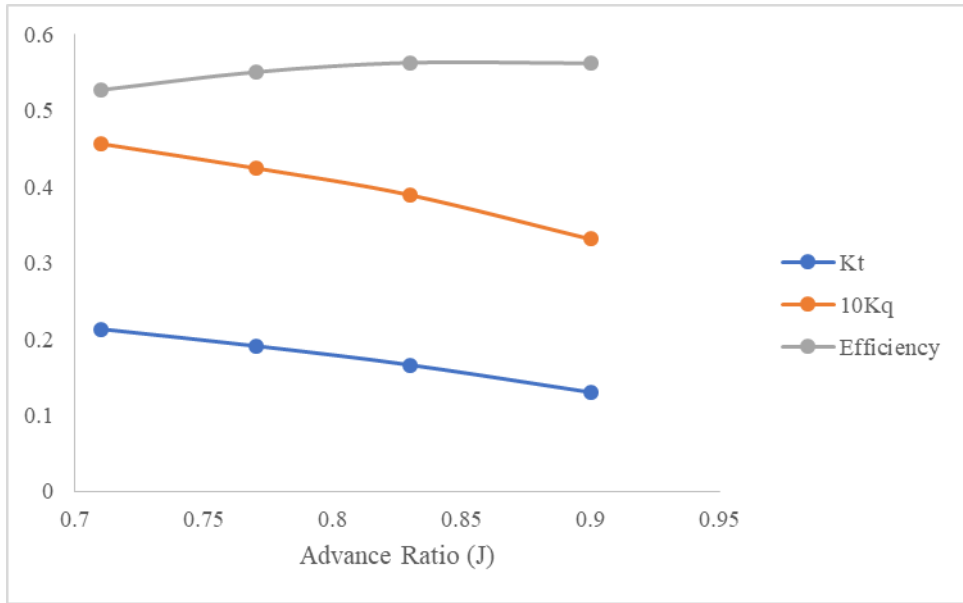
Figure 4.15 Performance parameters variation with Advance ratio (Schnerr-Sauer model in Forward Operation)
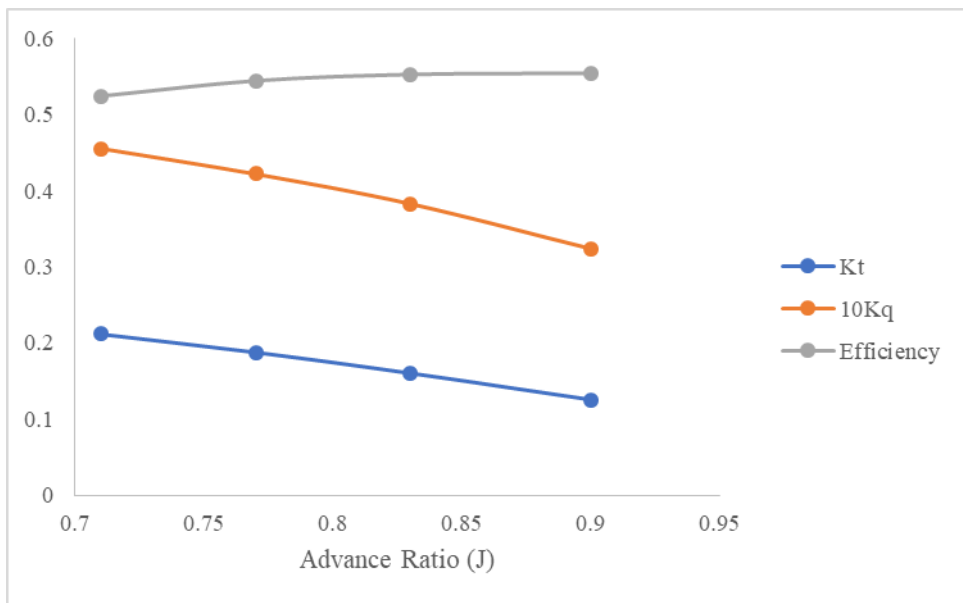
Figure 4.16 Performance parameters variation with Advance ratio (Singhal model in Forward Operation)
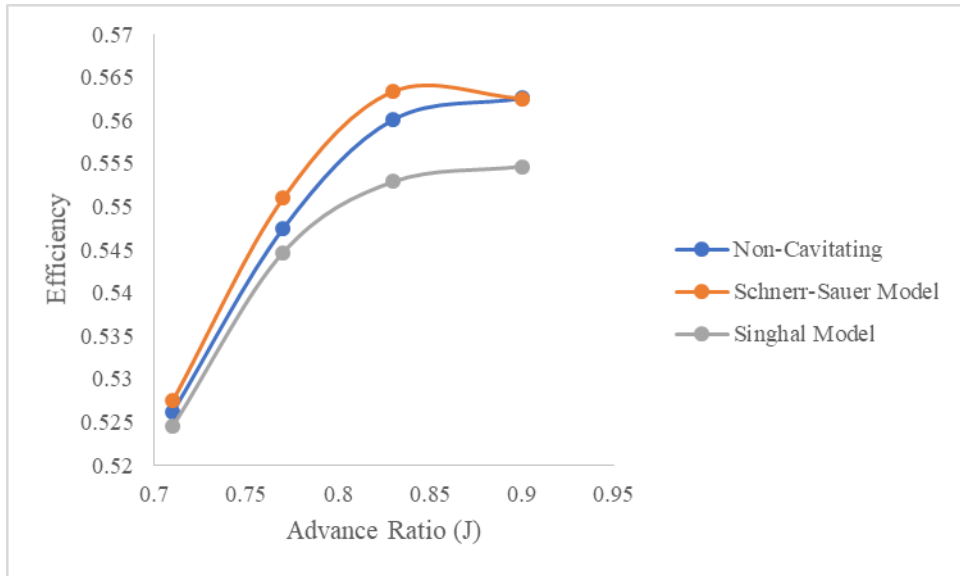
Figure 4.17 Variation of Efficiency with Advance Ratio in Forward Operation

In case of Forward operation, which refers to the forward advance of the motorboat, the performance parameters such as thrust coefficient (K_T), torque coefficient (K_Q) are observed to be higher in cavitating condition compared to non-cavitating condition. The efficiency computed by Schnerr-Sauer cavitation model is observed to be higher than both the Singhal cavitation model and non-cavitating model. Here the Singhal cavitation model appears to be in agreement with the literature while Schnerr-Sauer cavitation model appears to be in disagreement.

For forward operation of the motorboat propeller, the thrust coefficient (K_T) and torque coefficient (K_Q) both are increasing slightly with decreasing advance ratio (J) while the efficiency is observed to be decreasing with small slope with advance ratio (J). It is also noticed from the fig 4.16 that the efficiency variation with advance ratio (J) for forward operation is around 4-5% only.

For Reverse Operation,

Table 13 Contours of Volume Fraction of Vapor

J	Schnerr-Sauer Cavitation Model	Singhal et al. Cavitation Model
0.9		
0.83		
0.77		

| 0.71 | |
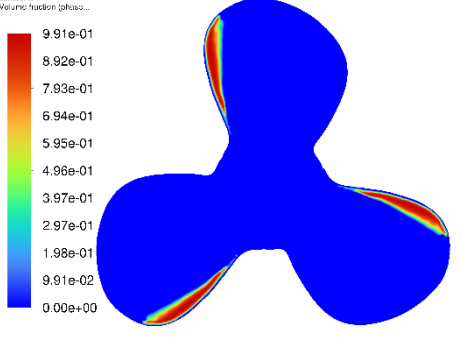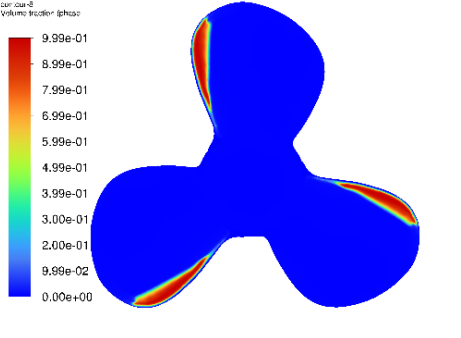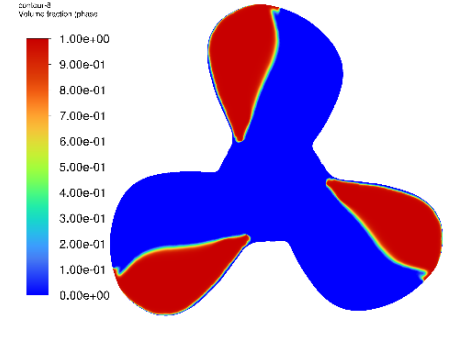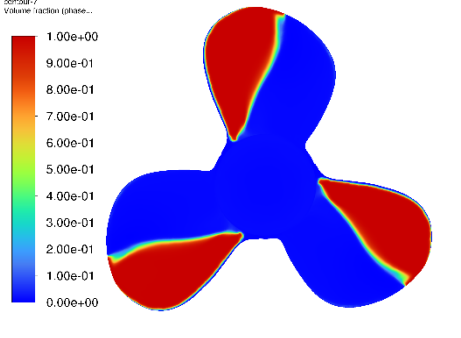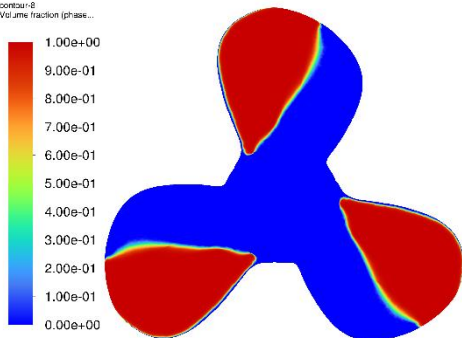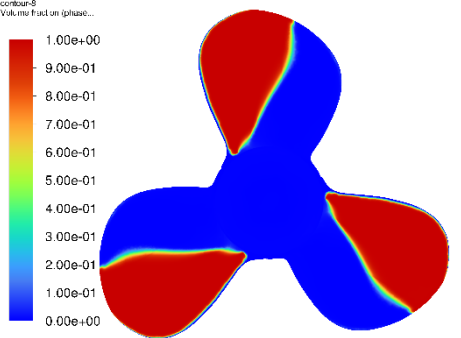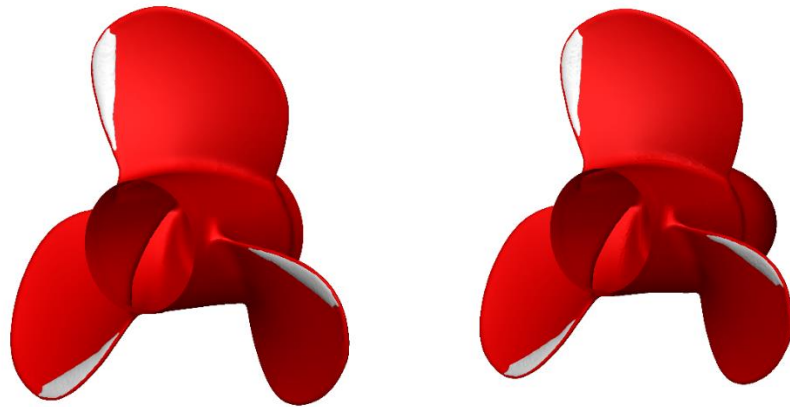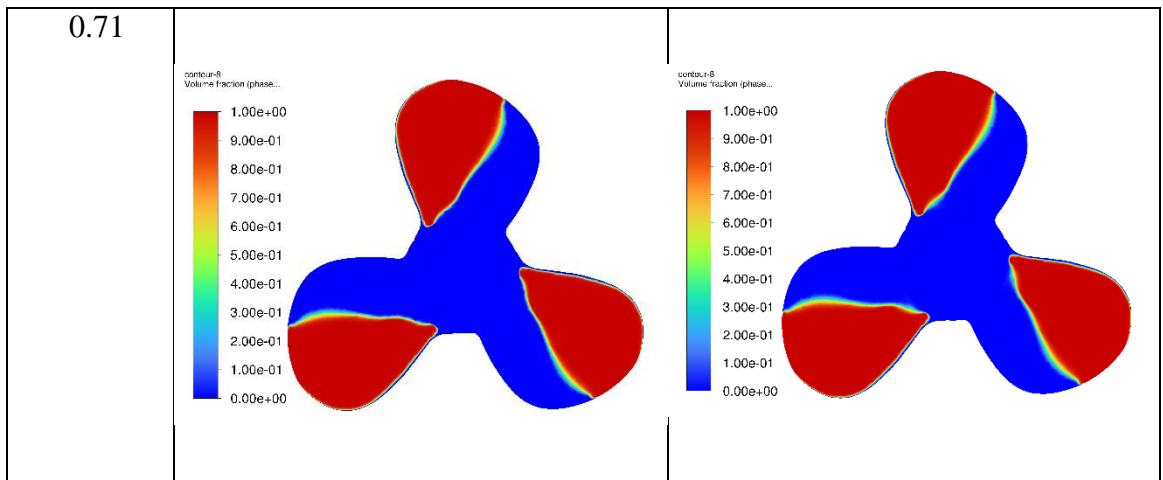
Figure 4.18 Iso-surface of Volume fraction α=0.5 for Schnerr-Sauer (left) and Singhal (right) cavitation models (J=0.9) for Reverse Operation
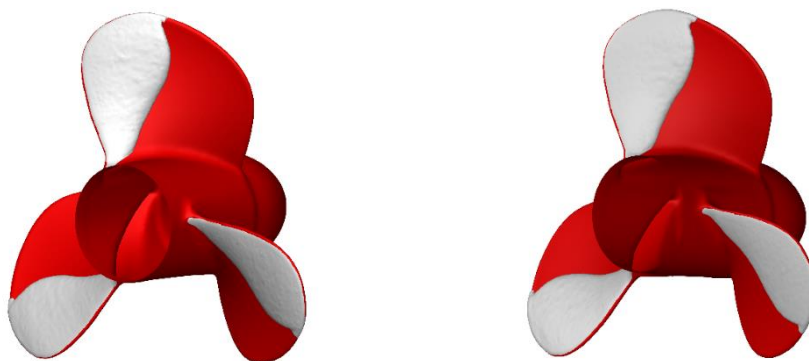
Figure 4.19 Iso-surface of Volume fraction α=0.5 for Schnerr-Sauer (left) and Singhal (right) cavitation models (J=0.83) for Reverse Operation
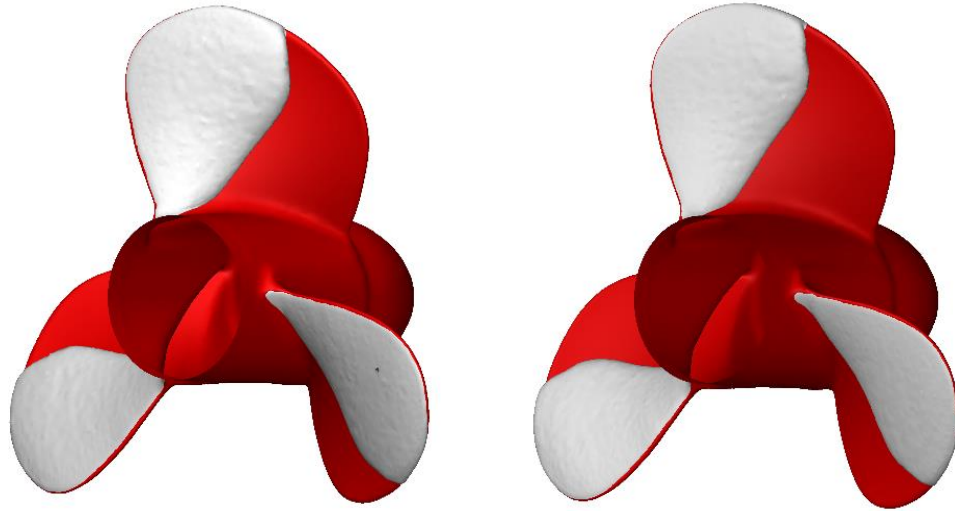
Figure 4.20 Iso-surface of Volume fraction α=0.5 for Schnerr-Sauer (left) and Singhal (right) cavitation models (J=0.77) for Reverse Operation
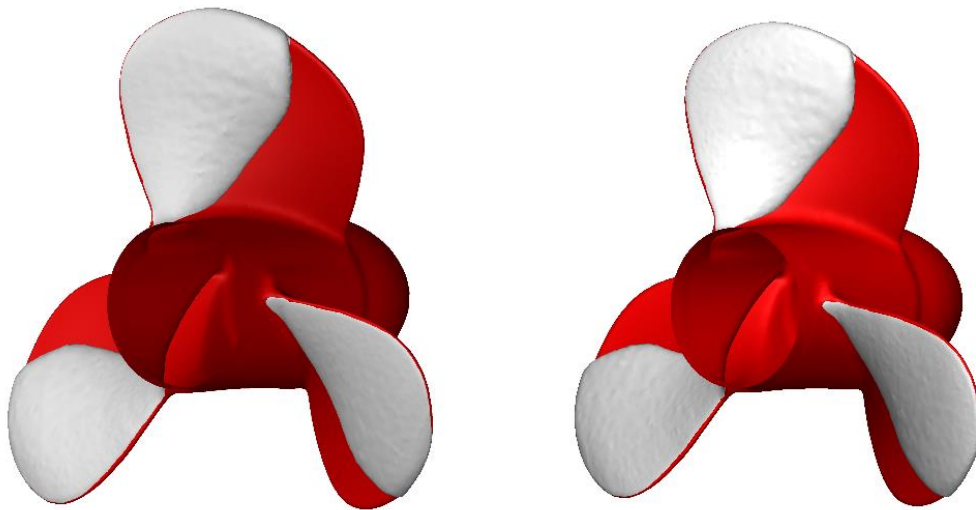
Figure 4.21 Iso-surface of Volume fraction α=0.5 for Schnerr-Sauer (left) and Singhal (right) cavitation models (J=0.71) for Reverse Operation

Result shows that as the cavitation number decreases from σ=4.455 to σ=2.063, the propeller becomes more prone to cavitation. Area of volume fraction of vapour is observed to be slightly higher in Singhal cavitation model compared to Schnerr-Sauer model in all four cases.

Tables below presents the thrust and torque variations at various rotational speeds of the propeller obtained by numerical simulations.

Table 14 Performance Parameters for J= 0.9 (Reverse Operation)

N (rps)	25		
Model	Non Cavitating	Schnerr-Sauer model	Singhal model
Thrust (N)	144.1036	105.7121	89.73274
Kt	0.036228	0.026576	0.022559
Torque (Nm)	13.63624	19.44101	18.68955
$10K_Q$	0.121319	0.172963	0.166277
Efficiency	0.427737	0.220091	0.194334

Table 15 Performance Parameters for J= 0.83 (Reverse Operation)

N (rps)	30		
Model	Non-Cavitating	Schnerr-Sauer model	Singhal model
Thrust (N)	390.131	364.1422	340.0992
K_T	0.068111	0.063573	0.059376
Torque (Nm)	27.86738	39.07978	37.94798
$10K_Q$	0.172174	0.241448	0.234455
Efficiency	0.522572	0.347817	0.334541

Table 16 Performance Parameters for J=0.77 (Reverse Operation)

N (rps)	40		
Model	Non Cavitating	Schnerr-Sauer model	Singhal model
Thrust (N)	970.9903	955.8386	918.9254
K_T	0.095355	0.093867	0.090242
Torque (Nm)	61.88766	83.90832	81.27572
$10K_Q$	0.215079	0.291608	0.282458
Efficiency	0.54332	0.394479	0.391529

Table 17 Performance Parameters for J=0.71 (Reverse Operation)

N (rps)	50		
Model	Non Cavitating	Schnerr-Sauer model	Singhal model
Thrust (N)	1947.174	1872.202	1819.49
K_T	0.122381	0.117669	0.114356
Torque (Nm)	116.5568	150.7182	148.2916
$10K_Q$	0.259246	0.335227	0.32983
Efficiency	0.533432	0.396642	0.391783

Compared to non-cavitating model, both the cavitating models show decrease in performance parameters. Singhal cavitation model appears to cause more performance impact, as shown by higher volume fraction in contours above. Besides the performance values, the pattern and area of cavitation region appears to be similar for both models. The interface between water and vapor is more dispersed in Singhal cavitation model.
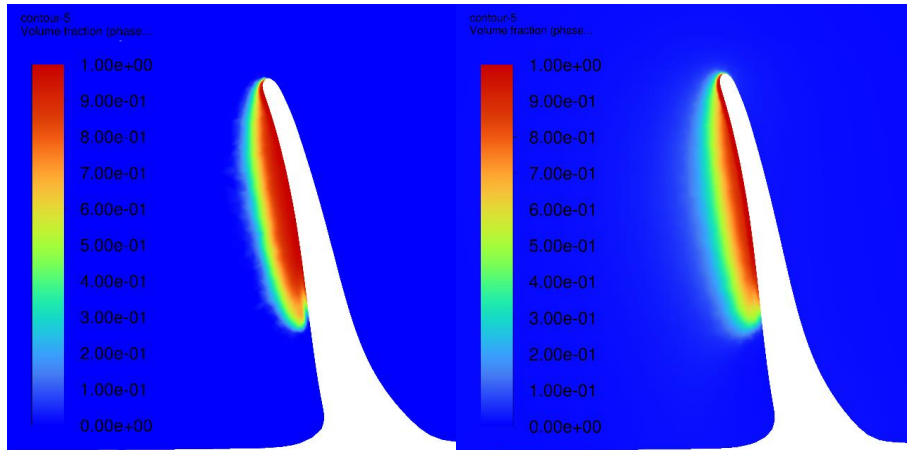
Figure 4.22 Contours of volume fraction in YZ plane for 30rps (left: Schnerr-Sauer model, right: Singhal model)
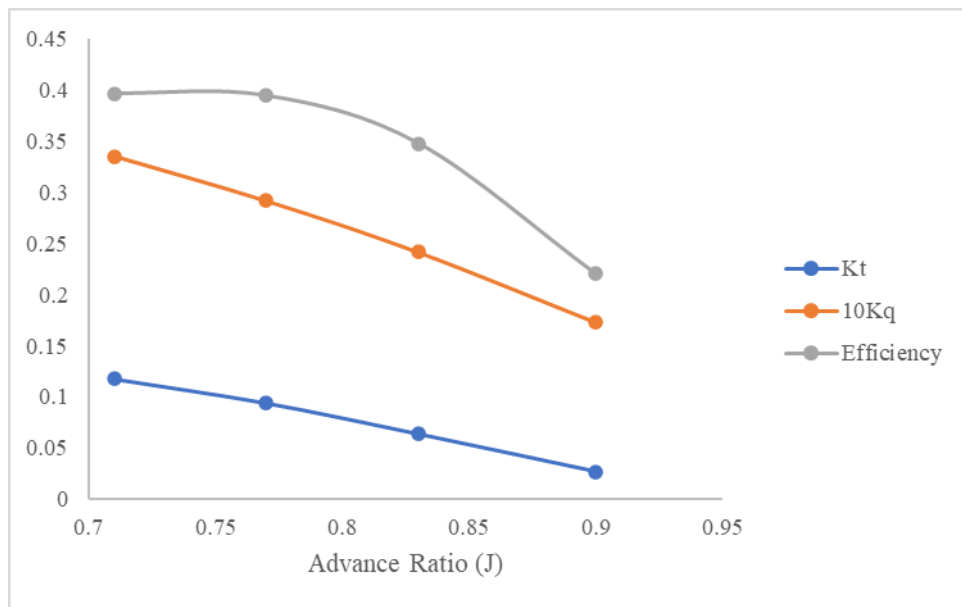
Figure 4.23 Performance parameters variation with Advance ratio (Schnerr-Sauer model in Reverse Operation)
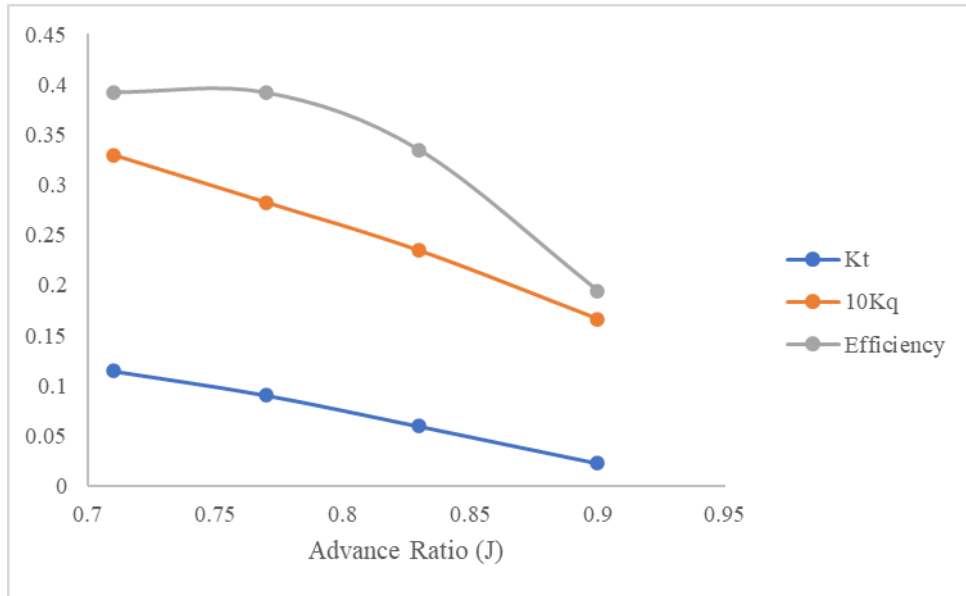
Figure 4.24 Performance parameters variation with Advance ratio (Singhal model in Reverse Operation)

Figure 4.23 and Figure 4.24 shows two cavitation models shows very little variation in predicting the performance parameters of the propeller. For all values of advance ratio, the Singhal cavitation model has predicted slightly higher values of performance parameters compared to Schnerr-Sauer cavitation model.
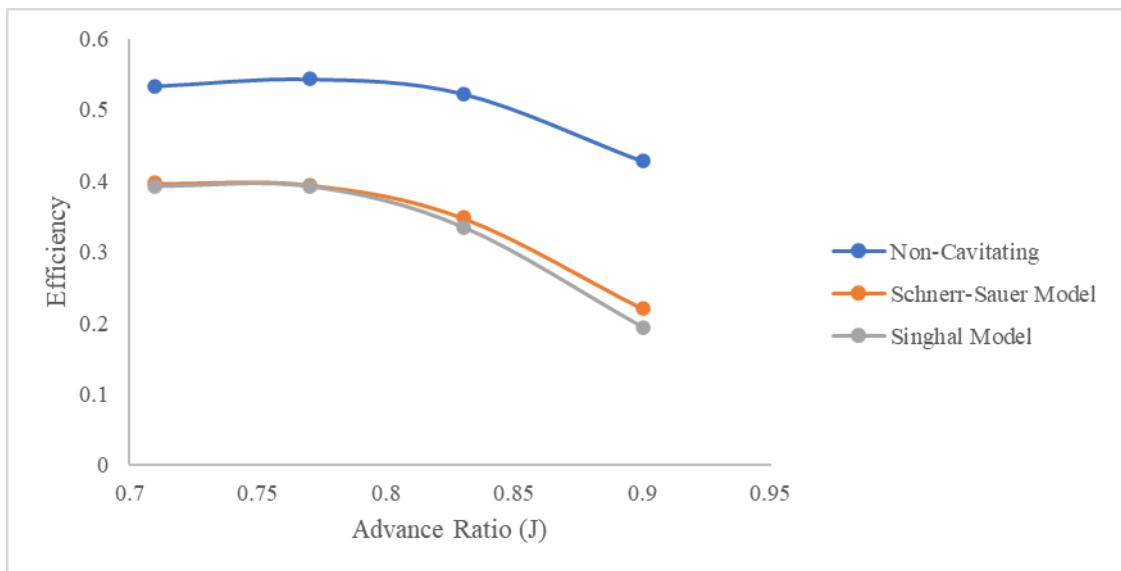
Figure 4.25 Variation of Efficiency with Advance Ratio in Reverse Operation

Result above shows that there is a significant drop in efficiency of propeller in cavitating flow compared to non-cavitating flow. As cavitation occurs, an increase in coefficient of torque is also observed. As the pressure in the propeller drops below vapor pressure, cavitation starts to take place. Cavitation causes pressure fluctuations and turbulence in water. A high-pressure jet is induced as cavitation bubbles collapse which impinge on the propeller blades causing vibrations and noise. This turbulent vibration and noise cause losses and reduce the propeller's efficiency. The reductions in efficiency are more significant at higher advance ratios. Compared to non-cavitating flow, the point of maximum efficiency is shifted towards lower values of advance ratio.

CHAPTER FIVE: CONCLUSION AND RECOMMENDATIONS

A detailed and complete CFD procedure for simulating the three-dimensional cavitating flow of a motorboat propeller is presented in this report. Along with that the cavitation patterns, performance characteristics is compared using two different cavitation models. This methodology only focuses on the possibility of turbulent flow regimes over the propeller. For turbulence modeling, k-ω SST is used. The CAD model used for this investigation is a three-blade motorboat propeller designed for Parsun outboard motors. The numerical simulation was carried out in FLUENT 2022 R1 version using a transient sliding mesh approach.

For the better comparison of cavitation area between two cavitation models at various operating conditions, vapor volume fraction iso-surface is also generated which is a preferred way of comparing cavitation pattern in literature.

In the case of reverse operation, the cavitation models are in good agreement in predicting the cavitation pattern for all four advance ratios. However, the Singhal cavitation model produced relatively low performance parameter values than the Schnerr-Sauer cavitation model. Schnerr-Sauer model does not take the effect of any non-condensable gas by default. To improve the accuracy of the cavitation models, the model constants can be adjusted to better match the properties of water.

In the case of forward operation, the cavitation models are in agreement in predicting the cavitation pattern but larger variations were observed while computing the performance parameters. A peculiar result was obtained where the propeller generated more thrust during cavitation than in non-cavitating case. Comparing the efficiencies, the Schnerr Sauer model shows efficiency even higher than simulation with no cavitation.

Recommendations:

- Study the effect of propeller pitch on the cavitation and performance parameters
- Causes of the peculiar computational results in case of forward operation of propeller
- Experimental validation of Schnerr-Sauer cavitation model
- study the effect of propeller geometrical parameters on cavitation

REFERENCES

1. ANSYS Fluent Theory Guide (2022)

2. ANSYS Fluent User's Guide (2022)

3. Brandner, P. A., Lecoffre, Y., & Walker, G. a. H. (2007). Design Considerations in the Development of a Modern Cavitation Tunnel. *16th Australasian Fluid Mechanics Conference (AFMC)*, 630–637.

4. Bulten, N., Oprea, A.L., (2006). Evaluation of McCormick's rule propeller tip cavitation inception based on CFD results. In: 6th Int. Symp. On Cavitation CAV2006, Wageningen, September.

5. C. M. O. Kiam Beng Yeo, Rosalam Sabatly and W. Y. Hau, "Effects of Marine Propeller Performance and Parameters Using CFD Method," J. Appl. Sci., vol. 22, 2014

6. Carlton, J. (2019). *Marine propellers and propulsion* (4th ed.). Butterworth-Heinemann.

7. D. Boucetta and O. Imine, "Numerical Simulation of the Flow around Marine Propeller Series," J. Phys. Sci. Appl., vol. 6, no. 3, pp. 55-61, 2016

8. D. Ponkratov and A. Caldas. Prediction of cavitation erosion by detached eddy simulation (des) and its validation against model and ship scale results. In 4th International Symposium on Marine Propulsors, Austin, Texas, USA, 2015.

9. Gaggero, S., & Villa, D. (2018). Cavitating Propeller Performance in Inclined Shaft Conditions with OpenFOAM: PPTC 2015 Test Case. Journal of Marine Science and Application, 17(1), 1–20. https://doi.org/10.1007/s11804-018-0008-6

10. Gatete, E., Ndiritu, H., & Kiplimo, R. (2018). A Review on Marine Propeller Performance of High Speed Boat Running on an Outboard Engine. Proceedings of Sustainable Research and Innovation Conference, 213–220.

11. Gou, W., Wu, J., Zhang, H., & Lian, J. (2018). Simulation modeling of the combined damage caused by cavitation and abrasion in sediment-laden liquids. *Journal of Fluids Engineering*, *140*(11), 111302. https://doi.org/10.1115/1.4040066

12. Ibraheem, A. (2021b). Evaluating the Efficiency of Polyhedral Mesh Elements in Solving the Problem of the Flow around Ship's Rudder. International Journal of Engineering and Management Sciences, 6(2). https://ojs.lib.unideb.hu/IJEMS/article/view/9301

13. João Baltazar, D. R. (2021). Prediction of the Propeller Performance at Different Reynolds. *Journal of Marine Science and Engineering*.

14. K. Kimura, T. Kawamura, A. Fujii, T. Taketani, and Z. Huang. Study on unsteady cavitating flow simulation around marine propeller using a rans cfd code. In Proceedings of the 7th International Symposium on Cavitation, CAV2009, Ann Arbor, Michigan, USA, 2009.

15. Kalouptsidi, M. (2021, June 10). *The Role of Shipping in World Trade | Econofact*. Econofact | Key Facts and Incisive Analysis to the National Debate on Economic and Social Policies. https://econofact.org/the-role-of-shipping-in-world-trade

16. Kim, S., Du, W., Kinnas, S.A., 2017. Panel method for ducted propellers with sharp and round trailing edge duct with fully aligned wake on blade and duct. In: Smp'17 Conf, Espoo, Finland, June.

17. Li, D.-Q., Grekula, M., Lindell, P., 2009. A modified SST k-o turbulence model to predict the steady and unsteady sheet cavitation on 2D and 3D hydrofoils. In: Proc. 7th Int. Symp. on Cavitation (CAV 2009) Ann Arbor, MI.

18. Lian, J., Gou, W., Li, H., & Zhang, H. (2018). Effect of sediment size on damage caused by cavitation erosion and abrasive wear in sediment-water mixture. *Wear: An International Journal on the Science and Technology of Friction Lubrication and Wear*, *398–399*, 201–208. https://doi.org/10.1016/j.wear.2017.12.010

19. Liu, D., Hong, F., Zhao, F., Zhang, Z., 2008. The CFD analysis of propeller sheet cavitation. In: 8th Int. Conf. on Hydrodynamics (ICHD'08), Nantes, France.

20. M. Kamarlouei, H. Ghassemi, K. Aslansefat, and D. Nematy,"Multi-Objective Evolutionary Optimization Technique Applied to Propeller Design," Acta Polytech. Hungarica, vol. 11, no. 9, pp. 163182, 2014

21. M. Nohmi, Y. Iga, and T. Ikohagi. Numerical prediction method of cavitation erosion. In Proceedings of FEDSM 2008, Jacksonville, Florida, USA, 2008.

22. Matusiak, J. (1992). Pressure and noise induced by a cavitating marine screw propeller. *VTT PUBLICATIONS VALTION TEKNILLINEN*, *87*.

23. N. B. Vargaftik, B. N. (1983). International Tables of the Surface Tension of Water. Moscow Aviation Institute.

24. N. Hasuike, S. Yamasaki, and J. Ando. Numerical study on cavitation erosion risk of marine propellers operating in wake flow. In Proceedings of the 7th International Symposium on Cavitation, CAV2009, Ann Arbor, Michigan, USA, 2009.

25. N.-X. Lu, U. Svennberg, G. Bark, and R. E. Bensow. Numerical simulations of the cavitating flow on a marine propeller. In Proceedings of the 8th International Symposium on Cavitation, CAV2012, Singapore, 2012.

26. Numerical prediction of sheet cavitation on marine propellers using CFD simulation with transition sensitive turbulence model. (2018). *Alexandria Engineering Journal*.

27. O. Usta, B. Aktas, M. Maasch, O. Turan, M. Atlar, and E. Korkut. A study on the numerical prediction of cavitation erosion for propellers. In 5th International Symposium on Marine Propulsors, Espoo, Finland, 2017.

28. Peters, A., Lantermann, U., & el Moctar, O. (2018). Numerical prediction of cavitation erosion on a ship propeller in model- and full-scale. *Wear*, *408–409*, 1–12. https://doi.org/10.1016/j.wear.2018.04.012

29. Pham-Thanh, N., Tho, H. V., & Yum, Y. J. (2015). Evaluation of cavitation erosion of a propeller blade surface made of composite materials. *Journal of Mechanical Science and Technology*, *29*(4), 1629–1636. https://doi.org/10.1007/s12206-015-0334-4

30. R. Fortes-Patella, J.-L. Reboud, and L. Briancon-Marjollet. A Phenomenological and Numerical Model for Scaling the Flow Aggressiveness in Cavitation Erosion. EROCAV Workshop, Val de Reuil, France, 2004.

31. Ramakrishna, S., Ramakrishna, V., Ramakrishna, A., & Ramji, K. (2012). CFD Analysis of a Propeller Flow and Cavitation. International Journal of Computer Applications, 55(16), 26–33. https://doi.org/10.5120/8841-3125

32. S. J. Schmidt, M. Mihatsch, M. Thalhamer, and N. A. Adams. Assesment of the Prediction Capability of a Thermodynamic Caviation Model for the Collapse Characteristics of a Vapor-Bubble Cloud. WIMRC 3rd International Cavitation Forum, 2011.

33. S. Schenke and T. J. C. van Terwisga. Simulating compressibility in cavitating flows with an incompressible mass transfer flow solver. In 5th International Symposium on Marine Propulsors, Espoo, Finland, 2017.

34. S. Subhas, V. F. (2012). CFD Analysis of a Propeller Flow and Cavitation. *International Journal of Computer Applications (0975 – 8887).*

35. Sato, K., Oshima, A., Egashira, H., Takano, S., 2009. Numerical prediction of cavitation and pressure fluctuation around marine propeller. In: Proc. 7th Int. Symp. on Cavitation (CAV 2009) Ann Arbor, MI.

36. Singhal, A.K., Athavale, M.M., Li, H., Jiang, Y., 2002. Mathematical basis and validation of the full cavitation model. J. Fluids Eng. 124 (3), 617–624.

37. Symscape, (2013) Polyhedral, Tetrahedral, and Hexahedral Mesh Comparison

38. Szantyr J.K., (2006), Scale effects in cavitation experiments with marine propellers models.

39. Vargaftik, N. B., Volkov, B. N., & Voljak, L. D. (1983). International Tables of the Surface Tension of Water. Journal of Physical and Chemical Reference Data, 12(3), 817–820. https://doi.org/10.1063/1.555688

40. Vaz, G., Bosschers, J., 2006. Modelling three-dimensional sheet cavitation on marine propellers using a boundary element method. In: 6th Int. Symp. on Cavitation CAV2006, Wageningen, September.

41. Watanabe, T. (2003) "Simulation of steady and unsteady cavitation on a marine propeller using a RANS CFD code."

42. Yeo, K. B., Sabatly, R., Hau, W. Y., & Ong, C. M. (2014). Effects of Marine Propeller Performance and Parameters Using CFD Method. Journal of Applied Sciences. https://doi.org/10.3923/jas.2014.3083.3088

43. Zheng, Liu, & Huang. (2019). The Numerical Prediction and Analysis of Propeller Cavitation Benchmark Tests of YUPENG Ship Model. *Journal of Marine Science and Engineering*, *7*(11), 387. https://doi.org/10.3390/jmse7110387

44. Zheng, Liu, & Huang. (2019). The Numerical Prediction and Analysis of Propeller Cavitation Benchmark Tests of YUPENG Ship Model. Journal of Marine Science and Engineering, 7(11), 387. https://doi.org/10.3390/jmse7110387

45. Zhu, J., Chen, Y. S., Zhao, D., & Zhang, X. (2015). Extension of the Schnerr–Sauer model for cryogenic cavitation. *European Journal of Mechanics B-Fluids*, *52*, 1–10. https://doi.org/10.1016/j.euromechflu.2015.01.

APPENDIX A: ADDITIONAL CONTOURS

For 25rps
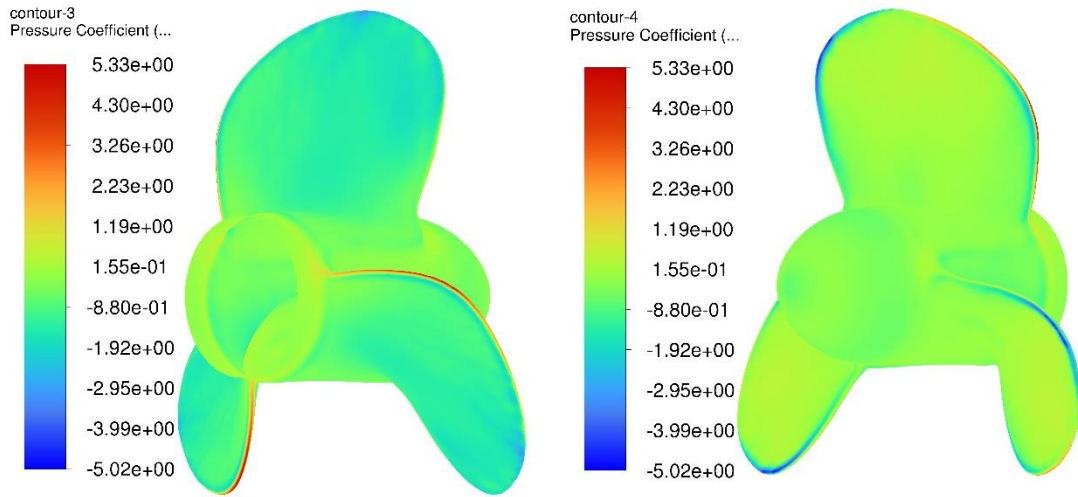
Figure A.0.1 Contour of Pressure Coefficient at Suction side (left) and Pressure side (right) for Schnerr-Sauer Model in Forward Operation
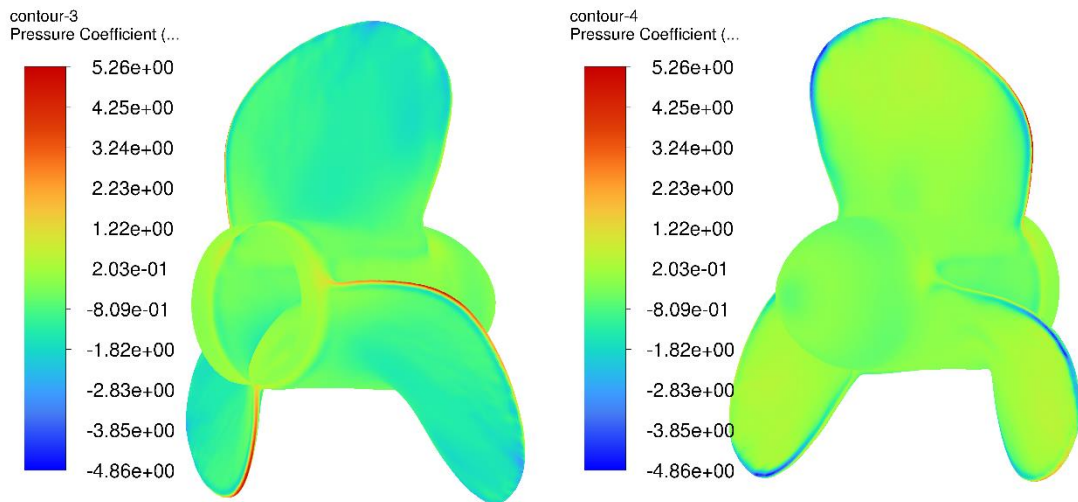
Figure A.0.2 Contour of Pressure Coefficient at Suction side (left) and Pressure side (right) for Singhal Model in Forward Operation

For 30rps
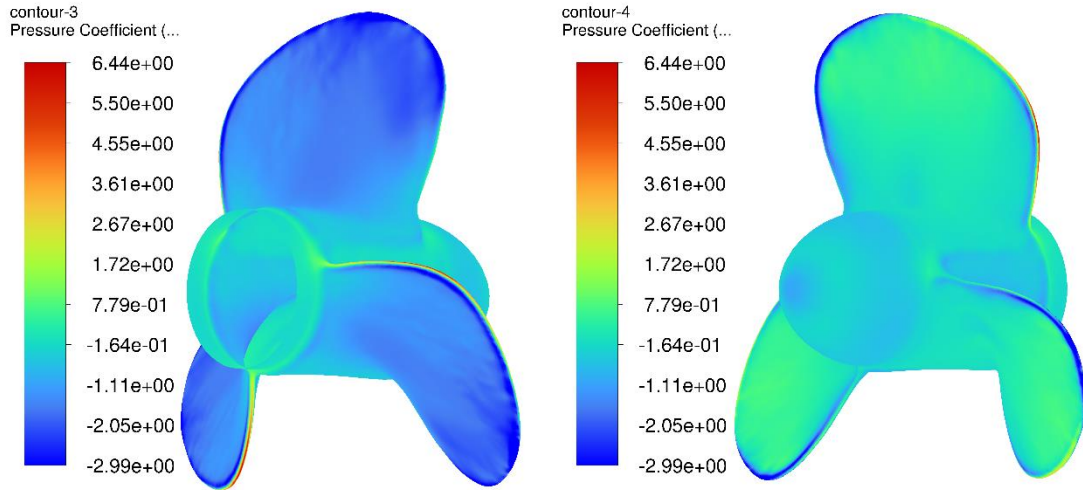
Figure A.0.3 Contour of Pressure Coefficient at Suction side (left) and Pressure side (right) for Schnerr-Sauer Model in Forward Operation
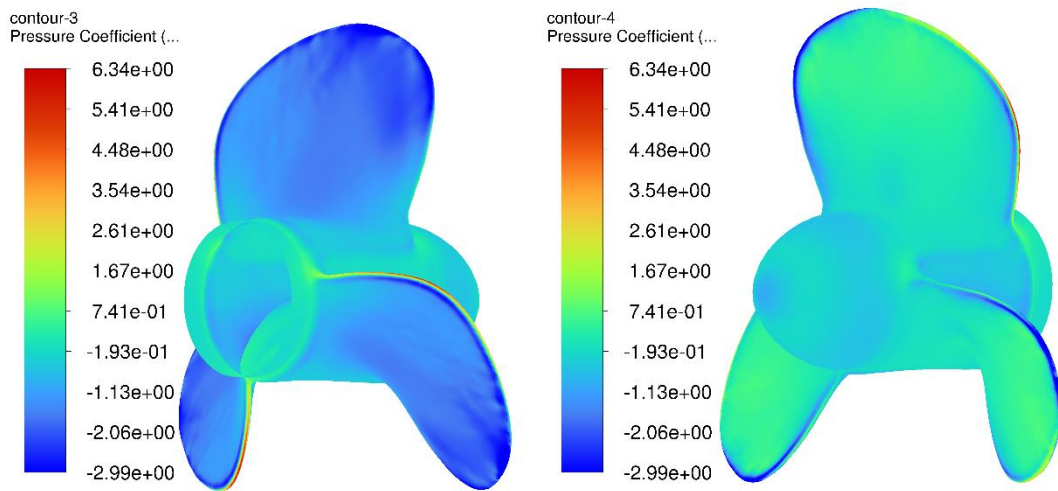
Figure A.0.4 Contour of Pressure Coefficient at Suction side (left) and Pressure side (right) for Singhal Model in Forward Operation

For 40rps,
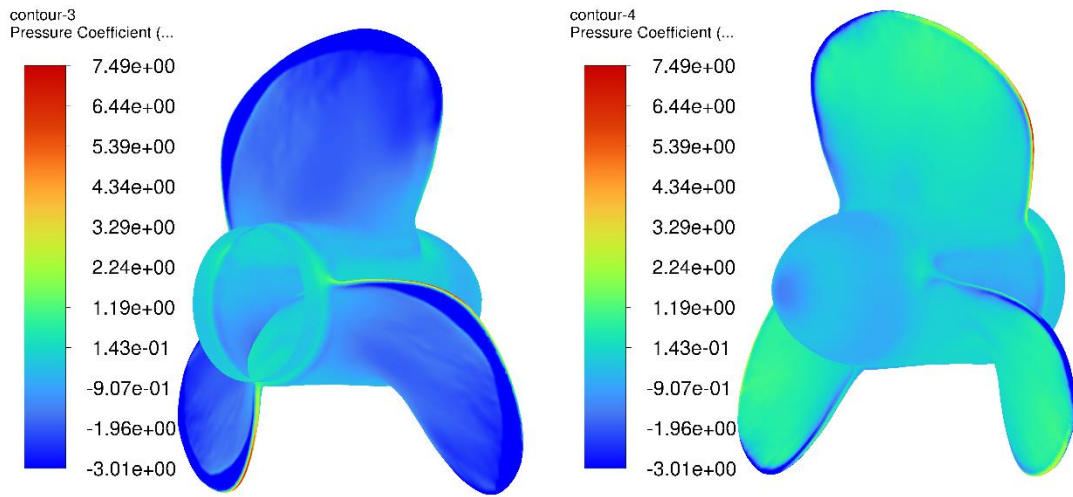
Figure A.0.5 Contour of Pressure Coefficient at Suction side (left) and Pressure side (right) for Schnerr-Sauer Model in Forward Operation
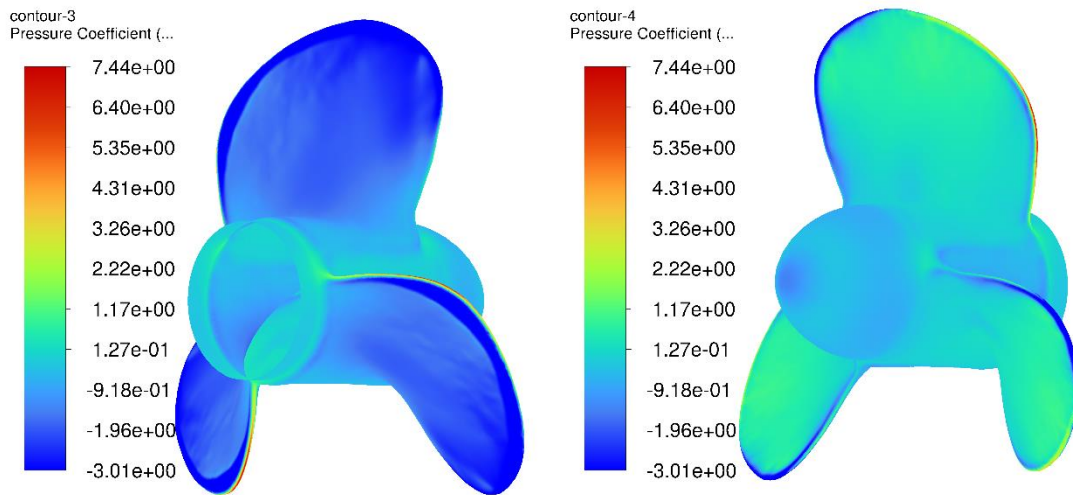
Figure A.0.6 Contour of Pressure Coefficient at Suction side (left) and Pressure side (right) for Singhal Model in Forward Operation

For 50rps,
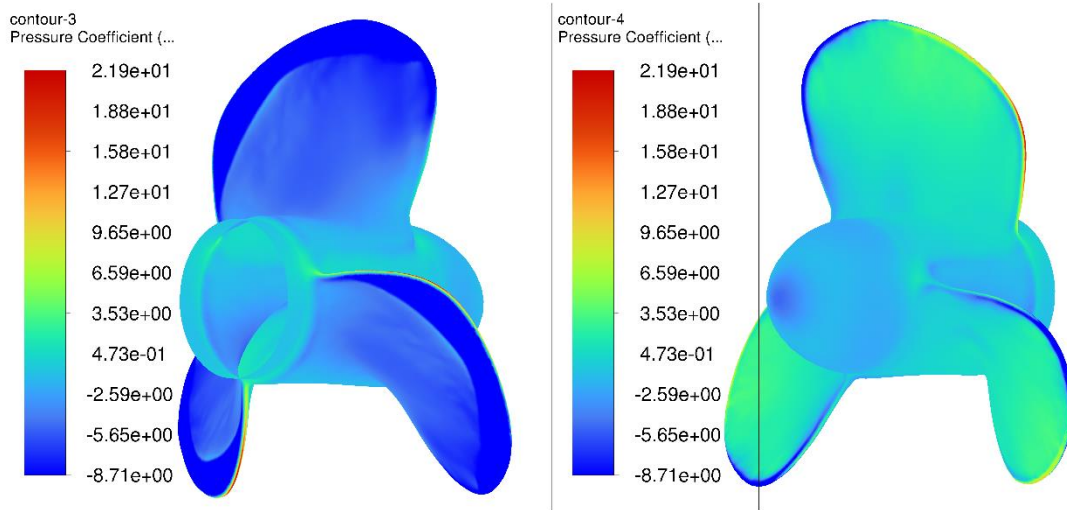
Figure A.0.7 Contour of Pressure Coefficient at Suction side (left) and Pressure side (right) for Schnerr-Sauer Model in Forward Operation
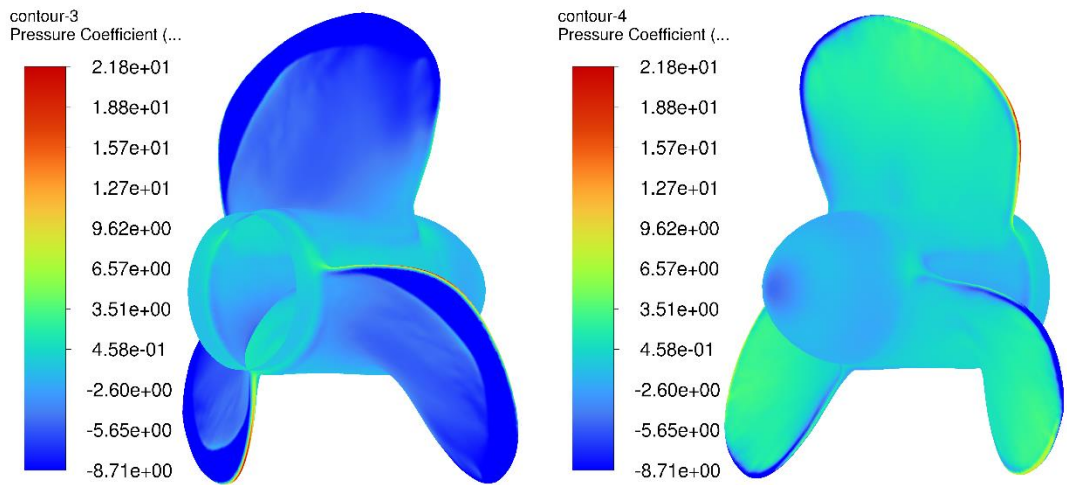
Figure A.0.8 Contour of Pressure Coefficient at Suction side (left) and Pressure side (right) for Singhal Model in Forward Operation

Schnerr-Sauer cavitation model at 25 rps
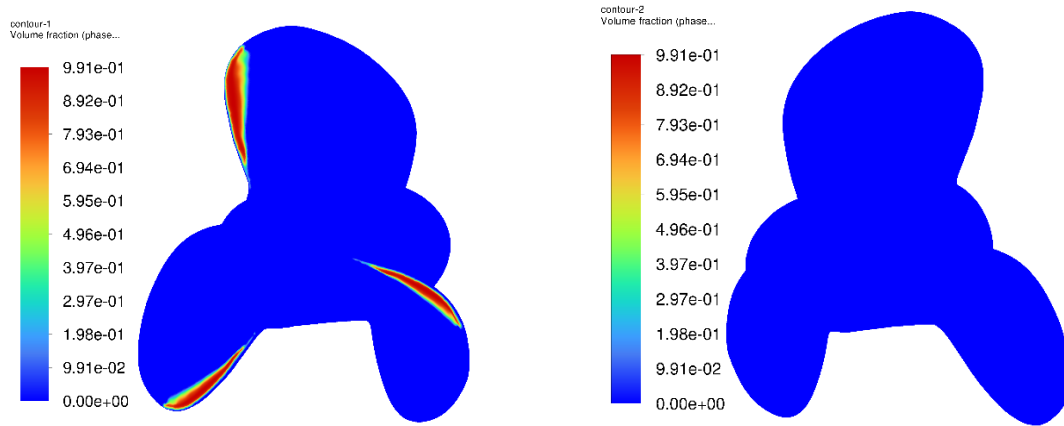
Figure A.0.9 Contour of Volume Fraction at Suction side (left) and Pressure side (right) in Reverse Operation
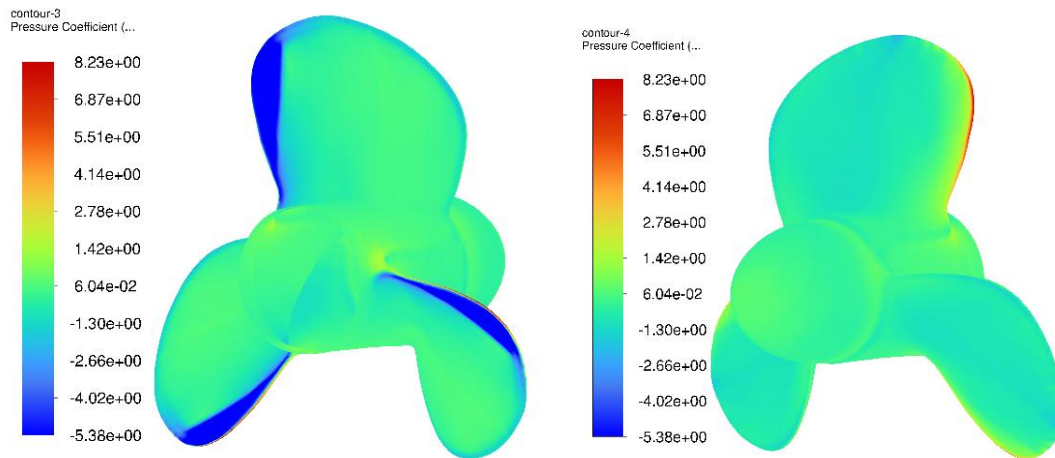
Figure A.0.10 Contour of Pressure Coefficient at Suction side (left) and Pressure side (right) in Reverse Operation

For Singhal cavitation model at 25 rps
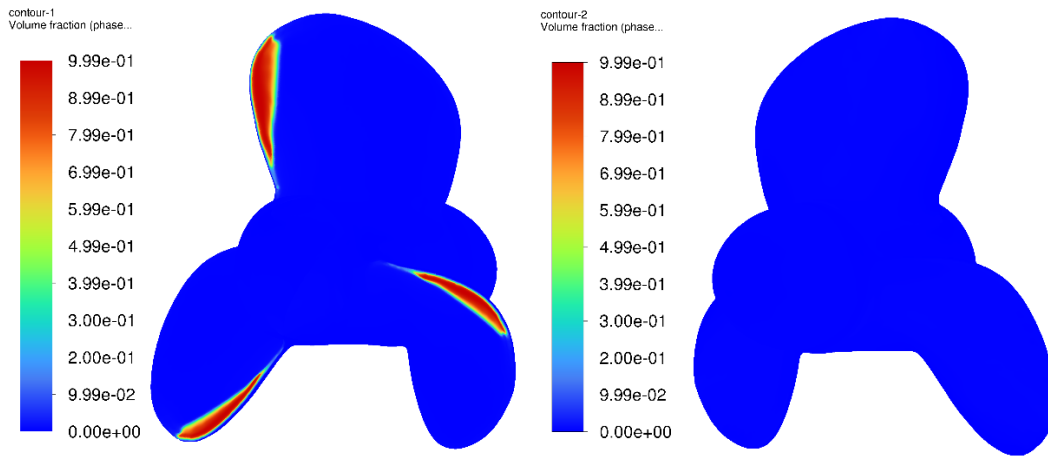
Figure A.0.11 Contour of Volume Fraction at Suction side (left) and Pressure side (right) in Reverse Operation
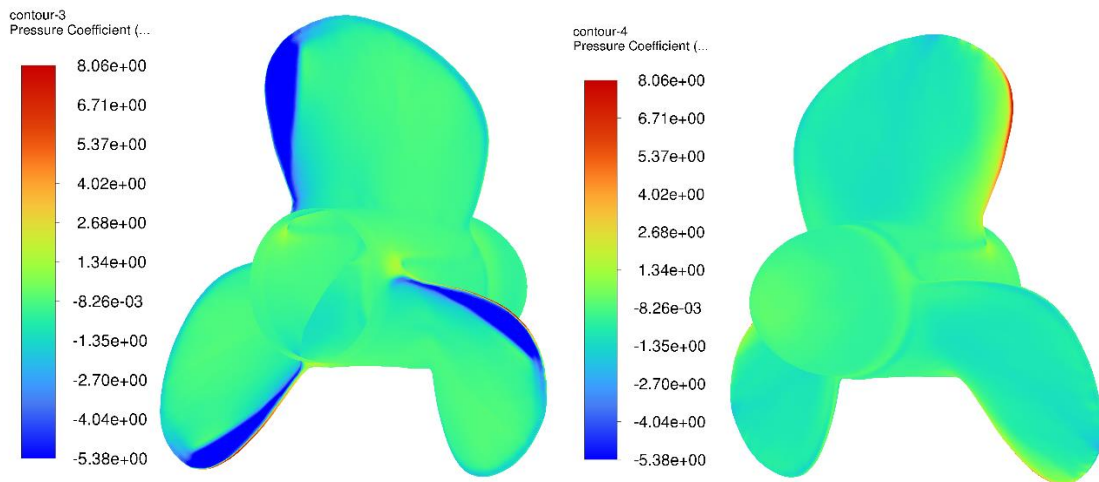
Figure A.0.12 Contour of Pressure Coefficient at Suction side (left) and Pressure side (right) in Reverse Operation

For Schnerr-Sauer cavitation model at 30 rps
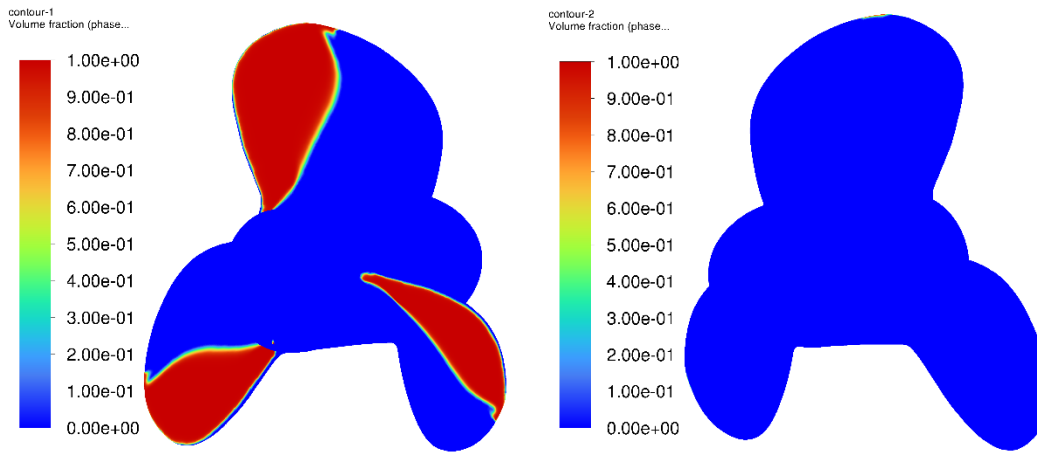
Figure A.0.13 Contour of Volume Fraction at Suction side (left) and Pressure side (right) in Reverse Operation
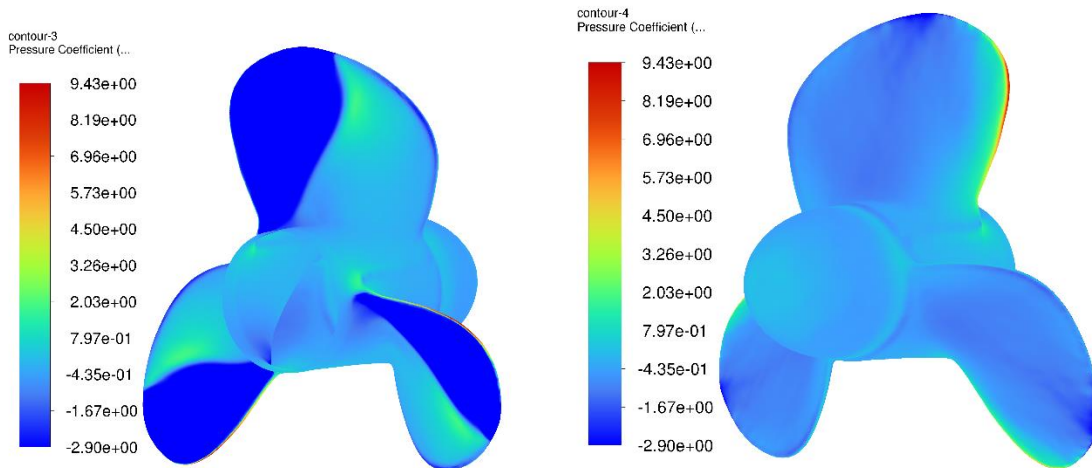
Figure A.0.14 Contour of Pressure Coefficient at Suction side (left) and Pressure side (right) in Reverse Operation

For Singhal cavitation model at 30 rps
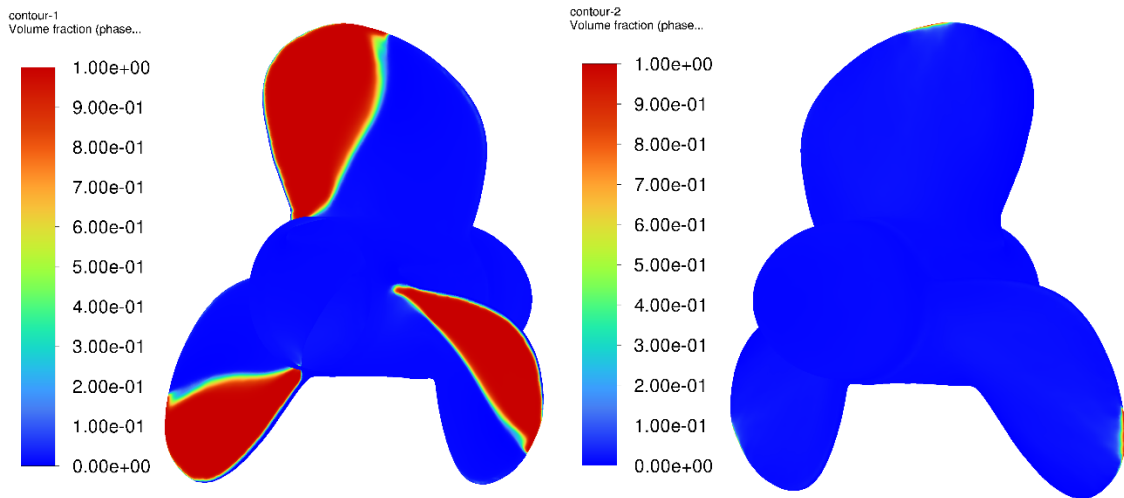
Figure A.0.15 Contour of Volume Fraction at Suction side (left) and Pressure side (right)
in Reverse Operation
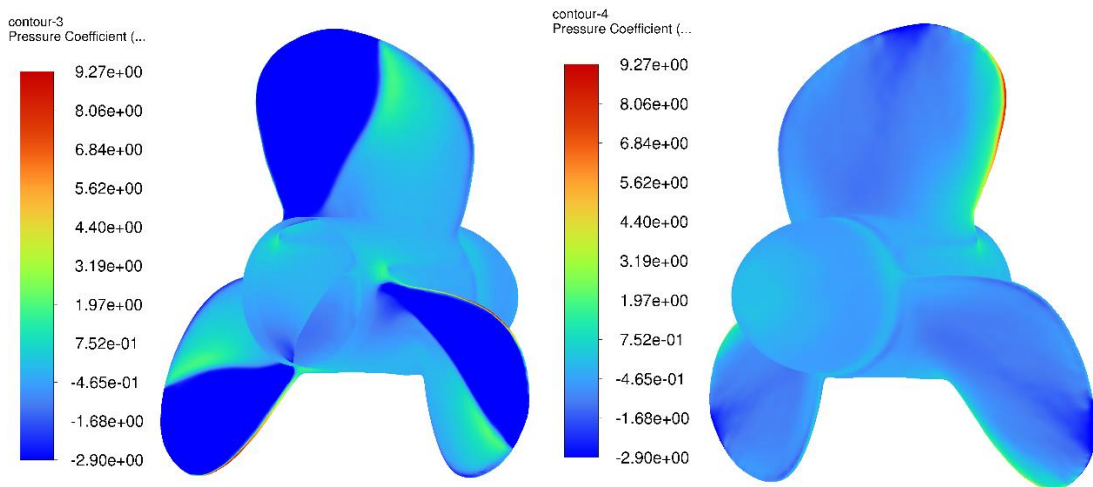
Figure A.0.16 Contour of Pressure Coefficient at Suction side (left) and Pressure side
(right) in Reverse Operation

For Schnerr-Sauer cavitation model at 40 rps
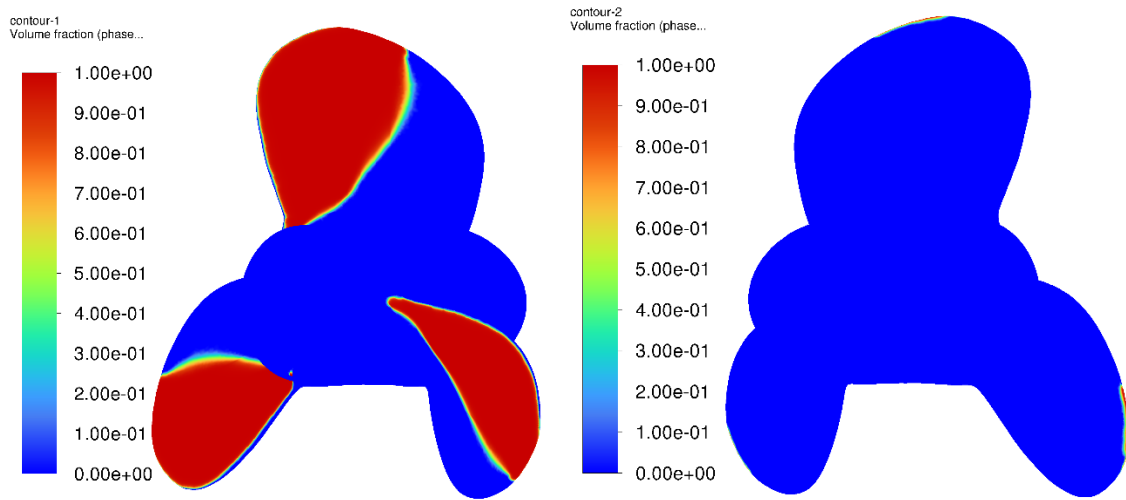
Figure A.0.17 Contour of Volume Fraction at Suction side (left) and Pressure side (right)
in Reverse Operation
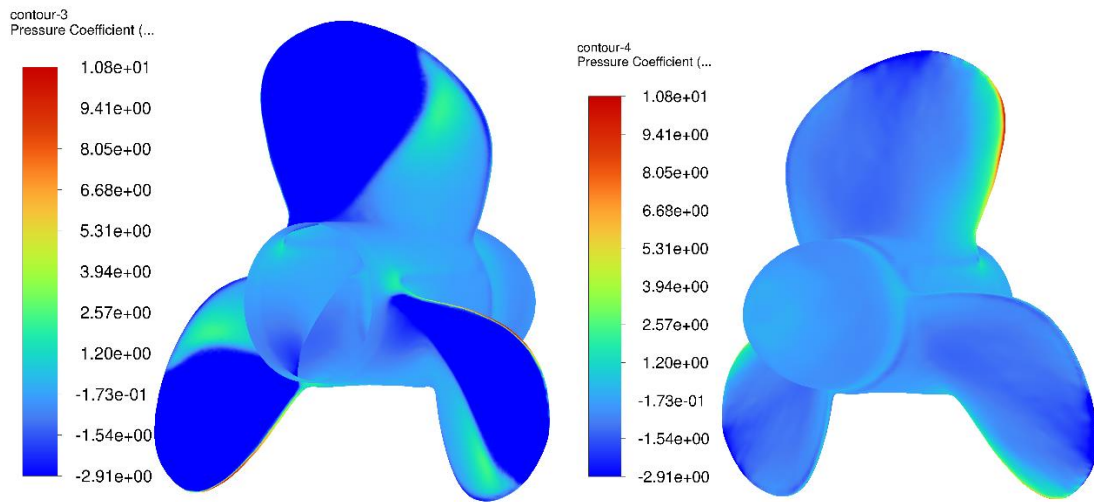
Figure A.0.18 Contour of Pressure Coefficient at Suction side (left) and Pressure side
(right) in Reverse Operation

For Singhal cavitation model at 40 rps
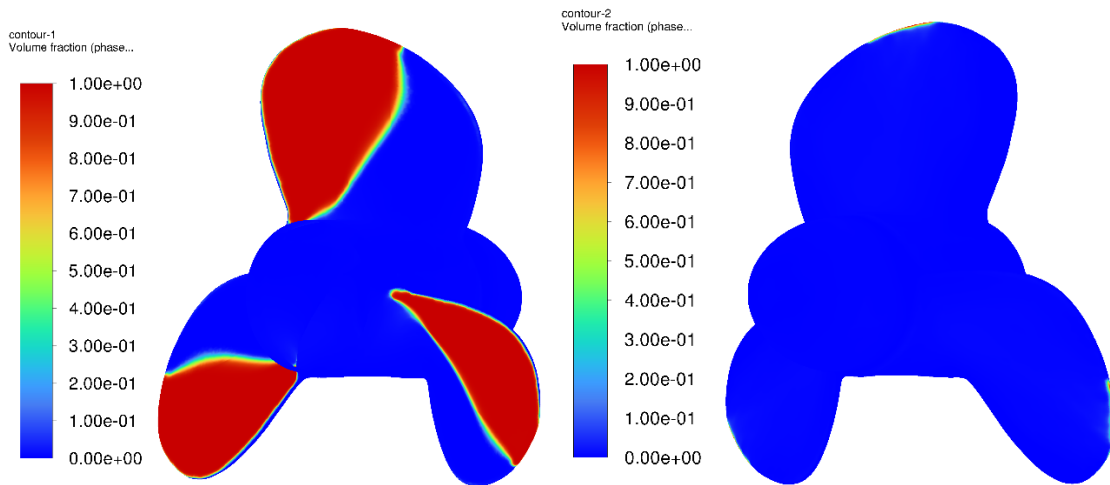
Figure A.0.19 Contour of Volume Fraction at Suction side (left) and Pressure side (right)
in Reverse Operation
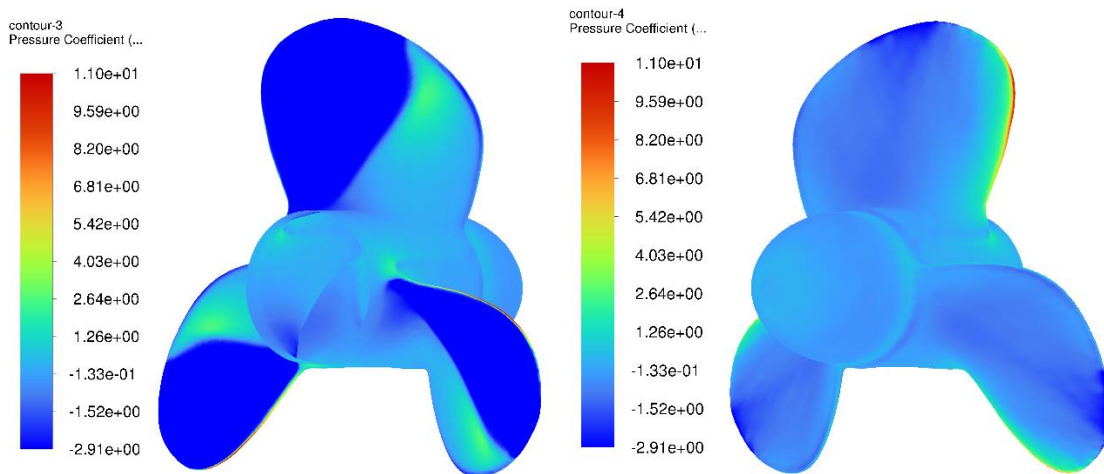
Figure A.0.20 Contour of Pressure Coefficient at Suction side (left) and Pressure side
(right) in Reverse Operation

For Schnerr-Sauer cavitation model at 50 rps
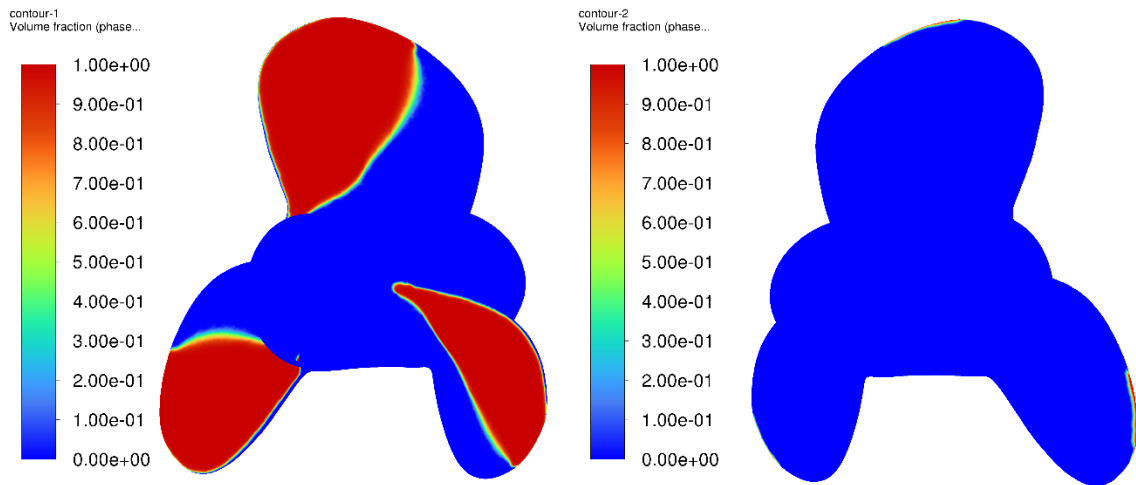
Figure A.0.21 Contour of Volume Fraction at Suction side (left) and Pressure side (right) in Reverse Operation
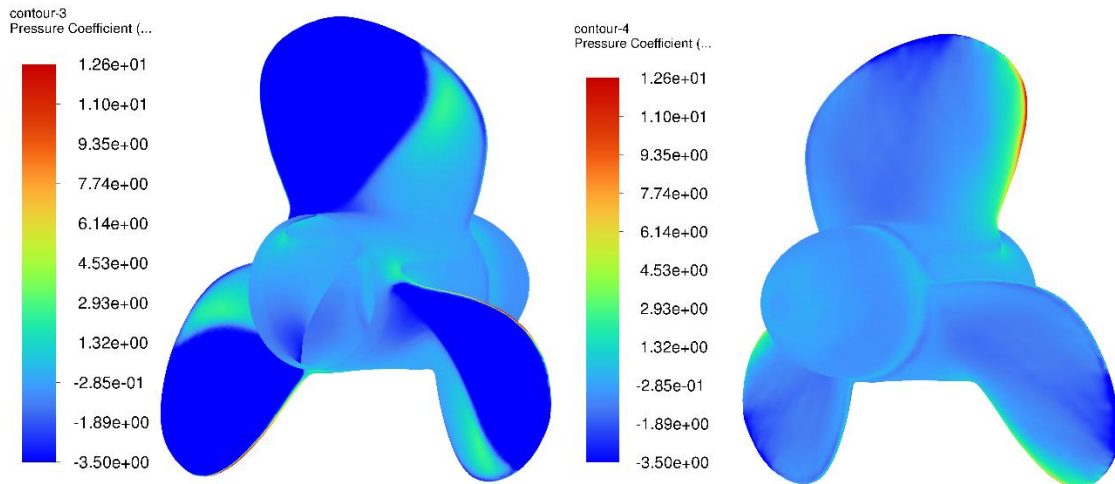
Figure A.0.22 Contour of Pressure Coefficient at Suction side (left) and Pressure side (right) in Reverse Operation

For Singhal cavitation model at 50 rps
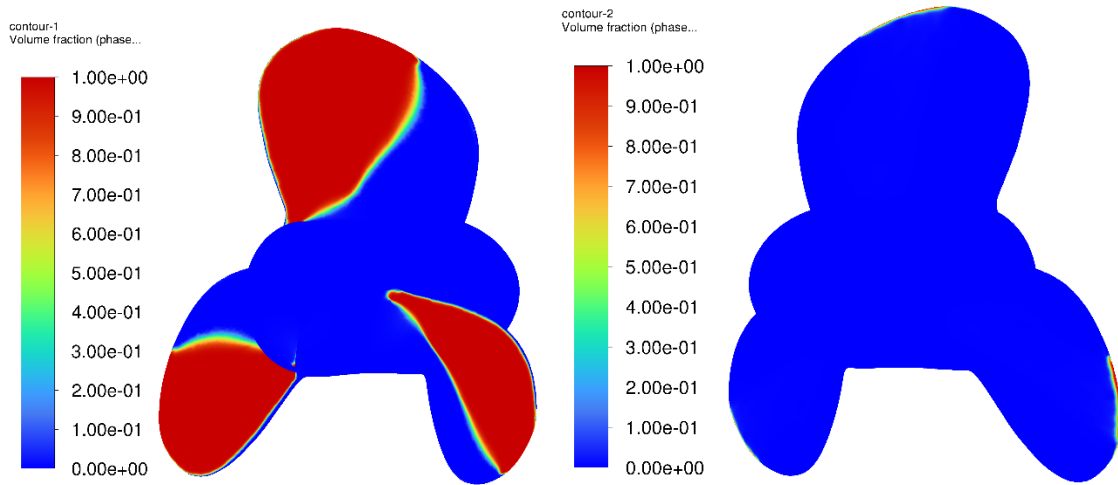
Figure A.0.23 Contour of Volume Fraction at Suction side (left) and Pressure side (right) in Reverse Operation
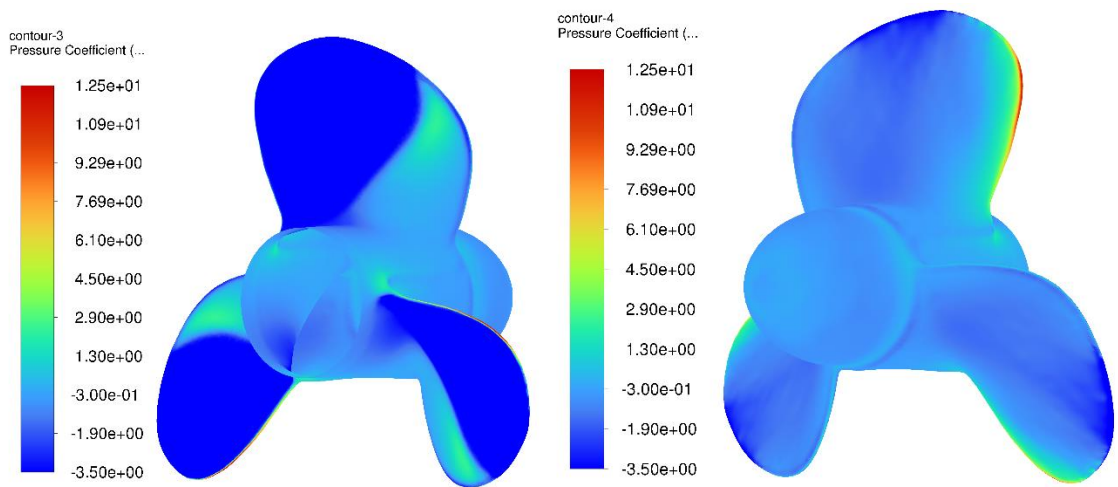
Figure A.0.24 Contour of Pressure Coefficient at Suction side (left) and Pressure side (right) in Reverse Operation